学位論文

The chemical and dynamical nature of dense cores in giant molecular clouds

（巨大分子雲における分子雲コアの化学的物理的性質）

平成 28 年 12 月博士（理学）申請
東京大学大学院理学系研究科
天文学専攻 大橋聡史

Abstract

Stars form in dense cores. Initial conditions of dense cores are the most important factors to determine formation process, masses and multiplicity of stars, and the nature of protoplanetary disks around them. Initial conditions of dense cores can be investigated in dense cores where star formation had has not started yet. Such dense core without star formation are often called "starless" dense cores. It is important to understand the nature of starless dense cores, in particular those on the verge of star formation because such starless dense cores must have the final condition just before star formation. However, it has been difficult to identify such dense cores partly because of short lifetime of starless dense cores on the verge of star formation and because of a lack of evolutional indicators of starless dense cores.

In dark clouds, chemical compositions of cores have been used as an indicator of evolutionary stages of cores ("chemical clock"). It is not clear, however, if chemical clocks established in cold cores also apply to warm cores whose temperature exceeds sublimation temperature of important players of chemical reaction networks such as CO, whose sublimation temperature is 25 K. Therefore, we evaluated several molecules like carbon-chain molecules (CCS, HC_3N), N-bearing molecules (N_2H^+, NH_3), and cyclic C_3H_2 as candidate tracers of chemical evolutions of the dense cores in two typical GMCs, the Orion A cloud and the Vela C giant molecular cloud complex, whose masses exceeding 10^4 $M_\odot$ and temperature exceeding 30 K.

Using the Nobeyama 45-m telescope and KVN 21-m telescope, we derived the molecular abundances of CCS, cyclic C_3H_2, and N_2H^+ toward dense cores in the Orion A cloud. To detect weak emission lines, these observations were performed with high sensitivities. As a result, CCS emission from $J = 7 - 6$ transition was detected for the first time towards the Orion A cloud. We found that the column density ratios of $N(N_2H^+)/N(\mathrm{CCS})$ and $N(\mathrm{c\text{-}C_3H_2})/N(\mathrm{CCS})$ are high in star forming cores while they are low in starless cores. We suggested that cyclic C_3H_2 is

better tracer for warm evolved cores than N_2H^+. Furthermore, we used CCS, HC_3N and NH_3 single-pointing observations data by Tatematsu et al. (2010) and Wilson et al. (1999). By these observations with high sensitivities, CCS emission from $J = 4 - 3$ transition was detected for the first time towards the Orion A cloud. We found that $N(NH_3)/N(CCS)$ and $N(NH_3)/N(HC_3N)$ are high in star forming cores while they are low in starless cores. These results that the carbon chain molecules trace the chemically young cores, while N-bearing molecules trace the chemically evolved cores, are the same with earlier findings in dark clouds. In the case of $N(NH_3)/N(CCS)$ and $N(NH_3)/N(HC_3N)$, we confirmed that these tendencies are applied for a wide range of kinetic temperature, $T_{\rm kin}$=$10 - 60$ K.

Subsequently, we confirmed these findings also apply to other GMC cores through observations of the HC_3N and N_2H^+ molecules toward the Vela C molecular clouds with the Mopra 22-m telescope. Even though the spatial resolution of 53" corresponding to 0.19 pc cannot resolve individual dense cores, we found a tendency that the $N(N_2H^+)/N(HC_3N)$ is high in star forming region, while it is low in starless region. This is the similar tendencies in $N(N_2H^+)/N(CCS)$, $N(c\text{-}C_3H_2)/N(CCS)$, $N(NH_3)/N(CCS)$, and $N(NH_3)/N(HC_3N)$ found in the Orion A cloud.

By comparing the published data of $N(NH_3)/N(CCS)$ and $N(N_2H^+)/N(HC_3N)$ in dark clouds and infrared dark cloud clumps, we found the criteria between star forming and starless cores are $N(NH_3)/N(CCS) \sim 30 - 40$ and $N(N_2H^+)/N(HC_3N) \sim 1 - 2$. Using the chemical reaction network of UMIST Database for Astrochemistry (UDfA) assuming a density of 10^4 cm^{-3} and a temperature of 10 K, we estimated a timescale of $4 \times 10^5 - 1 \times 10^6$ yr for these column density ratios achieve the criteria. This lifetime is several times longer than free-fall timescale and comparable to dissipation timescale of turbulence. Furthermore, we found a correlation between the chemical evolution and dissipation of turbulence ($R/R_{\rm cr}$), suggesting that the chemical evolution can be an indicator of the dynamical evolution of the core and the timescale is determined by the dissipation of turbulence.

Finally, we selected one of the most chemically evolved starless cores in the Orion A cloud (TUKH122 core) by means of the $N(N_2H^+)/N(CCS)$ ratio and observed it in the NH_3 ($J, K = 1, 1$) and ($J, K = 2, 2$) lines with high sensitivity (rms $\sim$ 40 mK) and spectral resolution (~ 0.05 km s^{-1}) by using the Nobeyama 45-m telescope. Interestingly, the NH_3 dense region has a linewidth of only ~ 0.2 km s^{-1} but the CS surrounding gas has a linewidth of ~ 0.8 km s^{-1}. This

indicates that the turbulent motions are dissipating in dense region. Taking into account the fact that TUKH122 is chemically evolved and the turbulence is almost dissipated within the core, we suggest that this core is on the verge of star formation. In the new observations using the Nobeyama 45-m telescope, we detect not only the quiescent thermal component but also a turbulent wing component in NH_3 ($J, K = 1, 1$), simultaneously for the first time towards this core. The detection of both NH_3 quiescent and turbulent components may indicate a sharp transition from the turbulent parent cloud to the quiescent dense core. This chemically evolved dense core (initial conditions of star formation) may be cold (~ 11 K) and coherent (~ 0.3 km s^{-1}).

Contents

Chapter 1

General introduction

1.1 Stars and initial mass function

Stars are one of the most fundamental objects in the universe and are the main component occupying about 90% of baryons in our Galaxy.

One of the most important properties of a star is its mass. By collapsing due to self gravity, the central materials become high temperature and high pressure, and the nuclear fusion reaction progresses accordingly. Once initial mass of a star is determined, its evolution after that can be almost predicatable. It is thus important to understand how stellar initial masses are determined.

Histogram of initial masses of stars are defined as the stellar initial mass function (IMF), and has been derived from nearby field stars (e.g., Salpeter, 1955). It is also studied toward various star forming regions in our Galaxy and external galaxies. Through these observations, it is suggested that the IMF shape is almost universal even though some power law variations have been reported (e.g., Scalo, 1986; Kroupa, 2001; Chabrier, 2003).

The origin of the IMF, however, remains unclear. The IMF is generally expressed as a power law, IMF $\propto m^{-\alpha}$, where m is the initial stellar mass and α is the slope of the logarithmic plot. Most popular IMF is that obtained by Salpeter (1955), with slope, $\alpha = 2.35$, over the entire mass interval between $0.4 - 10\ M_{\odot}$.

1.2 Interstellar molecular clouds

Stars are formed in interstellar molecular clouds where interstellar medium (ISM) is cold and dense. ISM consists of gas and dust, and the main component of the gas is hydrogen (74% in mass fraction), helium (25%), with minor contributions of the other heavier elements including C, N, and O. The dust grains consist of carbon, silicon, oxygen, and other heavy elements. The mass fraction of gas and dust is generally 100:1 (Hildebrand, 1983).

Atomic hydrogen (HI) is converted into molecular hydrogen (H_2) in region where density is higher than several 100 cm^{-3} and the UV radiation is shielded. Such dense region is called interstellar molecular clouds. The gas temperature is near equilibrium between heating and cooling, and the gas density changes with temperature in pressure equilibrium. Molecular hydrogen (H_2) does not emit radiation in cold environment because of lack of a permanent dipole moment. Molecules with permanent dipole moment are used to trace the distribution and kinematics of "invisible" H_2. Such molecules are called as tracer molecules.

We often use $^{12}C^{16}O$ (CO hereafter) rotational transition to trace H_2 because of the following three reasons; (1) CO is the most abundant molecule as high as 10^{-4} relative to H_2 (e.g., Dickman, 1978), (2) CO rotational level $J = 1$ lies 5.5 K above the ground state and is easily excited by collision with H_2 at 10 K, (3) CO is chemically stable. The critical density of CO is $\sim 10^3$ cm^{-3}, which allows us to observe most of the molecular clouds whose density is higher than several times 10^2 cm^{-3}. Therefore, CO transition is the most powerful probe to reveal molecular clouds. However, if we look into the physical conditions of dense region with a density of $\gtrsim 10^4$ cm^{-3}, we need other molecules whose critical densities are as high as 10^5 cm^{-3}.

1.3 Dense cores and embedded star formation

Molecular cloud condensation with the density higher than $\sim 10^4$ cm^{-3} is called a molecular dense core. For a few decades, molecular spectral observations and mm/submm dust continuum emission observations have been carried out and allowed us to understand the physical conditions in high dense regions of molecular clouds in low-mass star forming regions. "Dense cores" are established by a series of studies done by Benson & Myers (e.g., Myers & Benson, 1983a,b; Myers et al., 1983; Benson & Myers, 1989). They revealed that the molecular dense cores or dense cores

have a density of 10^{4-6} cm^{-3} and a temperature of $10 - 30$ K.

Dense cores are birth places of stars. This was shown in 1980s with Infrared Astronomical Satellite (IRAS) that observed 12, 25, 60, and 100 μm wavelengths toward 93% of all-sky area. A number of infrared point sources, or young stellar objects (YSOs) which are associated with dense cores were identified (Beichman et al., 1986).

YSOs are classified into various stages by their spectral energy distributions (SED) from the earliest main mass accretion phase (protostars) to the more evolved pre-main-sequence phase. It is well known to classify YSOs into three classes (Class I, II, and III) using the slope, $\alpha = d\log(\lambda F_\lambda)/d\log\lambda$, of SEDs at infrared wavelengths (e.g., Lada & Wilking, 1984; Adams et al., 1987) . The slope is classically derived from 2.2 and 25 μm energy fluxes. Class I sources are deeply embedded and show positive values of α of 0 to 3 (broader than single black body) because of infrared excess by their circumstellar/envelope material. Class II sources show negative values of α of -2 to 0 and cirumstellar disk emit infrared excess. Class III sources show negative values of -3 to -2, suggesting a single black body from central stars. Class II and III correspond to the pre-main-sequence star, in particular classical T Tauri star and weak-line T Tauri star, respectively.

An additional class, Class 0, was introduced by Andre et al. (1993) from submm continuum observations. Their SEDs are well fitted by black body with a temperature of $\sim$ 30 K. In this phase, central stars grow via mass accretion from the envelope cores and thought to be extremely young protostars in the main mass accretion.

When dense cores collapse, protostars are formed, which are seeds of stars. In this phase, urrounding circumstellar materials accrete onto the protostar to increase its mass. After the accretion stops and the parent dense core is swept away by outflows and/or radiations from stars, stars become visible at optical wavelengths. However, the protostars in early stage are still deeply embedded in the dense cores in early stage. They emit infrared radiation by heating surrounding circumstellar dust.

Star forming activities of Class 0 surces is characteraized by powerful bipolar outflows. Recent ALMA high spatial resolution observations clearly show that Class 0 objects have not only infall motions but also Keplerian rotational motions (e.g., Ohashi et al., 2014a; Aso et al., 2015). Furthermore, ALMA has also discovered centrifugal barriers where the kinetic energy of the infalling gas is converted to rotational energy. Chemical compositions drastically change in this

transition zone due to accretion shocks (e.g., Sakai et al., 2014; Oya et al., 2016). ALMA allows us to study a Keplarian disk formation and chemical compositions in the Class 0 phase, which is directly proceeding to planet formation.

1.3.1 Timescale of core evolution

The timescale of dense core evolution can be estimated with the number ratio of each stage object. For example, Onishi et al. (2002) estimated the typical lifetime of starless dense core to be several times 10^5 yr by comparing the number of protostellar cores with starless cores together with the age of T-tauri stars estimated from the H-R diagram. Andre & Montmerle (1994) also estimated the lifetime of Class 0 sources to be $\sim 10^4$ yr by comparing the number of Class 0 with Class I sources.

Accuracy of the timescale is improved through big and sensitive survey of nearby star forming regions with space telescopes such as the *Spitzer Space Telescope* and *Herschel Space Observatory* . The *Spitzer* covers the wide wavelengths of $3.6 - 70$ μm to identify embedded YSOs and to characterize the different evolutionary stages, from deeply embedded Class 0 stage to young stars which have lost most of their disks (Class III stage). One of the *Spitzer* legacy projects is "From Molecular Cores to Planet-forming Disks", or "Cores to Disks" abbreviated to "c2d project" (Evans et al., 2003), which obtained images and SEDs of YSOs in five large, nearby molecular clouds. By using these complete survey, Evans et al. (2009) derived the lifetimes of each stages. The derived lifetime for the Class 0 phase is $0.1 - 0.16$ My and for the Class I phase is $0.44 - 0.54$ Myr.

These timescales are compared with the free fall time of molecular clouds, which can be written as

$$t_{\rm ff} = \left(\frac{3\pi}{32G\rho(0)}\right)^{1/2} = 4 \times 10^5 \left(\frac{10^4 \ {\rm cm}^{-3}}{n}\right)^{1/2} \ {\rm yr}, \tag{1.1}$$

where ρ is the density (g cm^{-3}) and n is the number density (cm^{-3}). For dense cores with density higher than 10^4 cm^{-3}, the star-formation timescale is slightly longer than or comparable to the free fall time. The collapsing motions might be moderately supported by some mechanism such as magnetic field.

1.3.2 Structural and dynamical evolution of cores

The density structure of the cores can use stability equilibrium or non-equilibrium state of cores. In the Bonnor-Ebert sphere, a density contrast (central-to-surface density ratio) of 14 is the critical value. Cores in non-equilibrium state are on the way to gravitational collapse or stabilized by other mechanisms such as magnetic field and/or turbulence. We also often use virial analysis to look into a core equilibrium state because of its easy analysis. By assuming a uniform density core, the virial mass is estimated as

$$M_{\rm vir} = 210 \times \left(\frac{r}{1\ {\rm pc}}\right) \times \left(\frac{\Delta v}{1\ {\rm km\,s^{-1}}}\right)^2 M_\odot, \tag{1.2}$$

where r is the radius and Δv is the linewidth. MacLaren et al. (1988) suggested that the coefficient of the virial mass depends on the density profile, $\rho \propto r^a$, with the power-law index a. For uniform density ($a = 0$) the coefficient is 210, while for a power-law index ($a = -2$) similar to a Bonnor-Ebert sphere, the coefficient is 126 (see equation 1.2). The virial parameter, $\alpha_{\rm virial}$, is derived by $\alpha_{\rm virial} = M_{\rm vir}/M_{\rm core}$. If the virial parametner, $\alpha_{\rm virial}$ is less than 1, they are not in virial equilibrium and may be undergoing dynamical collapse. This analysis takes turbulent motions by using Δv, but the magnetic filed is still ignored.

1.3.3 Chemical evolution of cores

In star forming regions, ages of YSOs are often used as an indicator of ages of these regions. For starless cores, however, we cannot use this method. For starless cores in dark clouds, "chemical evolution" has been used as indicators of evolutionary phase. Chemical evolution is a method to estimate ages of starless cores under some physical conditions by studying observed molecular abundances and chemical models.

Ion-molecule gas phase reaction plays an important role to produce many kind of molecules in low temperature regions it is because ion-molecule reaction does not depend on temperature. Approaching ions make molecules polarized, and dipole moments are produced. As a result, the collisional cross section increases, and reaction rate becomes fast. For example, the presence of H_3^+ allows us to explain many observational results of interstellar chemistry such as HCO^+ ($H_3^+ + CO \longrightarrow HCO^+ + H_2$) and N_2H^+ ($H_3^+ + N_2 \longrightarrow N_2H^+ + H_2$), carbon-chain molecules,

and the isotopic fraction such as DCO^+/HCO^+ (Geballe & Oka, 1996).

Now, I will estimate the time scale of chemical equilibrium. For simplicity, I assume that molecules are produced from H_3^+ as following

$$H_3^+ + A \longrightarrow HA^+ + H_2 \tag{1.3}$$

and HA^+ is destroyed by electron

$$HA^+ + e \longrightarrow A + H, \tag{1.4}$$

where A is a molecule or an atom. H_3^+ is produced by following

$$H_2 + \text{c.r.} \longrightarrow H_2^+ + e \tag{1.5}$$

$$H_2^+ + H_2 \longrightarrow H_3^+ + H \tag{1.6}$$

Taking into account these equation (1.3)−(1.6), the reaction rate equation can be written as following based on H_3^+ and H_2^+ balance, respectively

$$\frac{d[H_3^+]}{dt} = k_1[H_2^+][H_2] - k_2[H_3^+][A] \tag{1.7}$$

$$\frac{d[H_2^+]}{dt} = \zeta[H_2] - k_1[H_2^+][H_2] \tag{1.8}$$

where k and ζ are reaction rate constant. From equation (1.7) and (1.8),

$$\zeta[H_2] = k_2[H_3^+][A] \tag{1.9}$$

Therefore, the time scale of the chemical equilibrium is

$$t = \frac{1}{k[H_3^+]} = \frac{[A]}{\zeta[H_2]} \tag{1.10}$$

Assuming A is CO, the chemical time scale will be $t = \dfrac{[CO]}{\zeta[H_2]} \sim 3 \times 10^5$ yr, which does

not depend on density. This time scale is almost comparable to free fall time of molecular clouds and thus the chemical composition may not be in equilibrium in molecular clouds. Therefore, the chemical evolution will be one of the powerful tools to judge the evolutionary stages of dense cores.

A pioneering study on the chemical evolution in dark clouds was done by Suzuki et al. (1992). They investigated the chemical characteristics of carbon-chain molecules like CCS, HC_3N, and HC_5N, and a N-bearing molecule, NH_3, in nearby dark cloud cores identified by Myers & Benson (1983b). They found that the abundances of the carbon chain molecules in dark clouds are correlated with each other but not with NH_3, which is more abundant in evolved cores associated with protostars. Based on the gas phase production models of carbon-chain molecules (Suzuki, 1983; Suzuki et al., 1992) and the gas phase production models of NH_3 (Herbst et al., 1987; Galloway & Herbst, 1989), the observed CCS/NH_3 ratios can be explained if dense cores form from diffuse gas in a period of 10^5 to 2×10^6 years. Thus, this ratio may be useful tracer of the chemical evolution in dark clouds, namely carbon-chain molecules (CCS, HC_3N) are abundant in chemically early phase, while N-bearing molecules (NH_3 and N_2H^+) are abundant in chemically late phase associated with protostars.

Although chemical evolution of dense cores in dark cloud is well studied, that of GMCs are less understood. Since most stars are formed in GMCs as clusters, the chemical evolution in GMCs is of great importance in studying the star-forming process in the Galaxy. Dark clouds and GMCs are different in their physical properties and associated star formation. Furthermore, it has become clear that gas phase chemistry by itself cannot explain all of the data and that gas-grain interactions and grain surface chemistry are essential as is evidenced by the detection of ices (Whittet et al., 1996). On the grain surface, hydrogenated species such as H_2O, NH_3, and CH_4 are produced because of the high mobility of atomic hydrogen on the cold surfaces. Then, energetic phenomena such as outflow shock waves and turbulent shocks, will provide the adsorbed NH_3 molecule to evaporate into gas phase from the grain surface.

Observations of a variety of molecular lines towards dense cores, offers information on how cores evolve. In nearby cold dark clouds, it has been suggested that molecules such as CCS, HC_3N, NH_3, and N_2H^+, and the neutral carbon atom C^0 are good tracers of the chemical evolution (e.g., Hirahara et al., 1992; Suzuki et al., 1992; Benson et al., 1998; Maezawa et al., 1999; Hirota

et al., 2002, 2009). The carbon-chain molecules such as CCS, HC_3N, and HC_5N are produced in chemically young stage by ion-molecular reactions and are easily depleted through both the gas-phase reactions and adsorption (Aikawa et al., 2001; Hirota et al., 2010). On the other hand, N-bearing molecules like N_2H^+ and NH_3 are produced in chemically late stage and their depletion time scale is larger than the other species because the nitrogen molecule N_2, which is the precursor of, N_2H^+ and NH_3, is produced in the late stages of the gas-phase chemistry and has a small binding energy on a grain surface (Aikawa et al., 2001). Therefore, the carbon-chain molecules, CCS and HC_3N trace the early chemical evolutionary stage, whereas N-bearing molecules, NH_3 and N_2H^+ trace the late stage. However, we should be careful about N_2H^+ molecule because this molecule is well known to react with gas phase CO to produce HCO^+ ($N_2H^+ + CO \longrightarrow HCO^+ + N_2$), which means that N_2H^+ traces quiescent cold dense regions where CO is depleted. It is suggested that CO evaporates from dust if temperature exceeds 25 K (e.g., Lee et al., 2004). As I explained, GMCs are warmer than cold dark clouds ($\sim$ 30 K) and are turbulent so that CO may be able to evaporate even in dense cores. Taking these effects, the chemical evolution in GMCs may differ from the above scenario. Therefore, it is highly needed to investigate these chemical evolution in GMCs.

Therefore, we evaluate some of the indicators of chemical evolution established in cold dark clouds (CCS, HC_3N, NH_3 and N_2H^+) as well as some other molecules (HCO^+, HCN), if they can be used a chemical clock in warm environments.

1.4 Dark clouds, giant molecular clouds (GMCs), and infrared dark clouds (IRDCs)

Molecular clouds are classified as giant molecular clouds (GMCs) and dark clouds. GMCs have molecular mass greater than 10^4 $M_\odot$ and comprise high-mass stars and cluster forming regions (including low- intermediate- mass star-formation). They are dominated by turbulent motions and are relatively high temperature ($10 - 30$ K). Dark clouds have mass lower than 10^4 $M_\odot$ and comprise only low-mass isolated star forming region. They have narrower linewidth ($\Delta v \sim 0.3$ kms s^{-1}) and are cold ($\sim$ 10 K).

Representative examples of GMCs (high mass star forming region) include the Orion A/B

cloud, Vela C molecular cloud complex and others. The Orion A cloud and Vela C molecular cloud complex are our targets of this thesis.

Their mass function and lifetime can be estimated by large surveys. In Large Magellanic Cloud (LMC), GMCs with masses larger than 2×10^4 $M_\odot$ have been identified by NANTEN observations and the mass spectrum of the clouds is fitted well by a power law of $N_{\rm cloud}(> M_{\rm CO})$ $\propto M_{\rm CO}^{0.75\pm0.06}$ above the completeness limit of 5×10^4 $M_\odot$ (Fukui et al., 2008). Kawamura et al. (2009) derived a lifetime of $20 - 30$ Myr for these GMCs by adopting the timescale of the youngest stellar clusters,10 Myr assuming that the number of the GMCs should be proportional to the timescale of each evolutionary stage. They also suggested that the GMCs are destroyed by strong UV radiation from massive stars.

Objects thought to host the earliest stages of high-mass star formations in GMCs are Infrared Dark Clouds (IRDCs). They were recently discovered as dark regions obscuring the bright mid-infrared background (Perault et al., 1996; Egan et al., 1998; Simon et al., 2006; Peretto & Fuller, 2009). Recent studies in IRDCs show masses of 10^{2-4} $M_\odot$ or higher at a scale of $\sim 1 - 3$ pc. Their embedded compact clumps have an average mass of ~ 120 $M_\odot$ and size of $\lesssim 0.5$ pc (Rathborne et al., 2006). Molecular line studies in NH_3 found that they have a temperature of ~ 15 K and a linewidth of ~ 2 km s^{-1} (e.g., Pillai et al., 2006; Sakai et al., 2008b; Ragan et al., 2011, 2012; Dirienzo et al., 2015). Furthermore, it has also been reported that IRDCs consist of many filamentary structures (Rathborne et al., 2006; Sanhueza et al., 2010; Contreras et al., 2016).

Although there are some evidences for active high-mass star formation at certain locations in IRDCs such as ultracompact (UC) HII regions (Hoare et al., 2007; Battersby et al., 2010), hot cores (Rathborne et al., 2008), embedded 24 μm sources (Chambers et al., 2009), molecular outflows (Sanhueza et al., 2010; Wang et al., 2011), or maser emission (Wang et al., 2006; Chambers et al., 2009), most of the IRDCs are quiescent and have massive cold IR-dark clumps, and thus it is suggested that star formation has not started yet. Therefore, these objects are believed to be the best targets in the earliest phase of high-mass star formation. Recent space telescopes such as *Spitzer* and *Herschel* improved the sensitivities at mid infrared wavelengths and succeeded in identifying a number of YSOs in IRDCs. The initial conditions of star formation will be revealed by investigating molecular dense core which are extremely dense but a protostar does not exist. Therefore, we should be careful about target selections even in IRDCs to reveal the initial condi-

tions of high-mass star formation.

Representative examples of nearby cold dark clouds (low mass star forming region) include the Taurus, Chamaeleon, and others. On contrary to dense cores in GMCs and IRDCs, those in dark clouds are very quiescent. Dense cores in nearby cold dark clouds (such as Taurus, Ophiuchus, and Camaeleon dark clouds) are cold ($\sim$ 10 K) and narrow linewidth ($\Delta v \sim 0.3$ km s^{-1}) because no massive stars are formed in this region.

There are observational evidence for lack of massive star formation in dark clouds. For instance, Onishi et al. (2002) identified 55 $H^{13}CO^+$ condensations in Taurus, of which 44 are starless. The steep slope of the mass spectrum of these starless condensations shows $dN/dM \propto M^{-2.5}$ for 3.5 $M_\odot < M <$ 20.1 $M_\odot$. The most massive starless core is 20.1 $M_\odot$. Assuming star formation efficiency of 30% (Evans et al., 2009; Machida & Hosokawa, 2013), no massive stars will be formed in Taurus.

1.5 Possible scenario of star formation

I will summarize the recent understanding on formation of the low to intermediate-mass stars and high-mass stars, respectively in the followings:

1.5.1 Low-mass stars

Most of stars in the local universe are low-mass stars ($\sim$ 1 $M_\odot$). Formation process of low mass stars has been investigated intensively because of the abundance of low-mass stars, proximity of low-mass star forming regions, and its simple physics and chemistry without effects from strong UV radiation or shock by massive stars.

Theoretical models of the formation of a single, low-mass, and isolated star have been established since Shu et al. (1987) provided its framework. In these models, star formation begins with contraction of rotating and self-gravitational dense cores and protostars are formed through gravitational collapse. Angular momentum of the core makes it form an accretion disk where the centrifugal force balance the gravitational force and accretion of the surrounding materials. The materials of the disk can accrete to the protostar by releasing its angular momentum through an outflow (e.g., Snell et al., 1980). This main accretion phase continues for $\sim$ 1 Myrs. These phases are classified as Class 0 and I as mentioned in the previous section.

To reveal the collapsing process, the density structure is one of the most important information. Bok globules are good targets to measure the density profile from central dense part to outer diffuse part because they are isolated and uncontaminated by other sources. On the basis of near-infrared observations, Alves et al. (2001) showed that the Bonnor-Ebert Sphere model (Bonnor, 1956; Ebert, 1955) can explain observed radial column density profile of the bok grobule Barnard 68. The Bonnor-Ebert shape consists of flat central region surrounded by a steeper outer region of $\rho \propto r^{-2}$. Many nearby globules have shown the Bonnor-Ebert structure revealed by Kandori et al. (2005); Launhardt et al. (2013). When a Bonnor-Ebert sphere collapse, it is expected that the infall velocity increase with radius in the flat dense region because free fall time does not depend on radius and takes the same time. On the other hand, in outer part of $\rho \propto r^{-2}$, the infall velocity decrease with radius. Larson (1969) and Penston (1969) solved the density evolution of an isothermal uniform density gas sphere analytically with assuming that a core does not maintain kinetic balance (LP solution). They found self-similar solutions to describe the collapse of an isothermal gas ("runway" collapse). When a central object (first core) is formed, the density profile reaches $\rho(r) = 4.4(c_s^2/2\pi G)r^{-2}$ and velocity field is $v(r) = 3.3c_s$. Shu et al. (1987) also showed the isothermal similarity solution, which assume a core that slowly increase its central density through ambipolar diffusion with keeping equilibrium state. After the density profile achieves a singular isothermal sphere, the core is dynamically collapse ("inside-out" collapse). This model considers $\rho(r) = (c_s^2/2\pi G)r^{-2}$ when the core is collapse. To be exact, LP solution described infall motion before the first core is formed, while Shu model described core collapsing motion after the first core is formed. Therefore, Hunter (1977) and Whitworth & Summers (1985) developed LP solution by analyzing collapsing motion after the first core formation. Hunter (1977) showed the case of unstable Bonnor-Ebert sphere. Whitworth & Summers (1985) derived similarity solutions for the isothermal sphere with the Shu and LP solutions.

These models suggest that the density and velocity structure show $\rho \propto r^{-1.5}$ and $v \propto r^{-0.5}$, respectively, from the center to the outside. The outside radius expands with sound speed (c_s) for the Shu solution and with $3.3c_s$ for the LP solution. The mass infall rate is predicated to be $\sim c_s^3/G$ for the Shu solution and 48 times higher than this for the LP solution. Recent observations have reported that the infall motion can be explained by the inside-out collapse (e.g., Hogerheijde & Sandell, 2000; Kurono et al., 2013; Evans et al., 2015) or by the isothermal collapse of a marginally

critical Bonnor-Ebert sphere (former accretion is similar to the LP solution but the later accretion is similar to the Shu solution) (Kurono et al., 2013).

However, this scenario has mainly been established based on observations of bok globules or isolated low-mass dense cores where thermal motions are dominant in cores found in cold dark clouds (e.g., Tatematsu et al., 1993; Caselli & Myers, 1995). Taking into account the fact that most stars ($70 - 90$ %) are formed in GMCs as clusters (Lada & Lada, 2003), it is of great importance to check if this scenario also applies to cluster forming regions where nonthermal motions are dominant.

To reveal star forming process in GMCs and cold dark clouds, it is essential to compare the initial conditions of star formation in prestellar cores (e.g., density distribution, linewidth distribution, and velocity fields) between them.

1.5.2 High-mass stars

Even though high mass stars ($\geq$ 8 $M_\odot$) are rare, they rule the energetics and chemistry of interstellar matter via by strong UV radiation and supernova explosions.

Nowadays, it is widely accepted that high-mass stars are formed in dense cores (coalescence of stars are much rare). However, there are mainly two problems to answer in high-mass star formation. One is the accretion flow inversion problem and the other is timescale problem. The accretion flow inversion problem is that accretion cannot proceed because the outward radiation pressure from the central star exceeds the inward gravitational pressure. The timescale problem is that the central star finishes the main sequence phase before the star increases its mass and becomes high-mass stars assuming the typical accretion rate ($\sim 10^{-7}\ M_\odot$ yr^{-1}) of low-mass star formation. Therefore, it might be possible that high-mass stars are formed in a process different from low-mass star-formation.

One possible solution is that high-mass stars form at a very high mass accretion rate. If the mass accretion rate is as high as $10^{-3}\ M_\odot$ yr^{-1}, the feedback effect becomes less important by the dynamical pressure and a several 10 $M_\odot$ can be formed. If this is the case, a massive outflow is expected to release the angular momentum through accretion process. Some observations support such massive outflow (e.g., Sanhueza et al., 2010; Zhang et al., 2015; Tan et al., 2016; Feng et al., 2016)

However, studies of high mass star formation are relatively few compared with that of low mass star formation. The reason is that high-mass stars form in crowded and complex environments (clusters) at large distances ($\gtrsim$ 2 kpc), making it difficult to resolve individual objects in clusters. Another difficulty is their very short prestellar phase (Motte et al., 2007) in spite of the fact that revealing the prestellar phase is very important to investigate high-mass star-forming processes.

There are currently two main models of high-mass star formation under debate: the turbulent core accretion model and the competitive accretion model. These two models differ in how and when the mass is gathered.

Turbulent core accretion model

The turbulent core accretion model is a scale up version of low-mass star formation. A dense core is supported by self-gravity, turbulence, and magnetic field. The core does not have fragmentations any more, and a single or a close multiple-star system are formed. In this model, the dense cores must be massive, much larger than the final stellar masses, because no further accumulation from surrounding cloud to core occur (McKee & Tan, 2003).

In this model, the star formation process is the same way as the low-mass star formation and the efficiency (the final stellar masses per unit dense core mass) may be almost constant. In low-mass star forming region, star formation efficiency (SFE) is estimated to be 0.3 (Evans et al., 2009). By accepting a constant SFE, we can expect there is a direct relation between the distribution function of core masses (Core Mass Function, CMF) and that of stellar masses (Initial Mass Function, IMF). It is also predicted that cores that form high-mass stars should be highly turbulent McKee & Tan (2003). These turbulent motions support the cores against gravitational instability, which means that cores are virialized ($\alpha_{\rm virial} = M_{\rm vir}/M_{\rm core} \sim 1$).

In order to test this model from observations, one of the important results should be identifying "massive prestellar core" having $\alpha_{\rm virial} = M_{\rm vir}/M_{\rm core} \sim 1$. Tan et al. (2013) claimed to find a massive prestellar and virialized core that are bounded by the high pressures of their surrounding clumps and magnetic field, consistent with the turbulent core accretion model. However, Tan et al. (2016) reported to identify highly collimated bipolar outflow that is being launched from the core, suggesting that the core is not prestellar. Further research is needed to test this model.

Competitive accretion model

Alternative is competitive accretion model. According to this model, high-mass star formation is highly dynamical. Large scale clumps ($\gtrsim$ 1 pc) fragment into cores having the thermal Jeans mass (Bonnell et al., 2004; Bate & Bonnell, 2005). Because the thermal Jeans mass is $\sim 1\ M_{\odot}$, mass accretion from surrounding gas is important to form high-mass stars. If we assume high-mass stars are formed in high density clouds, the thermal Jeans cores are embedded in a massive surrounding cloud. Some cores are located at the center of the gravitational potential in the cloud and may increase the mass via Bondi-Hoyle accretion. Eventually, high-mass stars are formed. One important distinction from the turbulent core accretion model is that "prestellar core" is not enough massive to form high-mass stars by itself. Not only gravitational collapse of the core but also large-scale inflow from the cloud is crucial.

In order to test this model from observations, one of the important results should be identifying "only low-mass (thermal Jeans mass) prestellar cores". In the cores where the gravitational potential is deep and high-mass stars are finally formed, the virial parameter $\alpha_{\rm virial}$ should be much lower than unity (Kauffmann et al., 2013).

Pillai et al. (2011) found prestellar cores having much lower values of virial parameters consistent with the competitive accretion model. However, Henshaw et al. (2016) suggested that these cores are supported by magnetic field and virialized. Zhang et al. (2009), Wang et al. (2011) and Ohashi et al. (2016a) suggested that a continuous accretion over a large scale from 1 to 0.01 pc onto protostars are needed to form high-mass stars. These results are inconsistent with the turbulent core accretion model. Moreover, the core masses they identified are much larger than the Jeans mass, which is also inconsistency with the competitive accretion model.

These observations do not support any of these two models and further research is needed to establish theories of high-mass star formation. To judge which scenario is true by observations, it is highly needed to identify initial conditions of high mass star formation. In order to search for such region (star formation has not stared yet but on the verge of star formation), we need to find out what evolutionary phase the molecular cloud core is in. For example, in case that molecular clouds are in very young stage, dense core formation has not started yet and chemically evolved

massive prestellar cores should not exist even if core accretion model is true. Therefore, we should know the evolutionary stages of massive dense cores in starless phase.

1.6 Scope of this work

In dark clouds, chemical compositions of cores have been used as an indicator of evolutionary stages of cores ("chemical clock"). It is not clear, however, if chemical clocks established in cold cores also apply to warm cores whose temperature exceeds sublimation temperature of important players of chemical reaction networks. For example, CO sublimation temperature is 25 K. Therefore, we evaluated several molecules as candidate tracers of chemical evolutions of the dense cores in two typical GMCs, the Orion A cloud and the Vela C giant molecular cloud complex, whose masses exceeding 10^4 $M_\odot$ and temperature exceeding 60 K. We will establish the chemical evolution in dense cores and reveal their evolutionary stages. By comparing chemically evolved dense cores with chemically young cores, we estimate the timescale of dense cores and investigate what is the important factor to initiate star formation. We also search for dense cores on the verge of star formation.

To understand the star formation process in GMCs, the initial conditions of star formation must be uncovered. For example, revealing initial conditions of star formation is quite essential to determine formation process, initial masses and multiplicity of stars, and the nature of protoplanetary disks around them. However, such dense cores on the verge of star formation are very rare because starless cores are in equilibrium state for $\sim 10^5$ yr in dark clouds (Onishi et al., 2002). By accepting the "inside-out" collapse of the Shu model, we can expect that a dense core with a power law, $\rho \propto r^{-2}$ alone, may be the initial conditions of star formation even though we don't know whether this model can be applied to cluster formation in GMCs or not. However, spatially high resolution and dynamic-range observations are quite important to determine the density structures of dense cores in GMCs because GMCs are located further from the earth. Therefore, it is difficult to determine the evolutionary stage of dense cores by judging from physical properties.

To determine the evolutionary stages of the dense cores and discover a critical dense core having the initial conditions, I am focusing on the chemical evolution, which will be a powerful tool to determine the evolution and search for the dense core. Therefore, the aim of this thesis is to establish the chemical evolution of dense cores in GMCs. This will allow us to promote a new

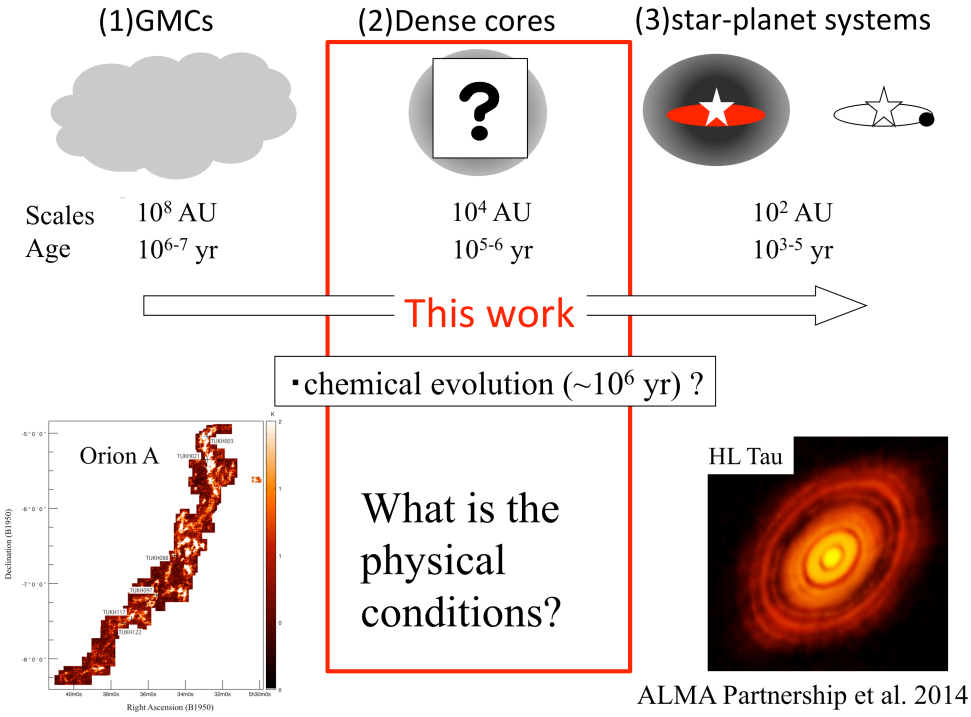

Figure 1.1: Schematic view of the approach of this thesis

exploration not only in our Galaxy but also in nearby galaxies. It is expected that the evolution of clouds in nearby galaxies will become major research topics because ALMA resolution and sensitivity will allow us to study it in great detail. However, the evolution of GMCs has not been established in our Galaxy. I expect to obtain a new paradigm of GMC evolution study, which will naturally lead to astrochemical study of clouds in nearby galaxies by ALMA.

1.7 Source selection

1.7.1 The nearest, best studied GMC: Orion A cloud

The Orion A cloud is one of the nearest (418 pc; Kim et al., 2008) and best studied GMCs .

Regarding the chemical evolution of the Orion A cloud, there are some recent studies. Tatematsu et al. (2010) detected the CCS emission, which is known as a young gas tracer in cold dark clouds, in the Orion A GMC for the first time. Tatematsu et al. (2014a) mapped six cores of the Orion A GMC in N_2H^+ and CCS, and found that the $N(N_2H^+)/N(CCS)$ ratio is low toward starless core regions while it is high toward star-forming core regions. Thus they suggested that

the $N(N_2H^+)/N(CCS)$ ratio will be an indicator of the chemical evolution not only in cold dark clouds (Suzuki et al., 1992) but also in the Orion A cloud if the gas temperature does not exceed $\sim$ 25 K. For $\gtrsim$ 25 K, N_2H^+ is destroyed by CO evaporation from dust (e.g., Lee et al., 2004). In fact, Reiter et al. (2011) found that N_2H^+ poorly traces dust emission in high mass star-forming regions, and suggested that CO destroys N_2H^+ in the warm gas phase. It is desirable to identify new late-type tracers, which are valid even in such high-temperature regions. Benson et al. (1998) pointed out that c-C_3H_2 column densities are correlated with those of N_2H^+ and anticorrelated with those of CCS. It might indicate that c-C_3H_2 would be a late type tracer like N_2H^+. Sanhueza et al. (2012) also found that HCO^+ is more abundant than N_2H^+ in evolved Infrared Dark Clouds (IRDCs) because HCO^+ is created by a combination of N_2H^+ and CO.

Thanks to recent high sensitivity space telescopes like the *Spitzer Space Telescope* and *Herschel Space Observatory*, protostars deeply embedded in GMC dense cores have also been identified as infrared excess. For instance, Megeath et al. (2012) performed a protostar survey of the Orion A and B molecular clouds undertaken with the IRAC and MIPS instruments on board *Spitzer* and identified 488 protostar candidates.

1.7.2 Nearby GMC in different conditions: Vela C molecular cloud complex

In order to understand the chemical compositions and evolutions in GMC cores in general, it is important to examine the chemical properties of different phases and environments of GMCs and a lot of star-forming dense cores.

The Vela molecular clouds or 'Vela Molecular Ridge' (Murphy & May, 1991) is one of the closest (700 pc; Liseau et al., 1992). GMCs within the Galactic plane, and consists of four components labelled A through D. The Vela C giant molecular cloud complex is the most massive component of the Vela region, and accompanies a bright HII region, RCW 36, associated with an early type star (spectral type O5-B0) (Massi et al., 2003).

Giannini et al. (2012) also performed a protostar survey toward the Vela C molecular cloud complex with with PACS and SPIRE on board *Herschel* and identified 48 sources as protostars based on 70μm excess,. By using these protostellar catalogs, protostellar cores and prestellar cores can be defined as association with protostars. From these definitions, I would like to investigate how chemical compositions are changed from prestellar to protostellar cores assuming that dense

cores evolve from prestellar into protostellar cores.

1.7.3 A starless, chemically-evolved dense core, TUKH 122

Tatematsu et al. (2014a) investigated the chemical evolution toward six dense cores in the Orion A cloud using CCS and N_2H^+ emission. They found that the $N(N_2H^+)/N(CCS)$ can be an chemical evolutional tracer even in GMC with a kinetic temperature < 25 K. In their targets, TUKH122 is a starless but takes the highest ratio of the $N(N_2H^+)/N(CCS) \sim 2-3$ within starless.

Here, we report new single-pointing observations of the NH_3 $(J, K) = (1, 1)$ and $(2, 2)$ emission lines toward the TUKH122 core at 0.05 km s^{-1} velocity resolution using the Nobeyama 45 m telescope in order to investigate the kinematics and the physical conditions of the core. Measurements of the NH_3 inversion lines are ideal for temperature of dense gas (Ho & Townes, 1983). Therefore, we will provide kinetic temperature and turbulence information from a good example of a dense core on the verge of star formation.

1.8 Thesis outline

The outline of this thesis is as follows. In Chapter 2, I present the results of the chemical variations of protostellar and prestellar dense cores located in the Orion A cloud and discuss the chemical evolution and dynamical evolution of the dense cores in this prototypical GMC. In Chapter 3, I show the results of the chemical evolution of dense cores located in another nearby GMC under different environment, the Vela C molecular cloud complex, and test whether the indicators of chemical evolution of dense cores in the Orion A cloud are useful for dense cores in other regions. In Chapter 4, spatial and dynamical structure of a chemically-evolved starless dense core in Orion, TUKH122, will be analyzed via observations in NH_3 $(J, K = 1, 1)$ and $(2, 2)$ lines. An evidence for turbulence dissipation was found. Current results prefer a coherent core scenario as the initial conditions of star formation.

Chapter 2

Chemical evolutions of dense cores in the Orion A cloud

A part of this chapter has been published as Ohashi, Satoshi; Tatematsu, Ken'ichi; Choi, Minho; Kang, Miju; Umemoto, Tomofumi; Lee, Jeong-Eun; Hirota, Tomoya; Yamamoto, Satoshi; & Mizuno, Norikazu, PASJ, 66, 119 (Ohashi et al., 2014b)

Abstract

We carried out mapping observations in N_2H^+, CCS, cyclic C_3H_2, $H^{13}CO^+$, HCO^+, and HCN lines toward six cores in the Orion A cloud with the Nobeyama 45 m telescope and the KVN 21 m telescope. The N_2H^+ and CCS data were observed with the Nobeyama 45 m and other lines were observed with the KVN 21 m telescope. We examined the chemical characteristics of the cores and found a tendency for the column density ratio, N(c-C_3H_2)/N(CCS), to be low in starless regions while it is high in star-forming regions. We also found that $N(H^{13}CO^+)$ is enhanced in cluster-forming regions compared with those in isolated star-forming regions. Furthermore, we found that the $N(NH_3)/N$(CCS) and $N(NH_3)/N(HC_3N)$ ratios are high in star-forming cores and low in starless cores in the Orion A cloud for a wide range of the kinetic temperature, T_k = 10 to 60 K. We suggest that the $N(NH_3)/N$(CCS), $N(NH_3)/N(HC_3N)$, and $N(N_2H^+)/N$(CCS) ratios may be indicators of chemical evolution in GMCs, including warmer regions. From a comparison between cores associated with protostars and cores without protostars through virial analysis, we also suggest that the dissipation of turbulence initiates star formation. Finally, we found that the $N(NH_3)/N$(CCS) ratio increases with the dissipation of turbulence. This may suggest that the chemical evolution can be an indicator of the dynamical evolution of the core.

2.1 Introduction of this chapter

The Orion A cloud is one of the nearest GMCs form the earth. Therefore, it is relatively easy to detect weak molecular lines such as CCS and HC_3N. Furthermore, physical conditions of the Orion A cloud cores have been well studied by many observations.

The Orion A cloud has a filamentary structure elongated in the north-south direction. Many observations have identified active star-forming sites in the Orion A cloud (e.g., Genzel & Stutzki, 1989; Strom et al., 1993; Chini et al., 1997; Megeath et al., 2012). The OMC-2/3 region is located on the northern end of the filament and one of the most active star-forming regions in the Orion A cloud. Dense cores of this region were studied by Tatematsu et al. (1993); Cesaroni & Wilson (1994); Aso et al. (2000); Takahashi et al. (2013). Cesaroni & Wilson (1994) estimated the gas kinetic temperature of dense cores in the OMC-2/3 region to be $\sim$ 20 K, which is higher than the typical value of 10 K in dark clouds cores (e.g., Benson & Myers, 1980). Megeath et al. (2012) carried out the protostars identification using IRAC and MIPS data and cataloged the protostars in the Orion A and B clouds. The Megeath catalog shows many protostars, and it is clear that the Orion KL cluster (e.g., Genzel & Stutzki, 1989) and the OMC-2/3 region are star-forming sites much more active than the other part of the cloud. However, it is not clear why star forming activities differ from place to place. Aso et al. (2000) observed the OMC-2/3 region in the HCO^+ (1$-$0) and $H^{13}CO^+$ (1$-$0) lines. They performed virial analysis with external pressure, and compared the properties of cores associated with protostars and those without protostars. They suggested that the dissipation of turbulence initiates star formation. However, the $H^{13}CO^+$ emission might be affected by outflows (e.g., Tatematsu et al., 2008). It is desirable to investigate the properties of cores using quiescent core tracers such as N_2H^+. The Orion A cloud has previously been observed in using HCN, HCO^+, and $H^{13}CO^+$ (e.g., Rydbeck et al., 1981; Ungerechts et al., 1997). From these observations, it seems that HCN, HCO^+ distribution is more or less similar and traces dense gas regions. These lines are most likely optically thick. The $H^{13}CO^+$ line, which is optically thin, is often used to identify the dense cores as well as N_2H^+ (e.g., Ikeda et al., 2007; Onishi et al., 2002). In extragalactic nuclei, it is recently suggested that HCN/HCO^+ abundance ratio varies between AGN-host galaxies and pure starburst galaxies because of high temperature chemistry (e.g., Izumi et al., 2013). Therefore, we are interested in differences of HCO^+ and HCN molecular lines on the GMC core scale.

In this study, we investigate the chemical and physical evolution of cores through mapping observations of N_2H^+, cyclic C_3H_2, CCS, $H^{13}CO^+$, HCO^+, and HCN lines. We also analyze NH_3, HC_3N, and CCS data taken from Tatematsu et al. (2010); Wilson et al. (1999). We expect that N_2H^+, NH_3, and cyclic C_3H_2 are chemically evolved tracers while CCS and HC_3N are chemically young type tracers even in GMCs. The purpose of this study is 1) to find a molecule which is a better chemical tracer than N_2H^+, 2) to understand how different the chemical properties of molecular cloud cores in the GMC are, compared with those in cold dark clouds, and 3) to investigate the physical parameters between starless cores and star-forming cores in the GMC and understand what initiates star formation using N_2H^+.

2.2 Observations toward the Orion A cloud

We observed cyclic C_3H_2 ($J_{K_aK_c} = 2_{12} - 1_{01}$), $H^{13}CO^+$ ($J = 1 - 0$), HCO^+ ($J = 1 - 0$), and HCN ($J = 1 - 0$) lines toward the six cores in the Orion A cloud with the KVN 21 m antennas in the single-dish telescope mode. The target cores are TUKH003, 021, 088, 097, 117, and 122. TUKH refers to the core catalog by Tatematsu et al. (1993). The positions of these cores are shown in Figure 2.1. We selected these cores because Tatematsu et al. (2010) detected in CCS $J_N = 4_3 - 3_2$ emission at 45 GHz toward these cores.

The observations were carried out with the KVN Tamna telescope from 2013 March 17 to June 5, and with the KVN Ulsan telescope from 2013 March 23 to 25. The data were obtained using the high-electron-mobility-transistor (HEMT) receiver for 86 GHz band. Digital filters and spectrometers were used as the back end. The details of KVN telescopes are given in Lee et al. (2011) and Kim et al. (2011). The half-power beam width (HPBW) and main beam efficiency $\eta_{\rm MB}$ of the telescope is 31.5 arcsec and 39 %, respectively. All the observations were done in position switching mode. All the maps were made on a 7 x 7 grid at a spacing of 20 arcsec, and the map center positions are taken from the core catalog of Tatematsu et al. (1993). The reference positions were (Δ R. A., Δ Dec.) = ($-30'$, $0'$) with respect to the map center except for TUKH088. For TUKH088, the reference position was (Δ R. A., Δ Dec.) = ($-60'$, $0'$) because (Δ R. A., Δ Dec.) = ($-30'$, $0'$) position of TUKH088 was detected in the HCO^+ emission. The rms noise level in the 86 GHz observations are $\sim$ 0.5 K at 30 kHz resolution. The observed data were reduced using the software package "CLASS".

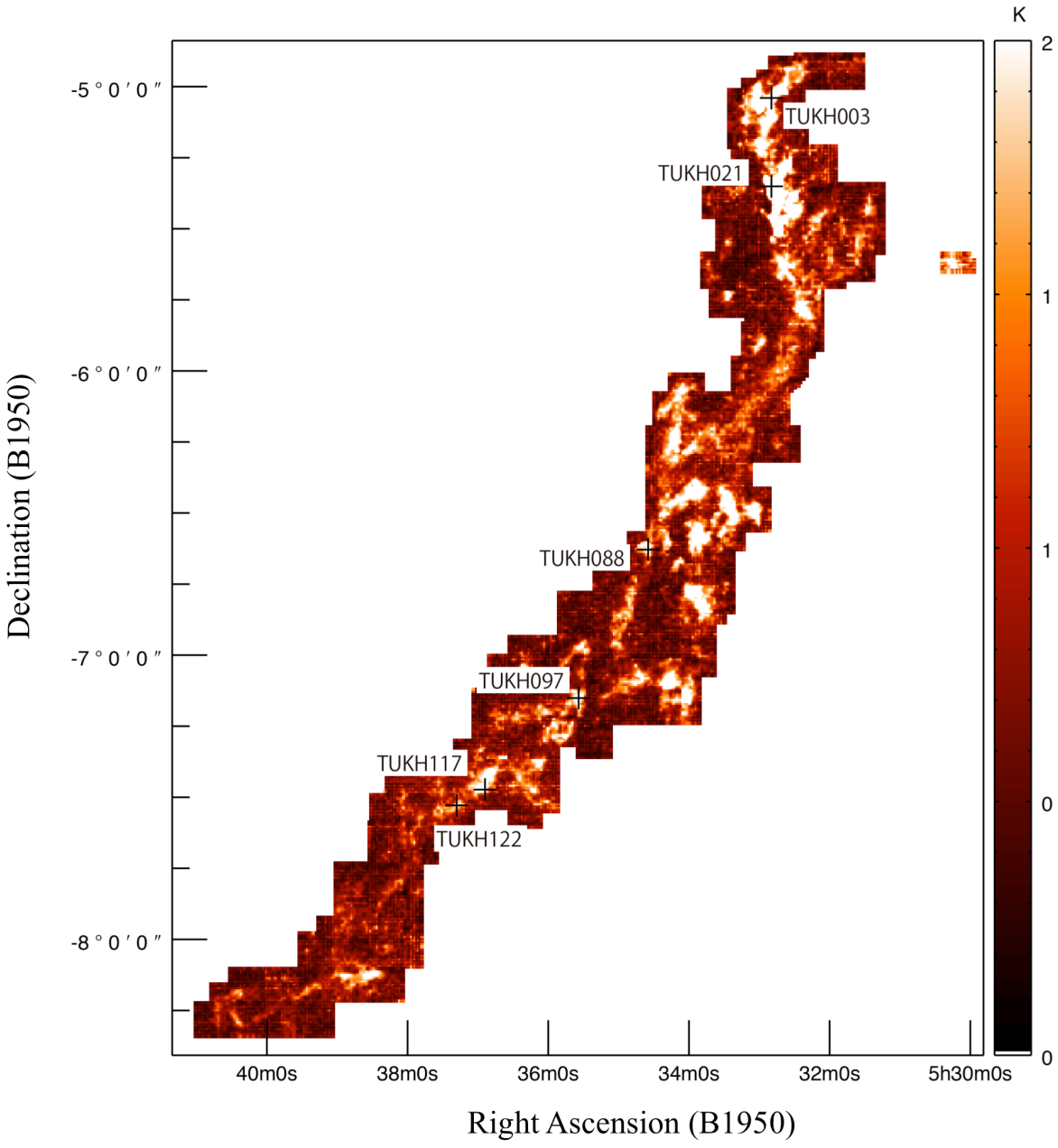

Figure 2.1: The positions of the observed cores. The color is the CS $J = 1 - 0$ peak intensity map (Tatematsu et al., 1993).

We also observed N_2H^+ (J = 1−0) and CCS (J_N = 7_6−6_5) lines toward the same cores with the Nobeyama 45 m telescope from 2013 January 13 to 24. The employed receiver front end was the single-beam two-polarization two-sideband-separation (2SB) SIS receiver "TZ1" (Asayama & Nakajima, 2013; Nakajima et al., 2013). We observed N_2H^+ $J = 1 - 0$ in the V (vertical) polarization and CCS $J_N = 7_6 - 6_5$ emission in the both polarization, simultaneously. The upper energy level E_u for each transition are 4.3 and 15.3 K, respectively. The HPBW and main beam efficiency of the telescope is 19.1 arcsec and 41% at 86 GHz, respectively. We used "SAM45" at the receiver back end digital spectrometer. The spectral resolution was 30.52 kHz, corresponding to ~ 0.1 km s^{-1}. The observations were done in position switching mode and their spacing was 20 arcsec. The reference positions were (Δ R. A., Δ Dec.) = ($-30'$, $0'$) with respect to the map center. The rms noise level in the CCS observations are ~ 0.06 K at 30 kHz resolution. The noise level in the N_2H^+ observations is about $\sqrt{2}$ times higher than the rms in CCS because of the single polarization observations. The observed data were reduced using the software package "Newstar"

The observational parameters are summarized in table 2.1

Table 2.1: Summary of observed molecular lines

Molecule	Transition	Rest frequency (GHz)	Telescope	Beam size (")
N_2H^+	$J = 1 - 0$	93.173777	Nobeyama 45 m	20
CCS	$J_N = 7_6 - 6_5$	81.505208	Nobeyama 45 m	20
cyclic C_3H_2	$J_{K_aK_c} = 2_{12} - 1_{01}$	85.338906	KVN 21 m	31.5
$H^{13}CO^+$	$J = 1 - 0$	86.754288	KVN 21 m	31.5
HCO^+	$J = 1 - 0$	89.188526	KVN 21 m	31.5
HCN	$J = 1 - 0$	88.630415	KVN 21 m	31.5

2.3 Results of the Orion A cloud

Figures 2.2 to 2.7 show the velocity integrated intensity maps of N_2H^+ J = 1−0 F_1 = 2−1, CCS $J_N = 7_6 - 6_5$, c-C_3H_2 $J_{K_aK_c} = 2_{12} - 1_{01}$, $H^{13}CO^+$ J = 1−0, HCN J = 1−0, and HCO^+ J = 1−0 emissions. We also plot the locations of the protostars identified as Class 0 or I by Megeath et al. (2012). The TUKH003 and 021 core regions accompany eight and nine protostars, respectively. On the other hand, the TUKH088, TUKH097, and TUKH117 core regions accompany only one or two protostars. Thus, we define the TUKH003 and 021 cores as cluster forming and define the TUKH088, 097, and 117 as the isolated star-forming region. From figures 2.2 to 2.7, we see

that there are some displacements of peak positions between c-C_3H_2 and $H^{13}CO^+$. This might be caused by chemical evolution, discussed in the subsequent section. The HCO^+ and HCN emissions were detected in almost all the positions. Those distributions are similar. To investigate the chemical characteristics and compare the column densities of these lines in these cores, we identified 36 positions that were detected in N_2H^+, c-C_3H_2, and $H^{13}CO^+$ emissions at more than 3 σ noise levels in the six molecular cloud cores. We labeled these positions as "A, B, C, ..." after core number TUKH (table 2.3). Tatematsu et al. (2014a) also identified local peaks of CCS ($J_N = 7_6 - 6_5$) or N_2H^+ ($J = 1-0$) and labeled in the same way. To avoid confusion, our labels are continued from Tatematsu et al. (2014a). The underlined TUKH numbers of table 2.3 indicate starless regions, while the others are star-forming regions.

2.3.1 Individual core

In the TUKH003 region (figure 2.2), all the emission lines were strongly detected. This region is well known as the OMC-3, which is an active star-forming site and has a filamentary structure along north-south direction. The protostars are distributed along the filamentary structure. The c-C_3H_2 and $H^{13}CO^+$ distributions are similar to that of N_2H^+ and all these peak positions are located in the center of the filament corresponding to "003B". The HCN and HCO^+ molecules are widely distributed and they are intense toward the northwestern region. This can be explained by two factors. First, the optical depth will be large in the HCO^+ and HCN emission lines, and they cannot trace the inner high density region. Second, the HCO^+ and HCN are sensitive to the temperature because of the optical thickness. In fact, Li et al. (2013) derived the kinetic temperature $\sim$ 20 K toward the northeastern region using NH_3 (1,1) and (2,2) lines. Note that the eastern region (R.A. $>$ 5 h 35 m 22.3 s) was not observed with the KVN telescope.

The TUKH021 region (figure 2.3) contains several protostars and is the most active star-forming region in our observed cores. All the emission lines were strongly detected. The c-C_3H_2 and $H^{13}CO^+$ distribution are more or less similar to the N_2H^+ distribution, but there are some differences in the local peak positions. In the eastern region, there is a local peak of c-C_3H_2 but neither N_2H^+ nor $H^{13}CO^+$ emission was detected. Tatematsu et al. (2014a) detected the CCS ($J_N = 7_6 - 6_5$) emission in this position and labeled as "TUKH021B" in their study. It might be suggested that this region is "Carbon-Chain-Producing Regions (CCPRs)" (Sakai et al., 2008a;

Hirota et al., 2009) despite the fact that the protostar is associated with this region. However, this region is located a few acrmin north of Orion-KL, and the kinetic temperature changes from 18 to 45 K on small scales (Wiseman & Ho, 1998). It is not clear whether the chemical properties are affected by the stellar radiation or temperature variation. The carbon-chain molecules of CCS may also be produced by shocks such as outflow. Yamaguchi et al. (2012) detected CCS emission in the L 1157 B1 shocked region driven by an outflow.

In the TUKH088 (Figure 2.4), the KVN observations did not cover the N_2H^+ peak position, which corresponds to a position of a protostar. However, all the emission lines become intense toward the protostar. In this region, the distributions of these lines are relatively similar, in contrast with the TUKH003 and 021 cluster regions. In the north, there is the $H^{13}CO^+$ intensity peak "088A". This $H^{13}CO^+$ peak position "088A" corresponds with CCS ($J_N = 7_6 - 6_5$) intensity peak position.

TUKH097 region (Figure 2.5) contains two protostars. The peak position of $H^{13}CO^+$ emission of "097A" corresponds with the CCS peak position. The distributions of all the emission are similar. The protostars are associated with local peaks of the c-C_3H_2 and the $H^{13}CO^+$ emission, taking into account the beam size.

The TUKH117 region (Figure 2.6) is associated with two protostars, one of them is Haro 4-255 FIR (Megeath catalog number 551), which drives a molecular outflow (Evans et al., 1986; Levreault, 1988). We have detected wing profiles in the HCO^+ and HCN emission. All the emission lines except for CCS are intense toward the core center. In contrast, CCS emission is distributed around the N_2H^+ core. Thus, the c-C_3H_2 and the $H^{13}CO^+$ distribution is anticorrelated with the CCS distribution. Since this core already form the protostar and has the outflow, it is unlikely that the CCS molecule is depleted in the center position. We suggest that these anticorrelated distribution may be explained by the chemical evolution.

The TUKH122 region (Figure 2.7) is starless. We found that the $H^{13}CO^+$ peak position located in the northwestern region corresponds to the CCS ($J_N = 7_6 - 6_5$) local peak position identified as "TUKH122A" by Tatematsu et al. (2014a).

We summarize the general tendency found in our observations. The c-C_3H_2 and $H^{13}CO^+$ distribution resembles the N_2H^+ distribution. However, the peak positions of $H^{13}CO^+$ correspond to the CCS ($J_N = 7_6 - 6_5$) emission peak positions in the TUKH088 and 122 cores. Thus, $H^{13}CO^+$

traces high dense region but it will be depleted in cold dense region. The c-C_3H_2 distribution is similar to the N_2H^+ distribution rather than CCS, suggesting that c-C_3H_2 traces not chemically young gas but evolved gas. The properties and chemical differences of these molecules will be discussed later.

2.3.2 Hyperfine fitting and derivation of physical parameter

Table 2.2 lists the physical parameters of N_2H^+ cores. We fitted the hyperfine component model to the N_2H^+ spectra, and derived the optical depth, LSR velocity, linewidth, and excitation temperature assuming a uniform excitation temperature in the N_2H^+ hyperfine components. The intrinsic line strengths of the hyperfine components are adopted from Tiné et al. (2000). The optical depth $\tau_{\rm tot}$ is the sum of the peak optical depths of all the hyperfine components. In TUKH003, TUKH097, and TUKH117, we identified two velocity components and fitted by using the two-component hyperfine model. Figure 2.8 shows the examples of hyperfine-fitting results in the peak positions of the cores. If we identified two velocity components, we only use the column densities of the main components. Peak positions are listed in table 2.2, and in Tatematsu et al. (2014a) corresponds to 003B, 021I, 088B, 097C, 117C, and 122C. The column density is calculated by assuming local thermodynamic equilibrium (LTE). The formulation can be found, for example, in Furuya et al. (2006). The fitting results of the optical depth and the excitation temperature range $\tau = 0.7 - 30$ and $T_{\rm ex} = 4 - 30$ K (see also table 2.2).

The HWHM (half of FWHM) core radius R is defined as $\sqrt{S}/\pi$, where S is the core area at the half-maximum level of the N_2H^+ integrated intensity. The core mass $M_{\rm LTE}$ was derived by assuming the N_2H^+ fractional abundance relative to H_2, 3.0×10^{-10} (Caselli et al., 2002).

Table 2.2: Physical parameter of the N_2H^+ cores

TUKH	Peak Position R.A. (h:m:s)	Decl. (°:′:″)	$R_{\rm core}$ (N_2H^+) (pc)	τ(N_2H^+)	$T_{\rm ex}$(N_2H^+) (K)	N(N_2H^+) (cm^{-2})	$M_{\rm LTE}$ ($M_\odot$)
003	5:35:19.0	−5:00:29.1	0.08	5.7±1.1	11.2±0.7	(3.7±0.1) E+13	54
021	5:35:17.3	−5:19:12.8	0.09	3.3±0.7	20.8±1.8	(9.7±0.9) E+13	180
088	5:37:0.5	−6:37:19.2	0.03	5.4±1.3	4.8±0.2	(1.5±0.4) E+13	3.1
097	5:37:57.8	−7:07:2.1	0.06	4.2±1.0	7.5±0.5	(2.1±0.2) E+13	17
117	5:39:19.7	−7:26:7.5	0.04	4.5±1.0	11.0±0.8	(4.4±0.3) E+13	20
122	5:39:42.5	−7:29:50.3	0.08	20.3±3.4	4.0±0.1	(1.1±0.1) E+13	16

Table 2.3 lists the column densities of the observed molecules toward the identified intensity

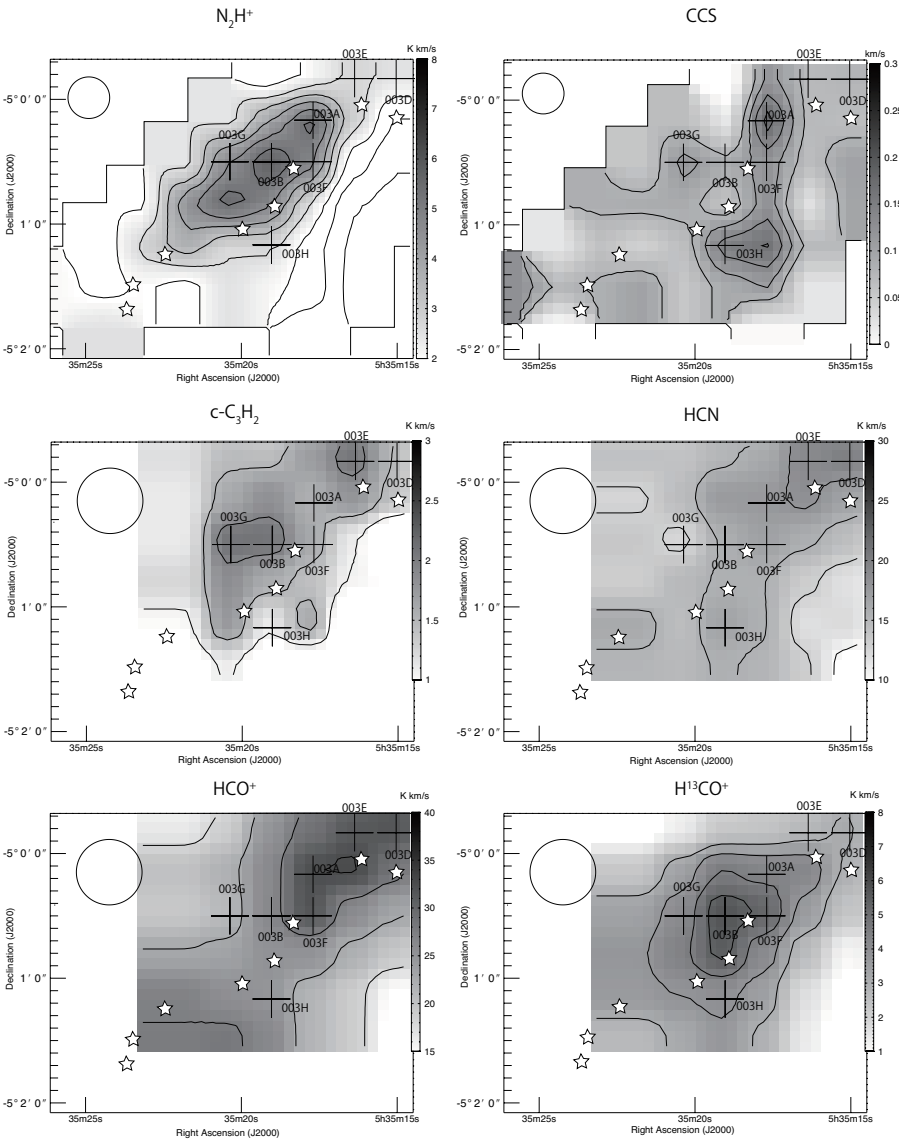

Figure 2.2: Velocity-integrated intensity maps. The velocity range for integration is 8.0 to 13.0 km s^{-1}. The top panels show the N_2H^+(1-0, F_1 = 2−1) and CCS ($J_N = 7_6 - 6_5$) maps. The contours start at 20 σ in N_2H^+ and 3 σ in CCS. The interval is 20 σ in N_2H^+ and 1 σ in CCS (1 σ is 0.033 and 0.027 K km s^{-1}, respectively). The middle panels show c-C_3H_2($J_{K_aK_c} = 2_{12} - 1_{01}$) and HCN (1-0) maps. The contours start at 3 σ in c-C_3H_2 and 12 σ in HCN. The interval is 1.2 σ in c-C_3H_2 and 3 σ in HCN (1 σ is 0.36 and 0.86 K km s^{-1}, respectively). The bottom panel shows HCO^+(1-0) and $H^{13}CO$ maps. The contours start at 15 σ in HCO^+ and 8 σ in $H^{13}CO^+$. The interval is 4 σ in HCO^+ and 2 σ in $H^{13}CO^+$ (1 σ is 1.2 and 0.38 K km s^{-1}, respectively). The open star signs represent the location of the protostar in Megeath et al. (2012). The white circle represents the beam size of the Nobeyama 45 m and the KVN 21 m telescopes. The cross signs represent the location of core intensity peaks.

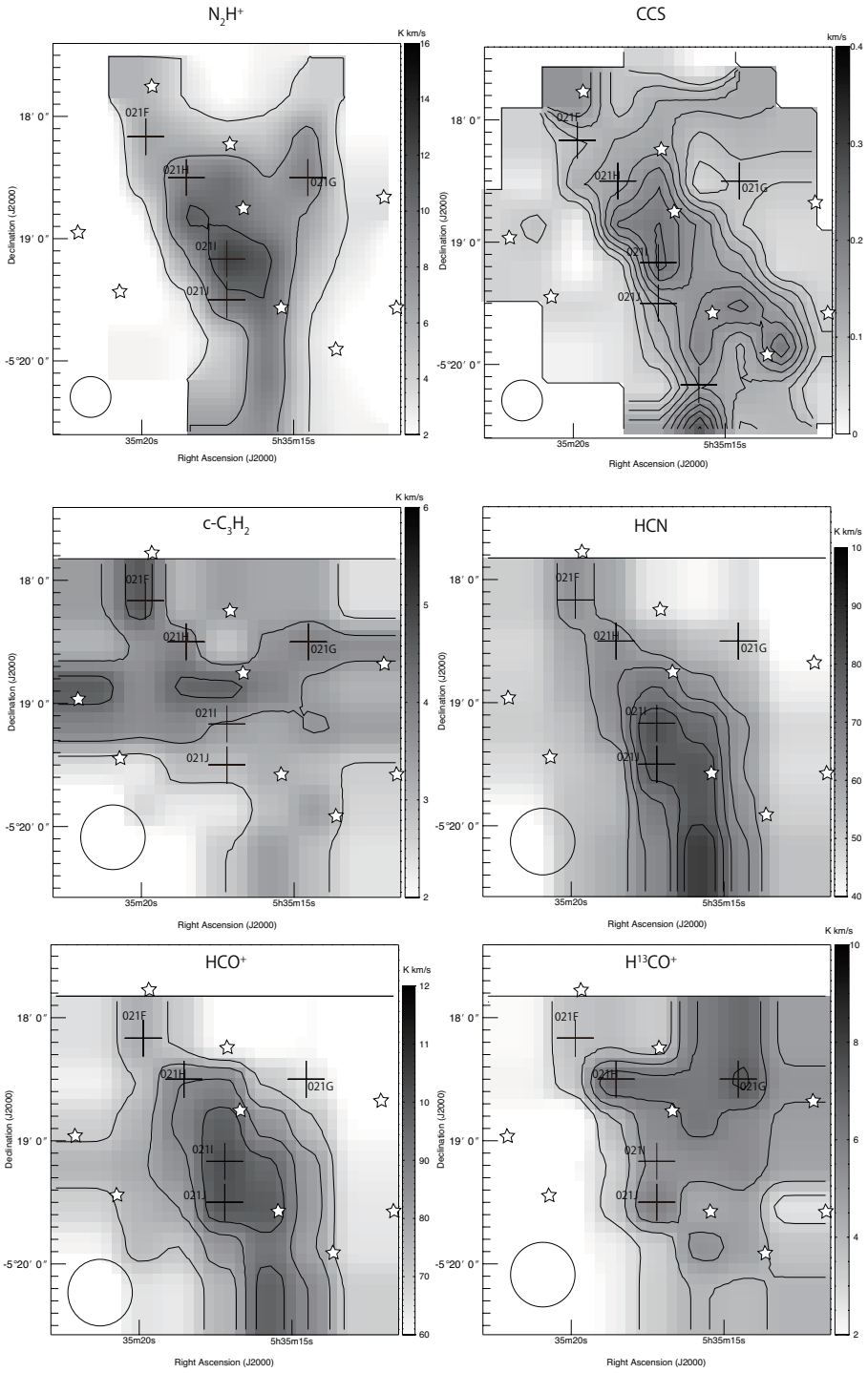

Figure 2.3: The same as Figure 2.2 but for TUKH021. The velocity range for integration is 8.0 to 12.0 km s^{-1}. The contours start at 15 σ in N_2H^+, 3 σ in CCS, 6 σ in c-C_3H_2, 6 σ in $H^{13}CO^+$, 120 σ in HCN and 140 σ in HCO^+. The interval is 15, 1, 1.8, 2, 10, and 15 σ. (1 σ is 0.231, 0.046, 0.45, 0.50, 0.51, and 0.51 K km s^{-1}, respectively).

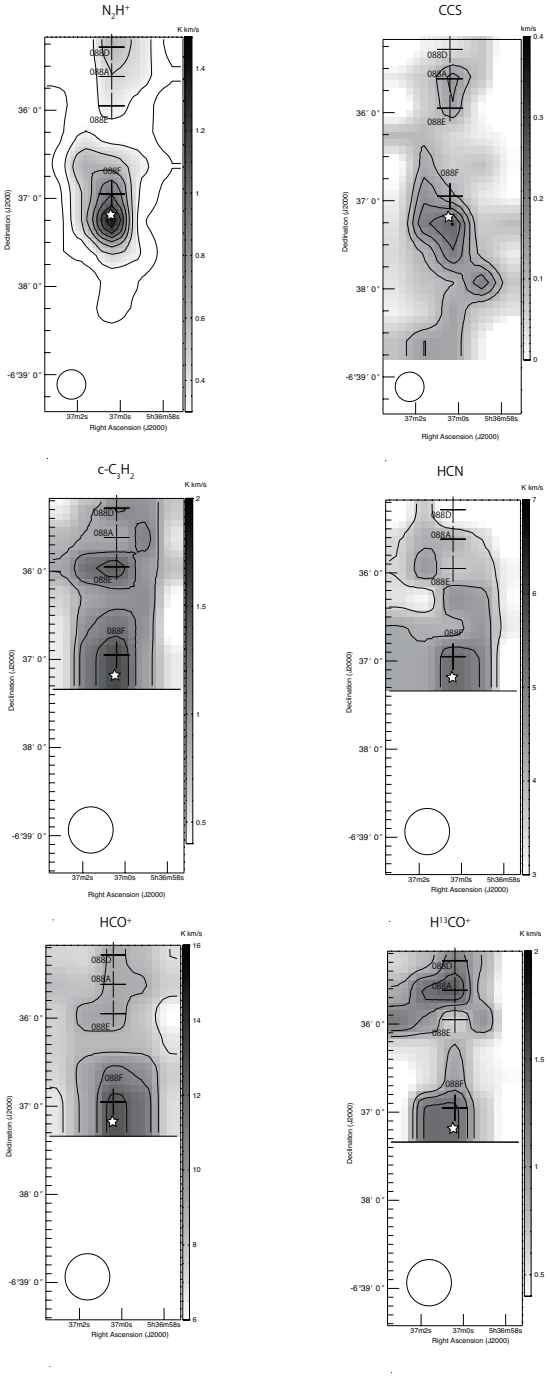

Figure 2.4: The same as Figure 2.2 but for TUKH088. The velocity range for integration is 4.5 to 7.5 km s^{-1}. The contours start at 3 σ in N_2H^+, 3 σ in CCS, 4 σ in c-C_3H_2, 4 σ in $H^{13}CO^+$, 10 σ in HCN and 20 σ in HCO^+. The interval is 3, 1, 1, 1, 2, and 5 σ. (1 σ is 0.0531, 0.034, 0.22, 0.21, 0.35, and 0.35 K km s^{-1}, respectively).

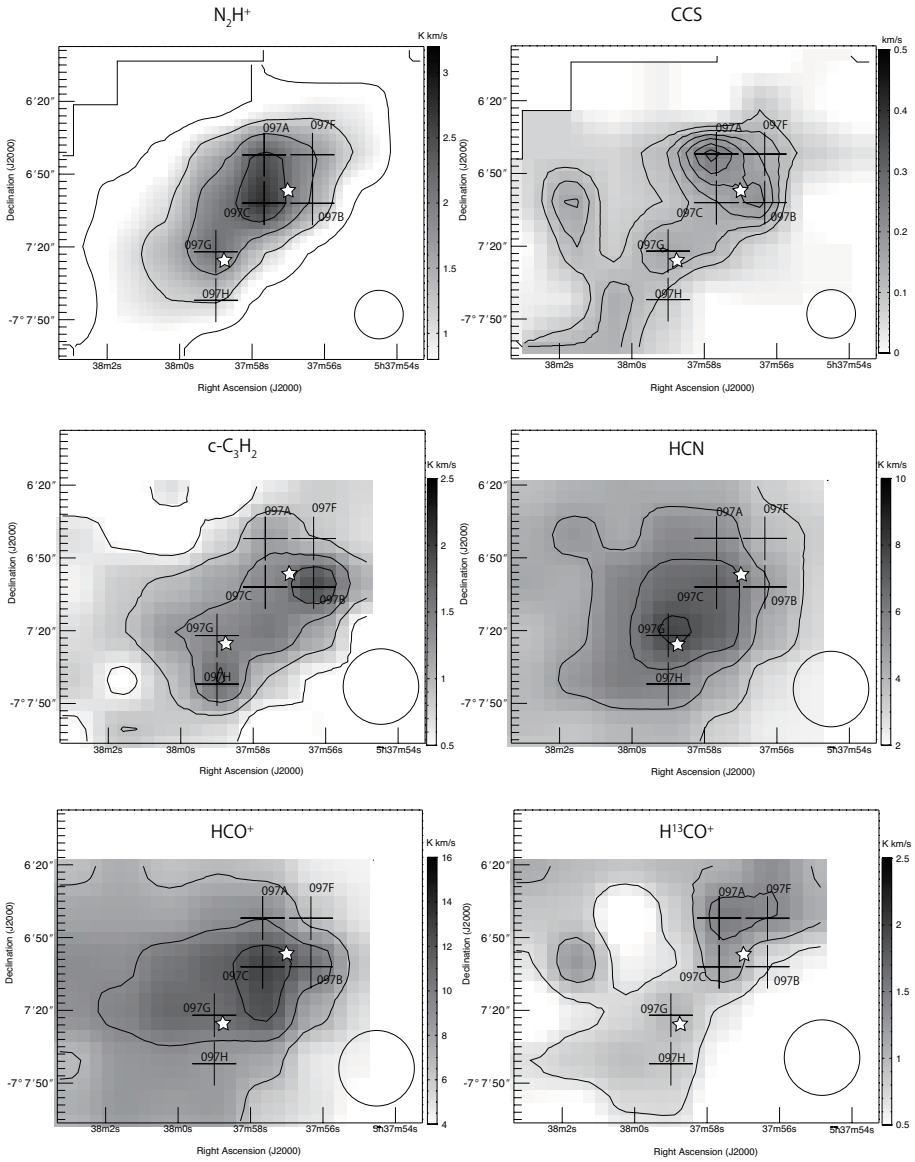

Figure 2.5: The same as Figure 2.2 but for TUKH097. The velocity range for integration is 4.2 to 7.8 km s^{-1}. The contours start at 10 σ in N_2H^+, 3 σ in CCS, 3 σ in c-C_3H_2, 3 σ in $H^{13}CO^+$, 10 σ in HCN and 9 σ in HCO^+. The interval is 10, 1, 2, 1.5, 4, and 3 σ. (1 σ is 0.0564, 0.031, 0.18, 0.23, 0.34, and 0.78 K km s^{-1}, respectively).

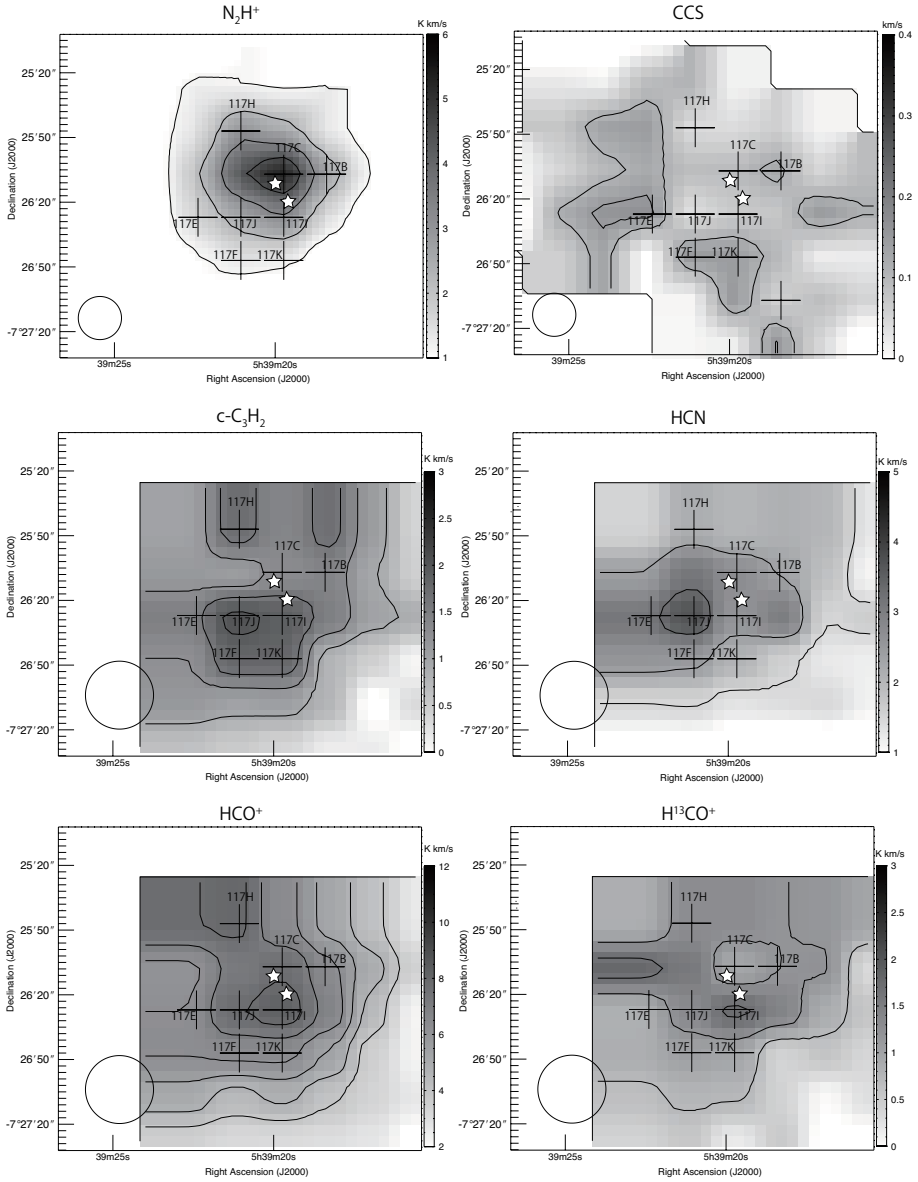

Figure 2.6: The same as Figure 2.2 but for TUKH117. The velocity range for integration is 2.9 to 6.5 km s^{-1}. The contours start at 6 σ in N_2H^+, 3 σ in CCS, 4 σ in c-C_3H_2, 3 σ in $H^{13}CO^+$, 5 σ in HCN and 10 σ in HCO^+. The interval is 6, 1, 1.5, 2, 3, and 2 σ. (1 σ is 0.185, 0.037, 0.23, 0.24, 0.30, and 0.39 K km s^{-1}, respectively).

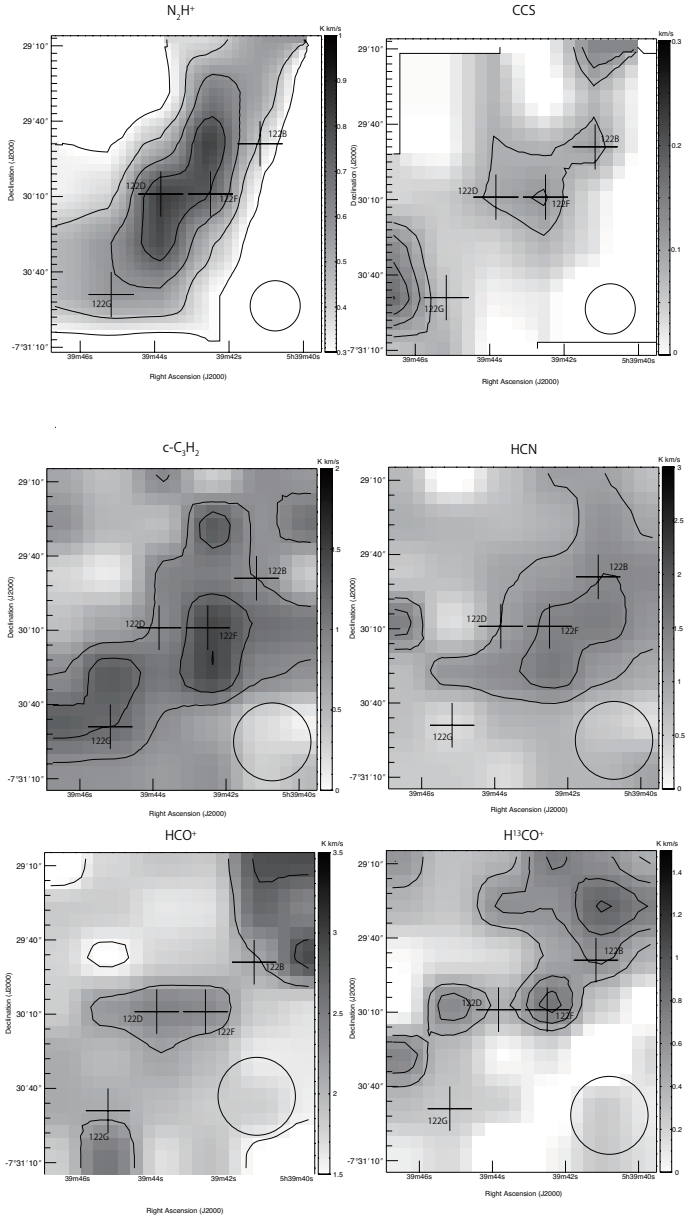

Figure 2.7: The same as Figure 2.2 but for TUKH122. The velocity range for integration is 2.6 to 5.1 km s^{-1}. The contours start at 4 σ in N_2H^+, 3 σ in CCS, 3 σ in c-C_3H_2, 3 σ in $H^{13}CO^+$, 3 σ in HCN and 3 σ in HCO^+. The interval is 2, 1, 1, 2, 1, and 2 σ. (1 σ is 0.0727, 0.028, 0.29, 0.15, 0.34, and 0.31 K km s^{-1}, respectively).

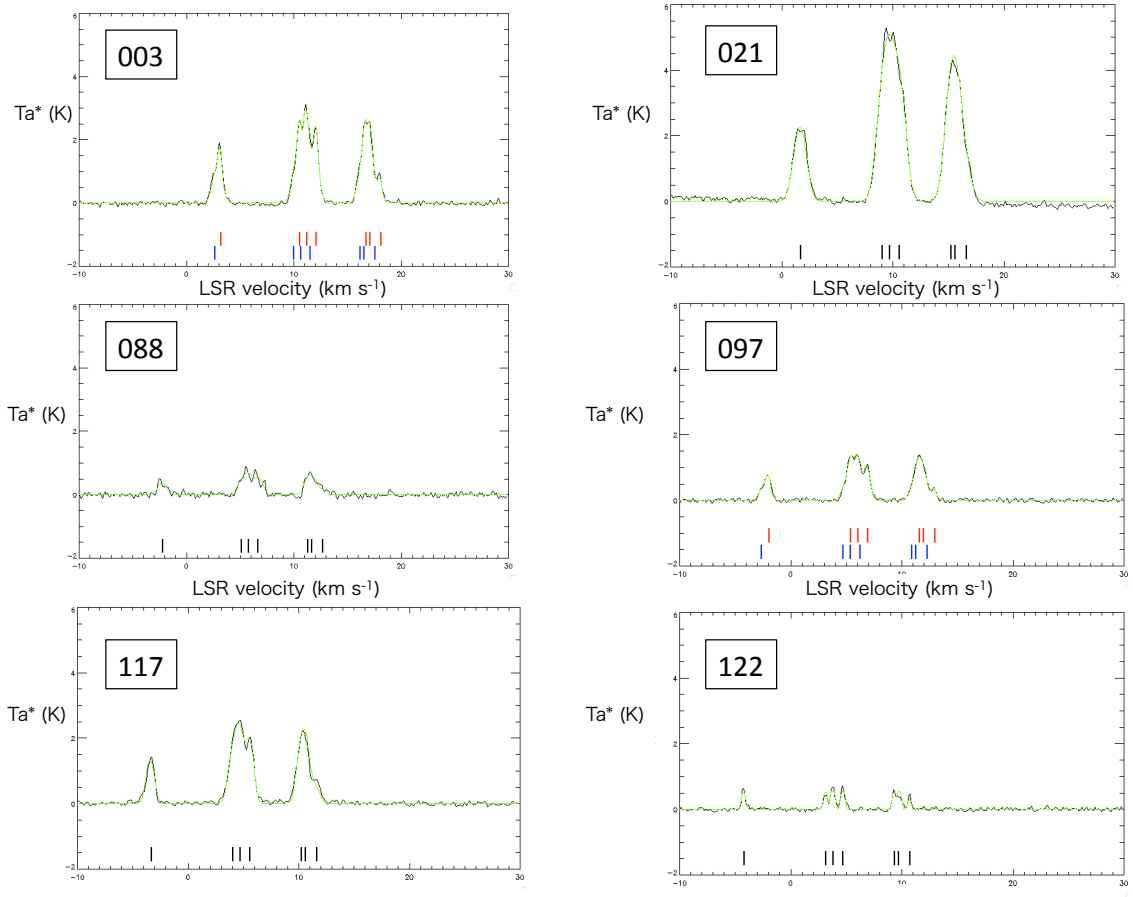

Figure 2.8: Hyperfine line fitting result for the N_2H^+ (J = 1−0) spectrum for the six cores. Seven short vertical bars are shown to illustrate the velocity offset corresponding to the frequency offset of the hyperfine components, blue and red color bars represent two components fitting.

peaks. The "three dots" indicates either "not observed" or "omitted because the noise level is too high". We performed Gaussian fitting to the HCO^+, $H^{13}CO^+$, and c-C_3H_2 line profiles. From HCO^+ and $H^{13}CO^+$ lines, we can derive the optical depth and excitation temperature, by assuming the $[^{12}C]/[^{13}C]$ abundance ratio $\sim$ 68 (Milam et al., 2005). We also derive those of c-C_3H_2 assuming the excitation temperature is equal to the rotation temperature which is derived by NH_3 (1,1) and (2,2) lines (Wilson et al., 1999).

Table 2.3: Coordinate, Column Density of N_2H^+, c-C_3H_2, $H^{13}CO^+$, and CCS

TUKH[1,2]	R.A. (J2000) h m s	Decl. (J2000) ° ′ ″	$N(N_2H^+)$[1] (10^{13} cm^{-2})	N(c-C_3H_2)[1] (10^{13} cm^{-2})	$N(H^{13}CO^+)$[1] (10^{13} cm^{-2})	N(CCS)[2] (10^{13} cm^{-2})	$\tau(HCO^+)$
003A	5:35:17.7	-5:00:10.0	5.3		0.41	0.27	21
003B	5:35:19.0	-5:00:30.0	4.2	2.2	0.61	0.15	39
003D	5:35:15.0	-4:59:50.0	1.8	1.5	0.29	< 0.33	23
003E	5:35:16.4	-4:59:50.0	1.9	2.1	0.28	...	21
003F	5:35:17.7	-5:00:30.0	2.3	1.4	0.56	...	33
003G	5:35:20.4	-5:00:30.0	4.4	2.2	0.38	< 0.23	36
003H	5:35:19.0	-5:01:10.0	1.3	1.0	0.38	< 0.32	23
021F	5:35:19.9	-5:18:10.0	6.4	6.9	0.38	< 0.89	7
021G	5:35:14.5	-5:18:30.0	0.42	5.7	0.91	< 0.46	12
021H	5:35:18.5	-5:18:30.0	8.9	5.8	0.97	< 0.39	7
021I	5:35:17.2	-5:19:10.0	15	4.8	0.85	< 0.43	6
021J	5:35:17.2	-5:19:30.0	11	4.2	0.92	...	4
088A	5:37:00.4	-6:35:37.0	0.70	1.5	0.14	5.3	34
088D	5:37:00.4	-6:35:17.0	0.40	1.7	0.17	< 0.46	19
088E	5:37:00.4	-6:35:57.0	0.20	1.4	0.08	< 0.79	13
088F	5:37:00.4	-6:36:57.0	0.82	1.6	0.11	< 0.96	13
097A	5:37:57.7	-7:06:42.0	1.8	0.9	0.14	0.42	17
097B	5:37:56.3	-7:07:02.0	1.2	1.2	0.06	0.77	18
097C	5:37:57.7	-7:07:02.0	2.1	1.1	0.12	0.33	11
097F	5:37:56.3	-7:06:42.0	1.2	0.7	0.14	< 0.20	20
097G	5:37:59.0	-7:07:22.0	1.7	0.9	0.10	< 0.20	8
097H	5:37:59.0	-7:07:42.0	0.70	1.2	0.12	< 0.23	8
117B	5:39:18.4	-7:26:07.0	1.9	0.8	0.12	0.08	21
117C	5:39:19.7	-7:26:07.0	4.4	0.9	0.07	0.2	25
117E	5:39:22.4	-7:26:27.0	1.0	1.0	0.08	0.6	16
117F	5:39:21.1	-7:26:47.0	1.0	1.5	0.12	0.56	19
117H	5:39:21.1	-7:25:47.0	2.5	1.3	0.09	< 0.18	22
117I	5:39:19.7	-7:26:27.0	2.2	1.4	0.15	< 0.16	26
117J	5:39:21.1	-7:26:27.0	1.7	1.2	0.12	< 0.16	16
117K	5:39:19.7	-7:26:47.0	0.91	1.2	0.10	< 0.20	21
122B	5:39:41.2	-7:29:49.0	0.67	0.7	0.35	6.2	284
122D	5:39:43.8	-7:30:09.0	1.3	1.2	0.04	1.2	30
122F	5:39:42.5	-7:30:09.0	1.3	1.3	0.09	1.9	40
122G	5:39:45.2	-7:30:49.0	0.82	0.9	0.05	< 0.20	55

2.3.3 HCN anomalous profiles

HCN (1−0) rotational transition has hyperfine structure as N_2H^+ does, and shows three hyperfine components. In the optically thin limit, these three emission lines have intrinsic intensity ratios of 1:5:3. However, the strengths of individual lines are often seen to be boosted or suppressed beyond what is expected from an LTE analysis or even from LVG analysis (e.g., Walmsley et al., 1982; Loughnane et al., 2012). In our observations, we found that the linewidths of the HCN

[1]This study
[2]Tatematsu et al. 2014

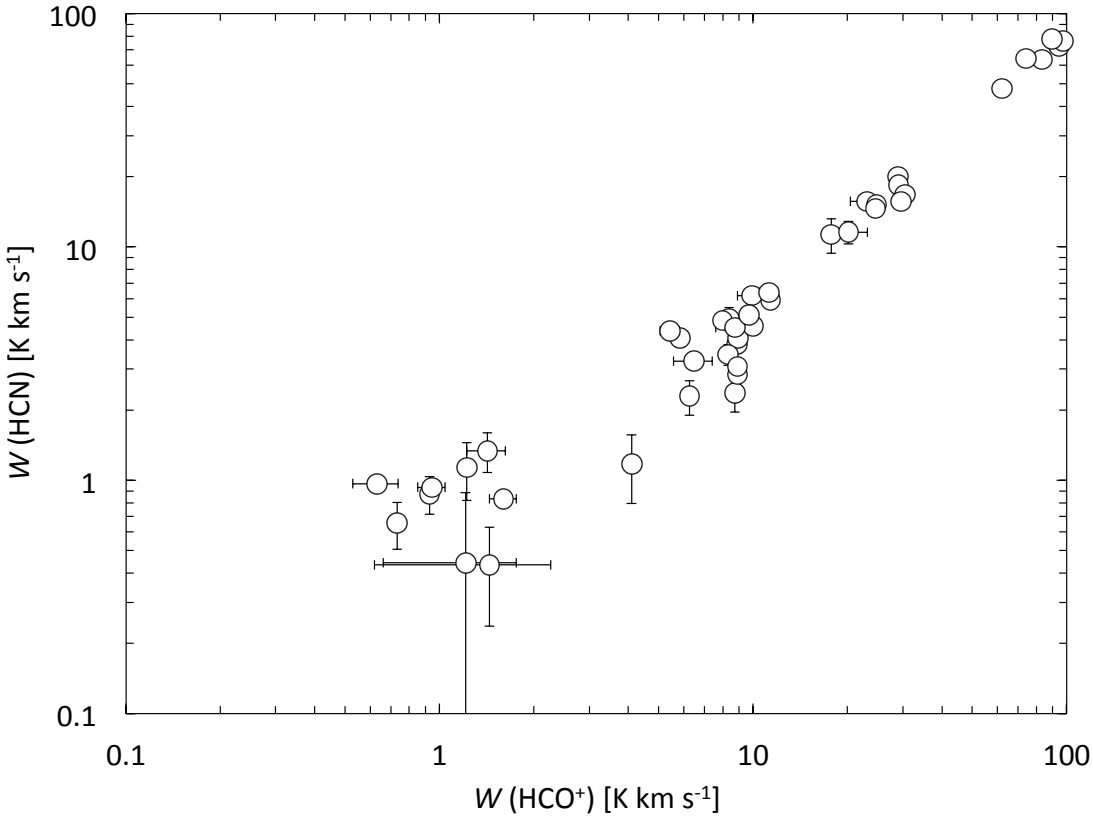

Figure 2.9: The integrated intensity of HCO^+ is plotted against the integrated intensity of HCN. The error bars represent 1 σ noise level.

(J=1−0, F=1−1) and (J=1−0, F=0−1) are increased. This is similar to what was observed in HCN emission toward the G333 massive star-forming region (Loughnane et al., 2012). Due to HCN anomalous profiles, we conclude that it is difficult to obtain the excitation temperature or optical depth, reliably. Figure 2.9 compares integrated intensity of HCO^+ $J = 1 - 0$ with that of HCN $J = 1 - 0, F = 2 - 1$. These plots are from each observing positions in all the maps with both HCN and HCO^+ detections. This figures shows strong correlation between HCO^+ and HCN integrated intensity. Therefore, we suggest that HCN traces the same dense gas with HCO^+ and they behave in a same way. We do not see any hint of HCN excess with respect to HCO^+ (e.g., Izumi et al., 2013; Kohno et al., 2001), probably because our regions do not contain very warm ($>$ 300 K) temperature causing warm gas chemistry.

2.4 Chemical variation in the Orion A GMC

To establish the chemical evolution in GMC cores, we will investigate how the abundances of $N(\mathrm{N_2H^+})$, $N(\mathrm{H^{13}CO^+})$, and $N(\mathrm{c\text{-}C_3H_2})$ vary by star-forming activity or the kinetic temperature. We also use the abundances of $N(\mathrm{CCS})$, $N(\mathrm{HC_3N})$, and $N(\mathrm{NH_3})$ in the literature (Tatematsu et al., 2010, 2014a; Wilson et al., 1999). We adopted the rotation temperature $T_{\rm rot}$ from $\mathrm{NH_3}$ (1,1) and (2,2) data obtained by Wilson et al. (1999). Following relations derived by Danby et al. (1988); Tafalla et al. (2004), we can convert the rotation temperature to the kinetic temperature. We convolved the $\mathrm{N_2H^+}$ data with a Gaussian of FWHM 23.4" to smooth the cube to the 31.5" spatial resolution of the KVN 21 m telescope ($\sqrt{19.1^2 + 23.4^2} \sim 31.5$) and derived the column density of $\mathrm{N_2H^+}$.

2.4.1 $\mathrm{N_2H^+}$ vs c-$\mathrm{C_3H_2}$

Figure 2.10 shows the column density ratio $N(\mathrm{N_2H^+})/N(\mathrm{CCS})$ against $N(\mathrm{c\text{-}C_3H_2})/N(\mathrm{CCS})$. The critical densities of c-$\mathrm{C_3H_2}$ and $\mathrm{N_2H^+}$ are about 2×10^5 and 3×10^5 cm^{-3}, respectively, therefore we consider that they trace similar density ranges. The arrows of the figure 2.10 show the lower limit to the ratio: we estimated the upper limit of the CCS at 3σ. We regard the intensity peak as star forming if it is within 30" from protostars. The column densities are taken from Table 2.3. This figure indicates that CCS is abundant in starless regions, and $\mathrm{N_2H^+}$ and c-$\mathrm{C_3H_2}$ are abundant in star-forming regions, suggesting that CCS serves as young type molecule, while $\mathrm{N_2H^+}$ and c-$\mathrm{C_3H_2}$ serves as late type molecules in the Orion A cloud. Figure 2.11 shows the comparison of $N(\mathrm{c\text{-}C_3H_2})$ and $N(\mathrm{N_2H^+})$. This plot includes the positions where both c-$\mathrm{C_3H_2}$ and $\mathrm{N_2H^+}$ were detected and not listed in table 2.3. White diamonds represent the positions where the core temperature is $\geq$ 24 K, and black diamonds represent the positions where the core temperature is $<$ 24 K. The straight line represents the least-squares fit to the data. The correlation coefficient is $R = 0.7$, indicating a good correlation between $N(\mathrm{c\text{-}C_3H_2})$ and $N(\mathrm{N_2H^+})$. We found that some white diamonds are located below the best fit and this trend may be caused by $\mathrm{N_2H^+}$ disruption by CO evaporation. It is possible that c-$\mathrm{C_3H_2}$ is a one of late type molecules and can remain in warm cores where $\mathrm{N_2H^+}$ is destroyed by CO evaporation even though c-$\mathrm{C_3H_2}$ is one of the carbon-chain molecules. However, our result is based on a small sample; in particular, it contains

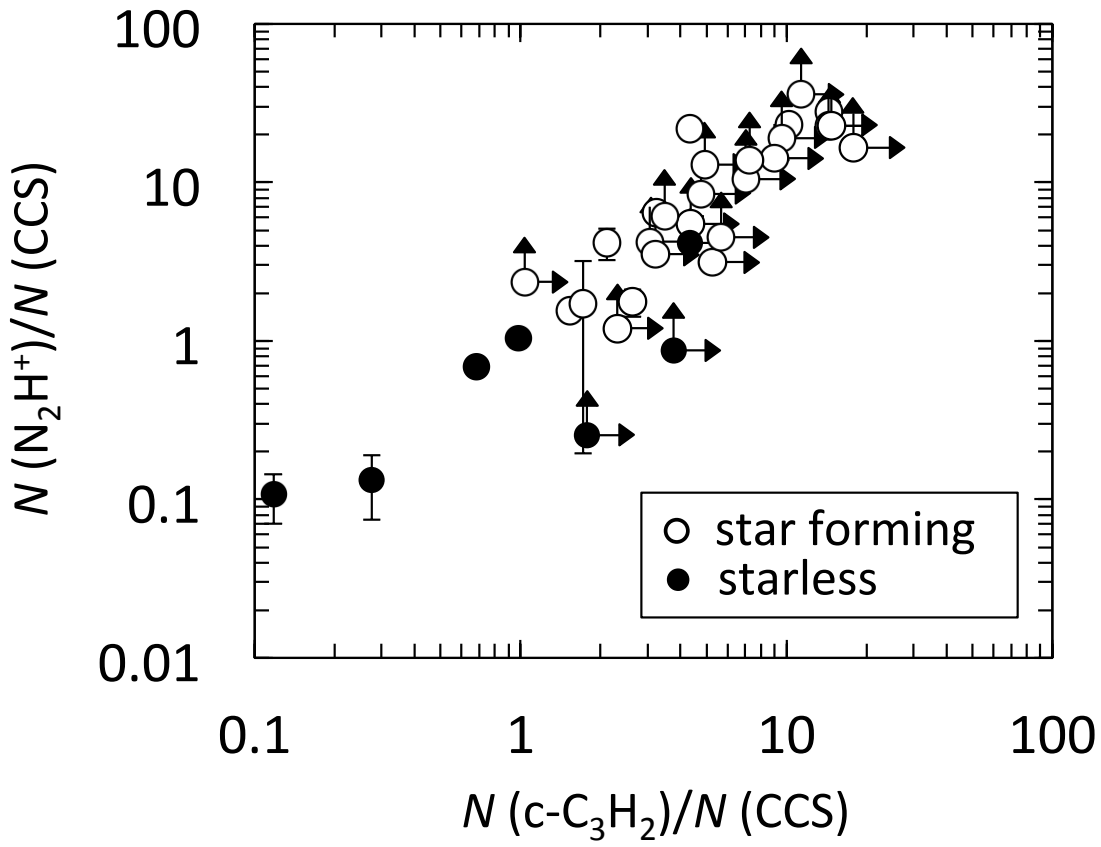

Figure 2.10: The column density ratio of N_2H^+ to CCS is plotted against the column density ratio of c-C_3H2 to CCS. CCS is abundant in starless cores while, c-C_3H_2 and N_2H^+ are abundant in star-forming cores. This suggests that CCS is a young-type tracer, but c-C_3H_2 and N_2H^+ are late-type tracers.

only one starless core. We need more observational data to confirm whether c-C_3H_2 is a late-type chemical tracer and can remain in warm regions.

2.4.2 N_2H^+ vs HCO^+, $H^{13}CO^+$

In warm region ($T_{\rm dust} > 25$ K), CO is in gas phase by evaporating from dust and N_2H^+ will be destroyed by the following reaction (Lee et al., 2004)

$$N_2H^+ + CO \longrightarrow HCO^+ + N_2. \tag{2.1}$$

By producing this reaction, we expect that HCO^+ is more abundant than N_2H^+ in warm regions. Sanhueza et al. (2012) suggested that the $N(N_2H^+)/N(HCO^+)$ ratio serves as a chemical clock

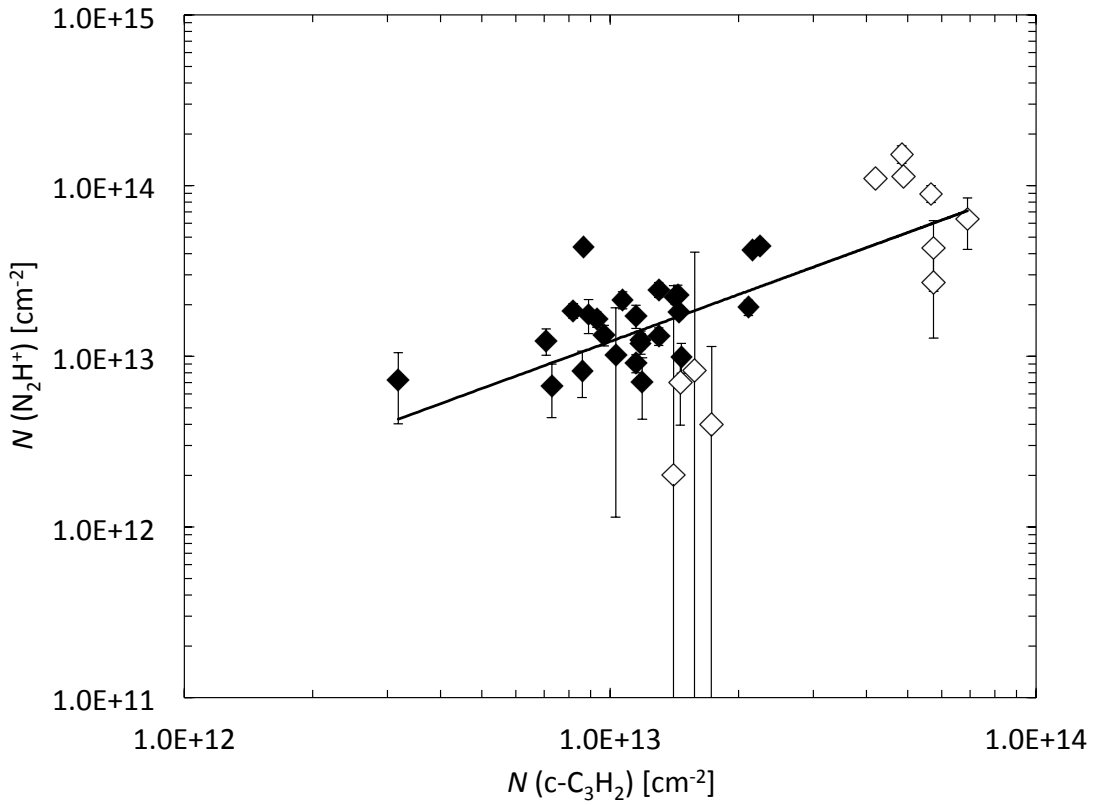

Figure 2.11: The column density of N_2H^+ is plotted against the column density of c-C_3H_2. The error bars represent 1 σ error in the N_2H^+ hyperfine fitting.

because the temperature increase causes CO evaporation after protostars form. Shirley et al. (2013) also suggested that the $N(N_2H^+)/N(HCO^+)$ ratio indicates whether the cores reserve cold and dense gas on the basis of $J = 3 - 2$ observations. However, HCO^+ is easily saturated due to the optical thickness. Therefore, the isotopes are more reliable tracer to investigate abundances in high dense region. Actually, we find the optical depth of HCO^+ is much higher than 1 in all position (see also table 2.3). Figure 2.12 shows the column density of N_2H^+ against the column density of $H^{13}CO^+$. When the HCO^+ was not detected, we use arrows to show 3σ upper limit. In star-forming cores, the N_2H^+ and $H^{13}CO^+$ column densities are correlated with each other. In starless cores, we do not see such a correlation, and the N_2H^+ column density does not exceed $\sim 1.0\times10^{13}$ cm^{-2}. Figure 2.13 shows a histogram of number distributions of $N(N_2H^+)/N(H^{13}CO^+)$ ratio. The vertical dashed lines indicate the median values. From these figures, we find that the $H^{13}CO^+$ is abundant in cluster regions, while N_2H^+ is abundant in isolated regions. Our results suggest that the $N(N_2H^+)/N(HC^{13}O^+)$ ratio is affected by not only the chemical evolution but also by star-forming activity. This is may be affected by temperature because the cluster regions may be warmer than the isolated regions by heating of protostars. We cannot mention starless regions because the histogram of the starless regions includes the upper limit.

2.4.3 CCS, HC_3N vs NH_3

We reanalyzed the data of Tatematsu et al. (2010) to see the chemical evolution of the $N(NH_3)/N(CCS)$ and $N(NH_3)/N(HC_3N)$ ratios against protostar association and temperature, by using a new protostar catalog of Megeath et al. (2012). New analysis has shown the chemical evolution tendency more clearly than Tatematsu et al. (2010).

They carried out one-point observations using CCS ($J_N = 4_3 - 3_2$) and HC_3N ($J = 5 - 4$) at 45 GHz toward the Orion A GMC cores with the Nobeyama 45 m telescope. The spatial resolution is $\sim$ 39" at 43 GHz and the typical rms is $\sim$ 0.1 K for CCS and $\sim$ 0.15 K for HC_3N. Table 2.6 summarizes the core parameters: coordinate, radius, LTE mass, and column density in CCS, HC_3N, and NH_3 lines, and kinetic temperature. The radius and LTE mass are derived by CS (1−0) line observations of Tatematsu et al. (1993). The column density of NH_3 is obtained by Wilson et al. (1999). They observed NH_3 $(J, K = 1, 1)$ and $(J, K = 2, 2)$ emission with the 100 m telescope of the MPIfR. The spatial resolution is 43" at 23 GHz. We check the association

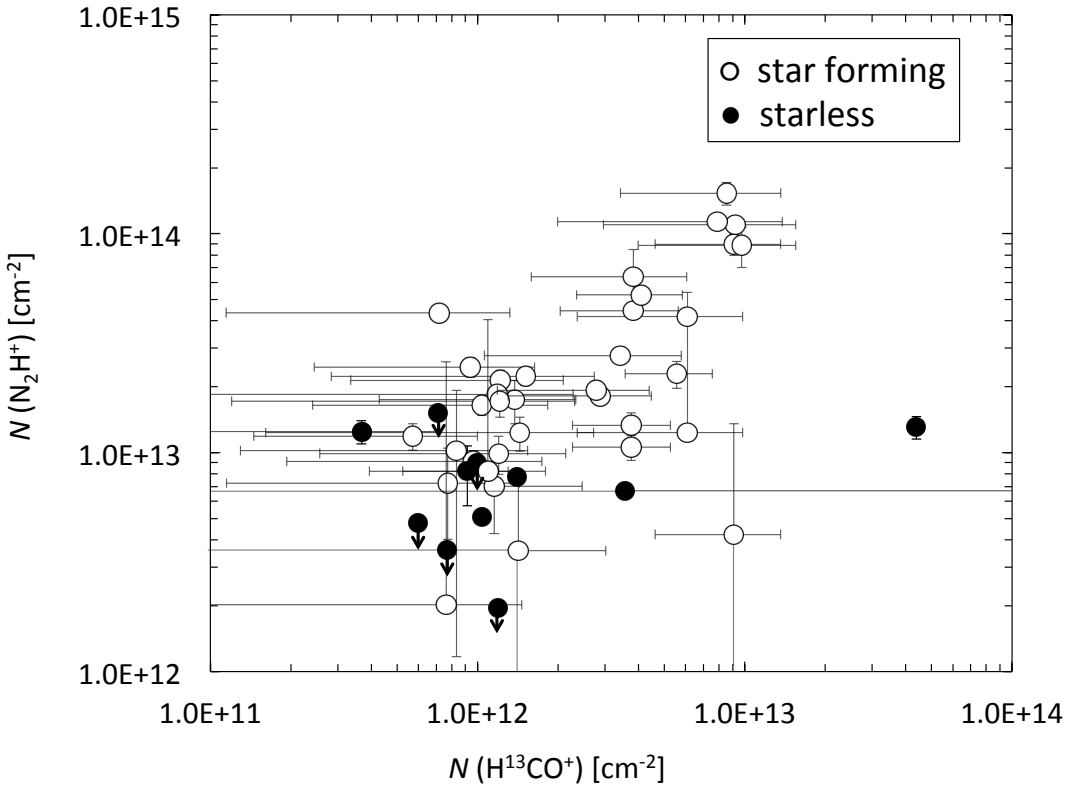

Figure 2.12: The column density of N_2H^+ is plotted against the column density of $H^{13}CO^+$. The error bars represent 1 σ error in the N_2H^+ hyperfine fitting or HCO^+ and $H^{13}CO^+$ Gaussian fitting.

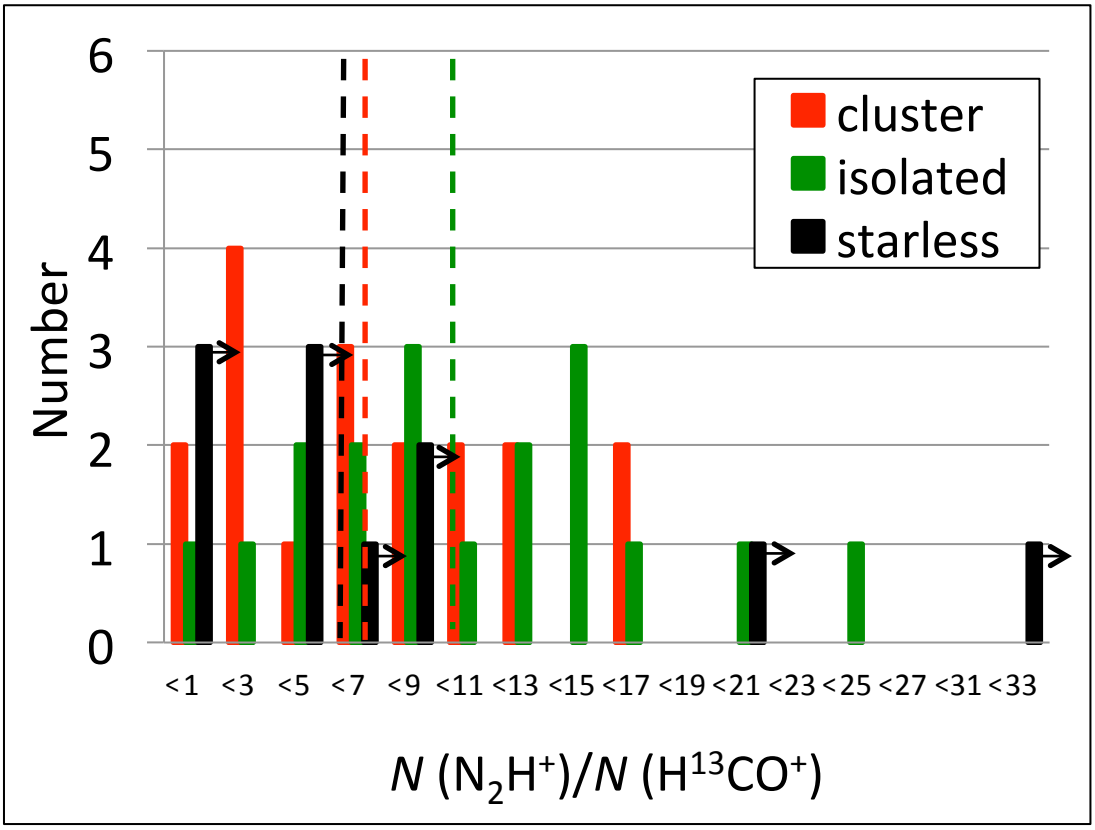

Figure 2.13: Histograms of the number distributions of the column density ratio of N_2H^+ to $H^{13}CO^+$ for each star-forming activities. The vertical dash lines represent the median values of the column density ratios for each stage. The right arrows represent upper limits. The median values suggest that the column density ratios increase from isolated to cluster.

of protostars with the criterion of 40", with respect to the core center. The criterion of 40" is the spatial resolution of the Nobeyama 45 m telescope at 45 GHz and the 100 m telescope of the MPIfR. If a protostar is located within 40" in two cores, we list the closer core.

Figure 2.14 plots the $N(NH_3)/N(CCS)$ ratio against temperature. Open circles represent star-forming cores and filled circles represent starless cores. The error bars represent the average noise level of NH_3 observations of $T_R = 0.4$ K, assuming that NH_3 emission is optically thin. This figure shows that the $N(NH_3)/N(CCS)$ ratio is low toward starless cores while it is high toward star-forming cores, regardless of temperature. This is similar to the tendency known in cold dark clouds, and the $N(NH_3)/N(CCS)$ ratio seems to reflect the chemical evolution even in the Orion A cloud. We see two star-forming cores (TUKH056 and 069) showing low ratios of $N(NH_3)/N(CCS)$.

Figures 2.15 and 2.16 show the $N(NH_3)/N(CCS)$ ratio against the line-width of CCS. We find that the $N(NH_3)/N(CCS)$ decreases with increasing linewidths. The two star-forming cores of TUKH056 and 069 have linewidhs of 2.0 and1.6 km s^{-1}, respectively. It is still not clear how CCS becomes abundant in star forming region with large turbulence. One possibility is that the one-point observations may have offset from the core center and traced outer region of the cores. Another possibility is that CCS may be produced by turbulent shocks (Yamaguchi et al., 2012).

In cold dark clouds, it is also suggested that the $N(NH_3)/N(HC_3N)$ ratio indicates the chemical evolution (Suzuki et al., 1992). Figure 2.17 shows the $N(NH_3)/N(HC_3N)$ ratio against the temperature. From this figure, we find that the $N(NH_3)/N(HC_3N)$ ratio takes high in star forming region, while it is low in starless region regardless of temperature. We also find a tendency for the $N(NH_3)/N(HC_3N)$ ratio to decrease with increasing temperature. Figures 2.18 and 2.19 show the $N(NH_3)/N(HC_3N)$ ratio against the line-width of HC_3N. These figures suggest that these column density ratios decrease in active or turbulent cores. The HC_3N may be also produced by shocks. However, if we take a value of temperature or linewidth, these column density ratios can divide the dense cores into star-forming and starless cores.

Our new analysis suggest that $N(NH_3)/N(HC_3N)$ and $N(NH_3)/N(CCS)$ may be indicators of the chemical evolution but we should be careful about the turbulent motions and temperature. However, the column densities of CCS and HC_3N are calculated using the data in a single line. To constrain the excitation condition, it is desirable to make multi-transition observations.

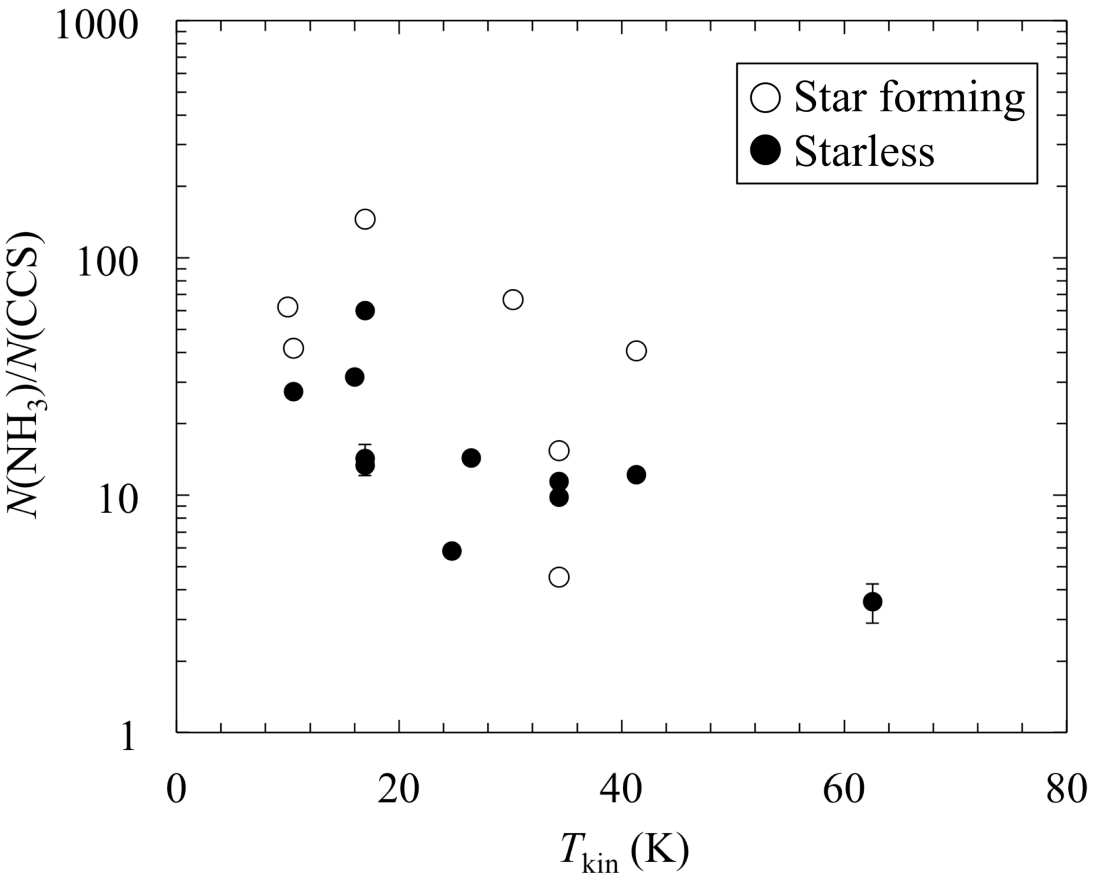

Figure 2.14: The column density ratio of NH_3 to CCS is plotted against the kinetic temperature. The open circles represent star-forming cores and filled circles represent starless cores.

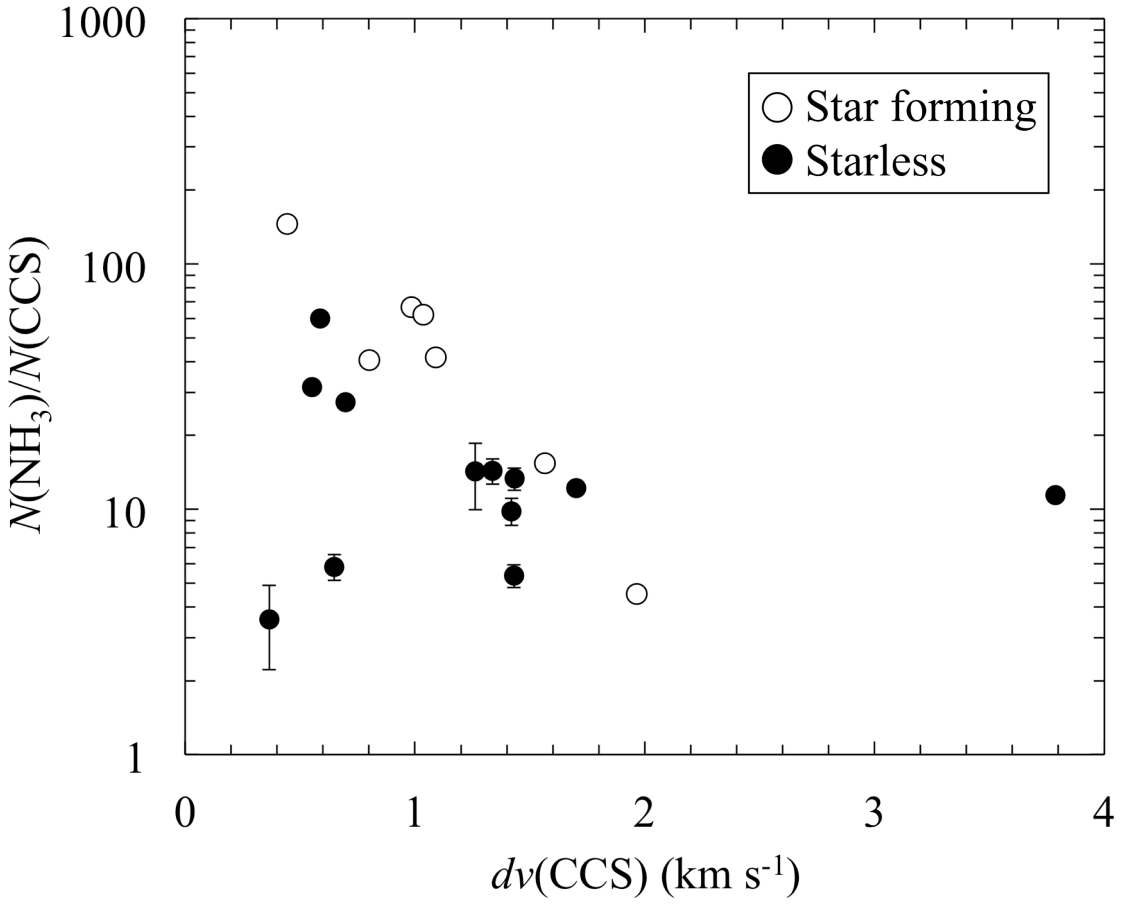

Figure 2.15: The column density ratio of NH_3 to CCS is plotted against the line-width of CCS. The open circles represent star-forming cores and filled circles represent starless cores.

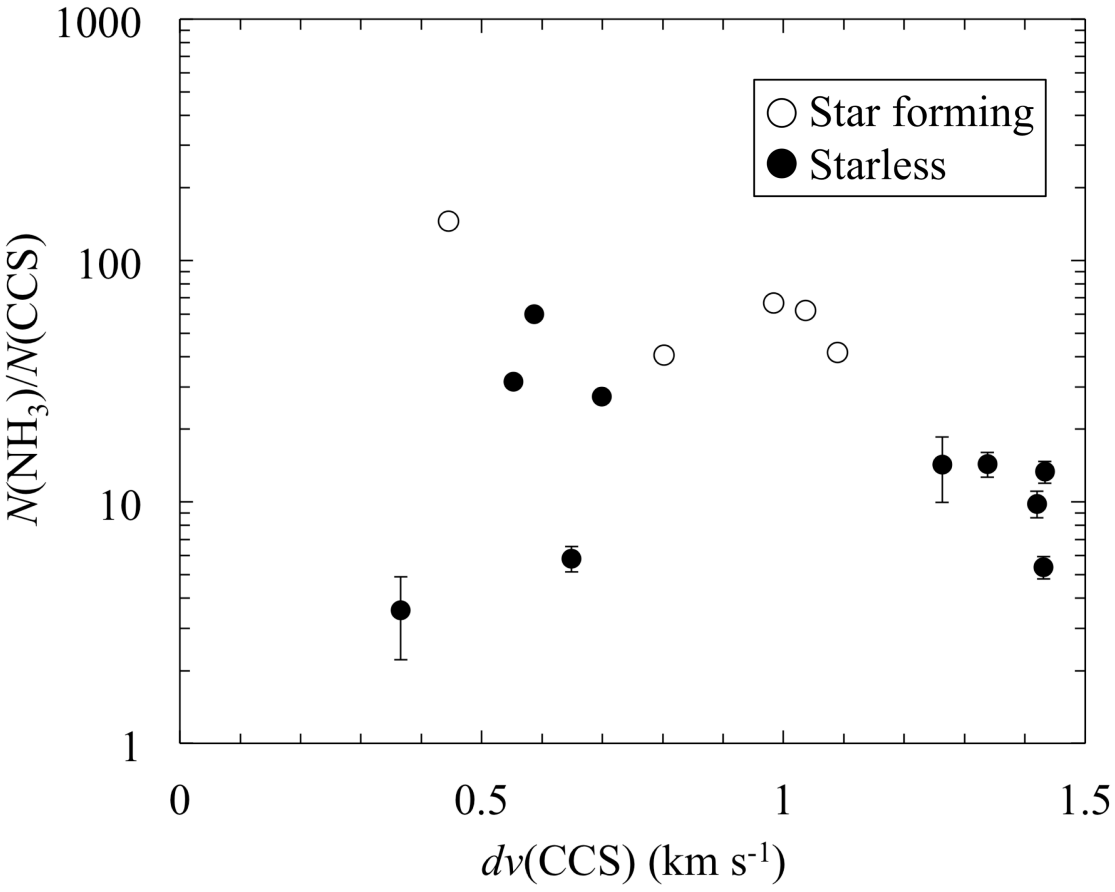

Figure 2.16: Same as figure 2.15 but a line-width of $0 - 2$ km s^{-1}.

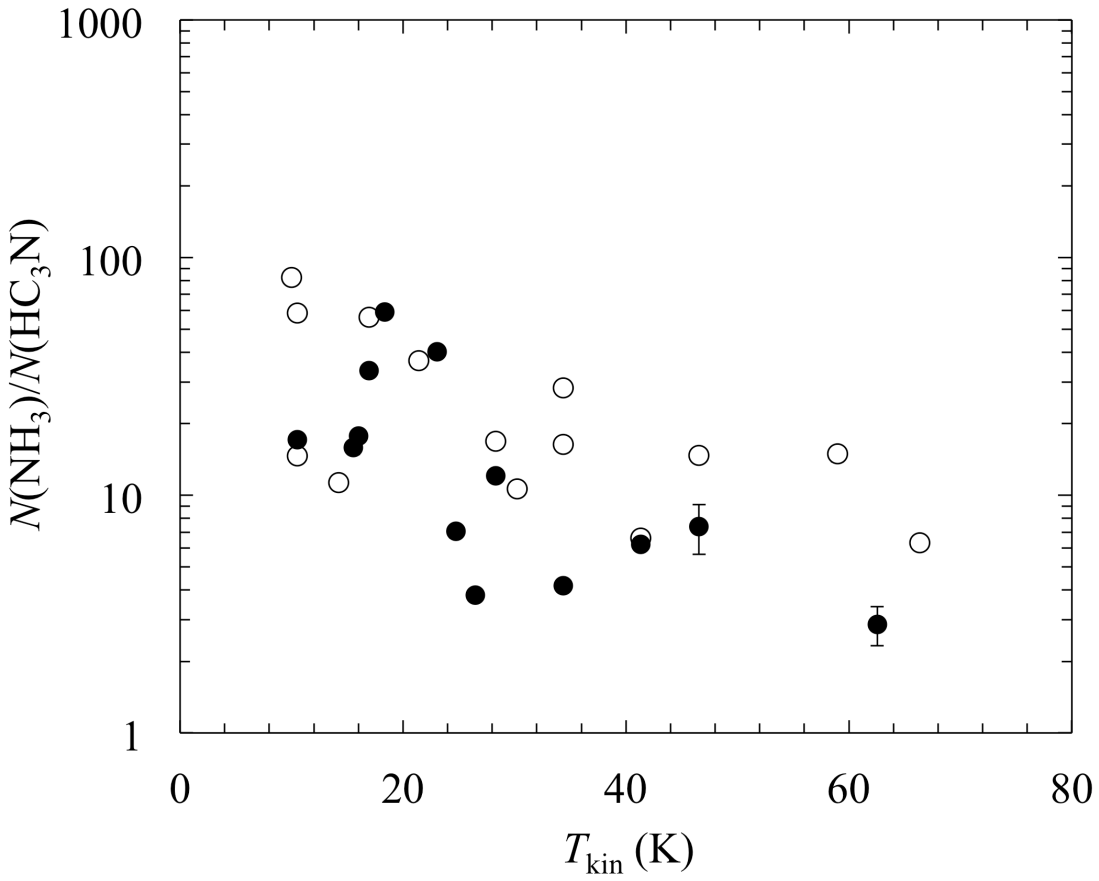

Figure 2.17: The column density ratio of NH_3 to HC_3N is plotted against the kinetic temperature. The open circles represent star-forming cores and filled circles represent starless cores.

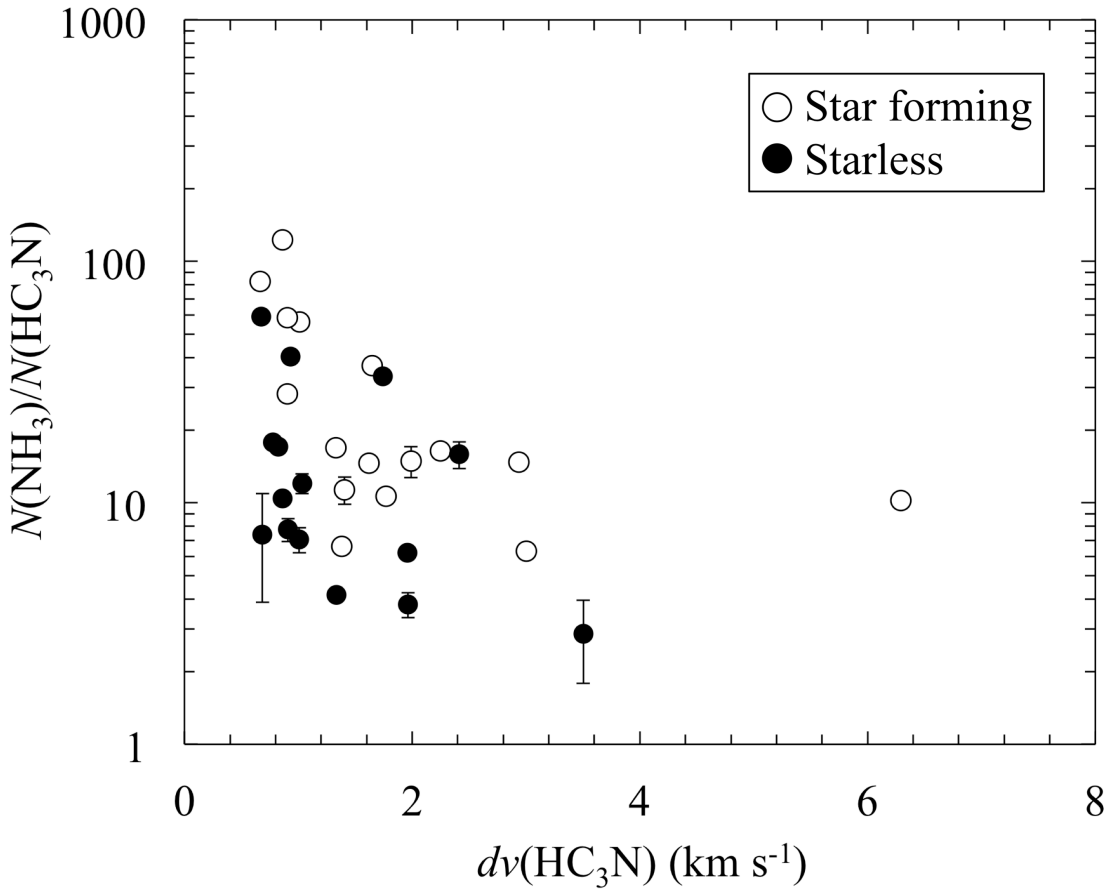

Figure 2.18: The column density ratio of NH_3 to HC_3N is plotted against the line-width of HC_3N. The open circles represent star-forming cores and filled circles represent starless cores.

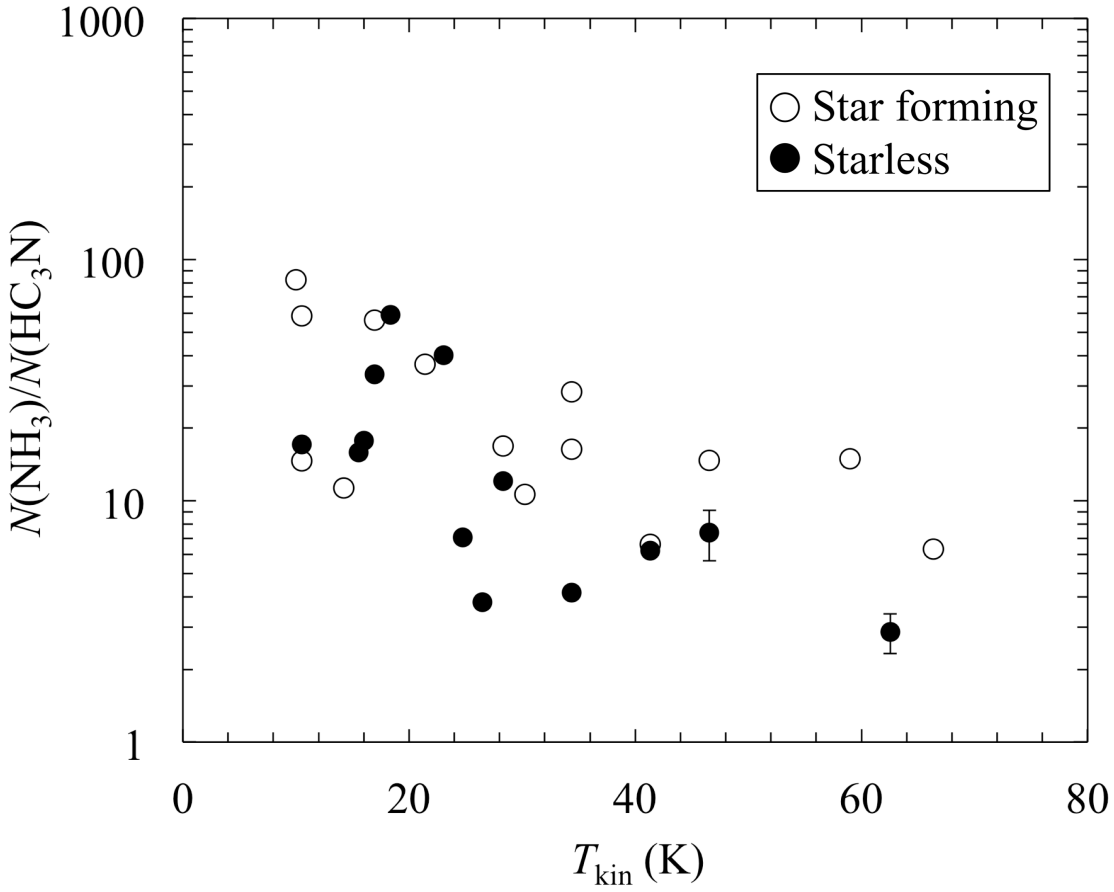

Figure 2.19: Same as figure 2.18 but a line-width of $0 - 2$ km s^{-1}.

2.5 Gravitational instability of the N_2H^+ cores

To understand what initiates star formation, we investigate the difference of the properties between cores with protostars/YSOs and those without protostars/YSOs. We analyze the core stability following Nakano (1998). Neglecting the effect of magnetic field and assuming spherical uniform cores, the virial equation reduces to

$$\frac{1}{2}\frac{d^2I}{dt^2} = 3C_{\rm eff}^2 M_{\rm core} - \frac{3}{5}\frac{GM_{\rm core}^2}{R} - 4\pi R^3 P_{\rm s} \equiv F(R) \tag{2.2}$$

$$\frac{P_{\rm s}}{k_B} \approx \frac{G\Sigma_0^2}{k_B} \tag{2.3}$$

where $C_{\rm eff}$, $M_{\rm core}$, R and I are the effective sound speed, the mass, radius, and generalized moment of inertia, respectively, of the core. The effective sound speed including turbulence (non-thermal component contribution) as well as thermal contribution, is defined as follows:

$$C_{\rm eff} = \left(\frac{\Delta V_{\rm tot}^2}{8\ln 2}\right)^{1/2} \tag{2.4}$$

$$\Delta V_{\rm tot} = \left[\Delta V_{\rm obs}^2 + 8\ln 2 kT\left(\frac{1}{m} - \frac{1}{m_{\rm obs}}\right)\right]^{1/2} \tag{2.5}$$

where m, $m_{\rm obs}$, and $T_{\rm k}$ are the mean molecular weight (2.33 amu), the mass of the observed molecule, and the kinetic temperature of the gas, respectively. $P_{\rm s}$ and Σ_0 are the pressure and the column density of the surrounding medium, respectively. We derive the $P_{\rm s}$ from the ^{13}CO column densities (Nagahama et al. (1998)) in which cores are embedded. The core is in equilibrium when $F(R) = 0$. Nakano's (1998) equation (27) gives

$$P_{\rm cr} = \frac{1}{12\pi G^3 M_{\rm core}^2}\left(\frac{5}{3}\right)^3\left(\frac{9}{4}C_{\rm eff}^2\right)^4 \tag{2.6}$$

$P_{\rm cr}$ is a critical value for the pressure of the surrounding medium $P_{\rm s}$, above which no equilibrium states exit. At this critical state $P_{\rm s}$ = $P_{\rm cr}$, the core has an equilibrium state with radius

$$R_{\rm cr} = \frac{4GM_{\rm core}}{15\pi C_{\rm eff}^2} \tag{2.7}$$

Figure 2.20 plots the virial theorem function $F(R)$ against $R/R_{\rm cr}$ for the N_2H^+ cores. Nakano (1998) assumed that the core is initially in a stable equilibrium state ($F = 0$ and $R/R_{\rm cr} > 1$). By dissipating turbulence, $R/R_{\rm cr}$ decreases until the core reaches the critical point (F = 0 and $R/R_{\rm cr}$ = 1). After the core goes beyond the critical point, the core becomes unstable. As a result, perturbations trigger the core collapse because no equilibrium states exist, and finally stars form. The result shown in Figure 2.20 seems to be consistent with the scenario; the cores without protostars are in the stable equilibrium ($F = 0$ and $R/R_{\rm cr} > 1$), while the cores with protostars are in the unstable state ($F < 0$). Some cores with protostars are located in the stable equilibrium. This may be caused by the N_2H^+ destruction. The mass traced by N_2H^+ will be underestimated in warm region and $R_{\rm cr}$ might be underestimated. Correction for this will make $R/R_{\rm cr}$ larger.

Figure 2.21 is the same as figure 2.20 but shows only the cores with gas temperature < 25 K. This figure shows the tendency more clearly. However, we found that some starless cores are located in unstable or virial non-equilibrium states. We point out two possibilities; we did not resolve structure in these cores well or these cores may be on the verge of star formation. One starless core stands out with a low $F(R)$. This core was identified No. 32 by Tatematsu et al. (2008). They derived the core size (R) and the mass ($M_\odot$) to be 0.17 pc and 78.0 $M_\odot$, respectively using N_2H^+. Because of its large core size, it might be suggested that the core is unstable on the large scale ($\sim$ 0.1 pc) but it is stable on the clump small scale ($\leq$ 0.04 pc).

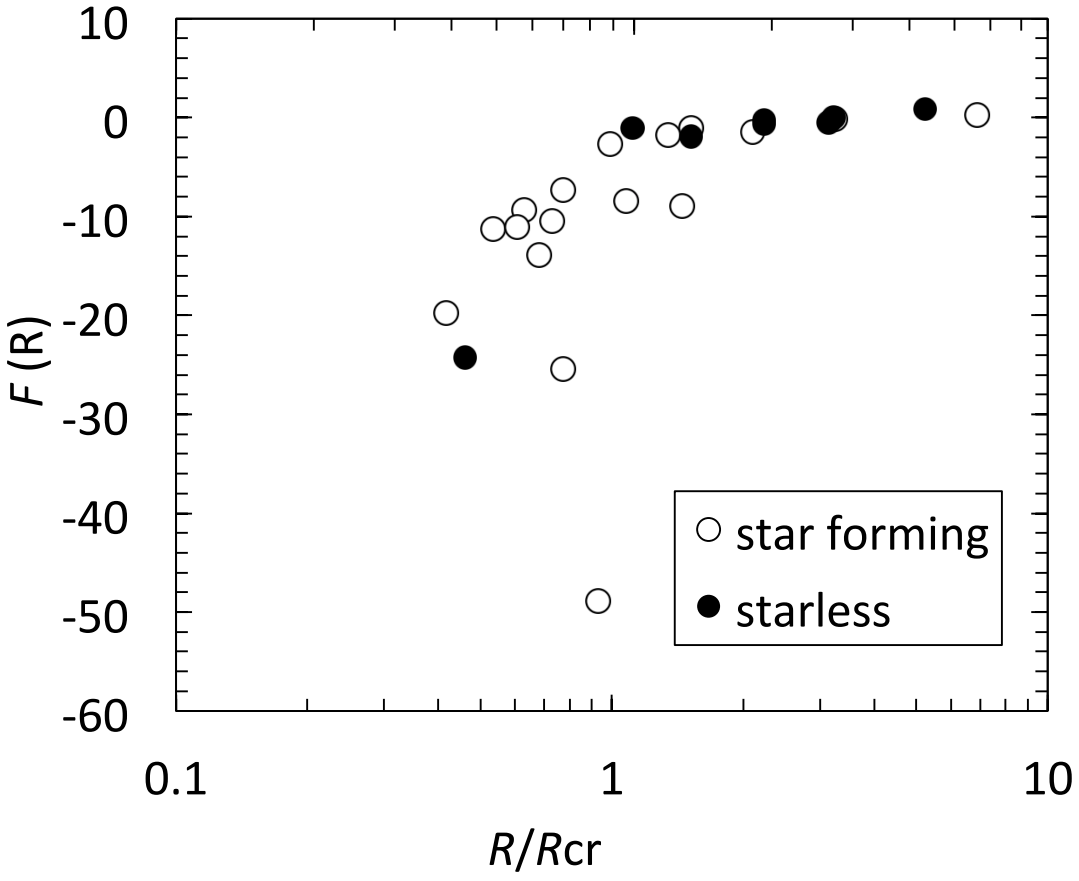

Figure 2.20: Virial theorem function F (eq[2.2]) is plotted against the radius R divided by $R_{\rm cr}$ (eq.[2.7]) for the N_2H^+ cores

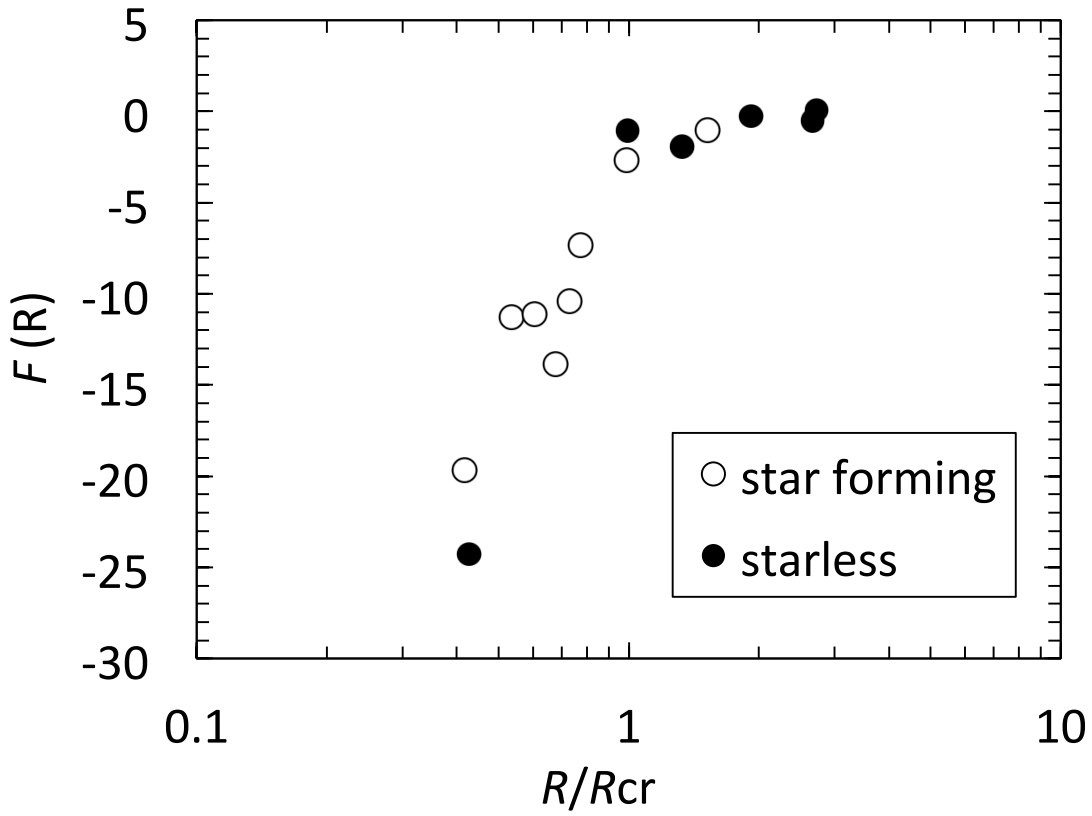

Figure 2.21: Virial theorem function F (eq[2.2]) is plotted against the radius R divided by $R_{\rm cr}$ (eq.[2.7]) for the N_2H^+ cores where the kinetic temperature is less than 25 K.

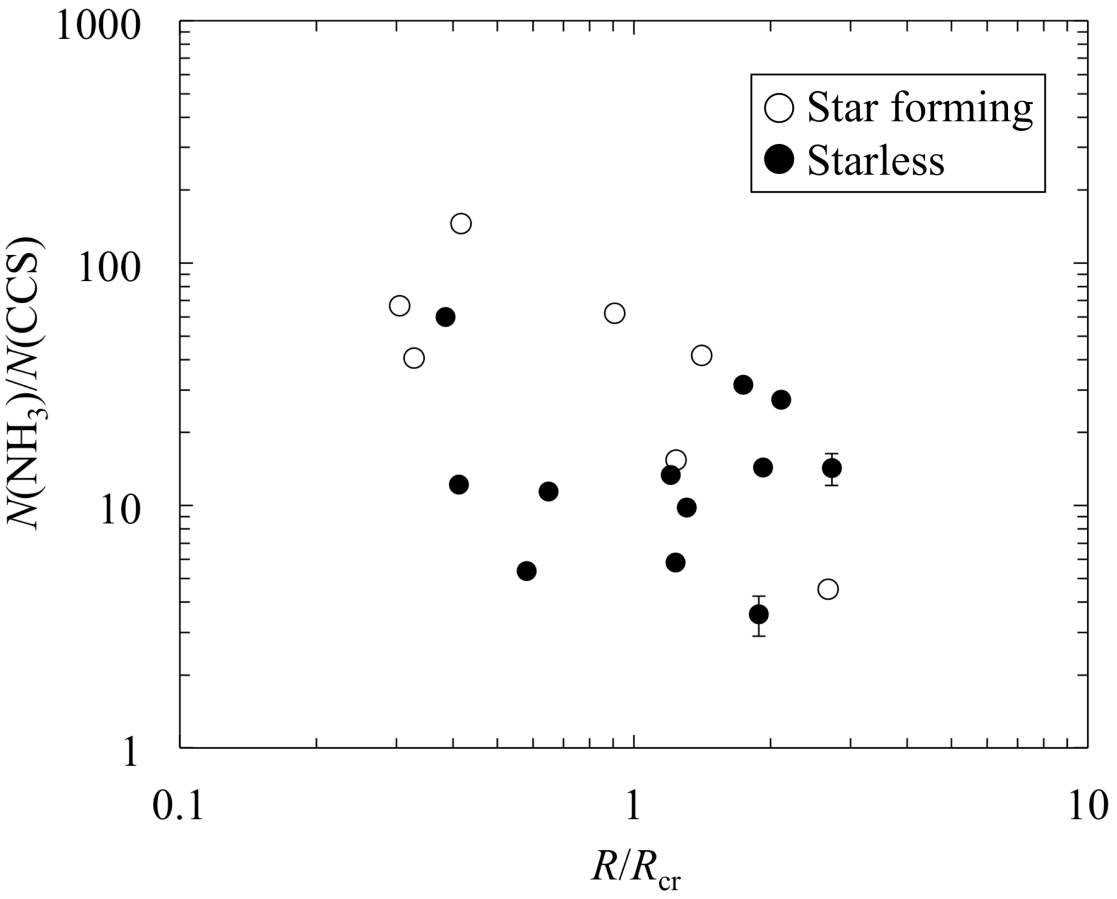

Figure 2.22: The column density ratio of NH_3 to CCS is plotted against the radius R divided by R_{cr} (eq.[2.7]) for the CS cores

Finally, figure 2.22 shows the $N(NH_3)/N(CCS)$ ratio against R/R_{cr}. R and R_{cr} are derived from the CS (1−0) data obtained by Tatematsu et al. (1993). We found that the $N(NH_3)/N(CCS)$ ratio decreases with R/R_{cr}. The correlation coefficient is $R = -0.5$, indicating a moderate negative correlation. The star-forming cores seems to be located in high $N(NH_3)/N(CCS)$ and low R/R_{cr} regions. On the other hand, the starless cores seem to be located in low $N(NH_3)/N(CCS)$ and in high R/R_{cr} regions. This may suggest that the chemical evolution can be an indicator of the dynamical evolution of the core. If we derive R/R_{cr} by using a high-density tracer like N_2H^+, the separation might be better.

Table 2.4: Coordinate, Radius, Mass, Column Density from CS, CCS, HC_3N, and NH_3 Line Parameter

			CS[1]		CCS[2]	HC_3N[2]	NH_3[3]		Megeath
TUKH[1]	R.A. (J2000) h m s	Decl. (J2000) ° ′ ″	R (pc)	$M_{\rm LTE}$ ($M_\odot$)	N(CCS) (10^{12} cm^{-2})	N(HC_3N) (10^{12} cm^{-2})	N(NH_3) (10^{13} cm^{-2})	$T_{\rm kin}$ (K)	
1	5:35:20.40	-4:57:10.0	0.15	93	···	···	3.6	21	
2	5:35:31.00	-4:59:11.0	0.14	140	···	···	10.8	30	2469
3	5:35:17.70	-5:00:30.0	0.23	910	2.68	6.94	39	17	2446
4	5:35:28.30	-5:01:11.0	0.22	290	···	···	10.2	23	
5	5:35:28.30	-5:03:11.0	0.14	120	···	···	4.1	25	2408
6	5:35:17.50	-5:04:30.0	0.2	580	···	···	9.3	28	2385
7	5:35:38.90	-5:05:51.0	0.2	170	···	···	3.6	34	
8	5:35:22.80	-5:07:50.0	0.2	310	···	···	22	26	
9	5:35:12.10	-5:09:49.0	0.17	110	···	···	3.2	17	
10	5:35:38.80	-5:09:51.0	0.11	18	···	···	2.8	30	
11	5:35:25.40	-5:10:30.0	0.18	240	···	19.41	32.8	28	2279
12	5:35:04.00	-5:11:09.0	0.13	23	···	···	1.7	25	
13	5:35:30.80	-5:11:51.0	0.16	84	···	4.81	5.8	28	
14	5:35:01.30	-5:12:29.0	0.14	69	···	···	~ 2	17	
15	5:35:17.40	-5:12:30.0	0.15	87	···	4.05	16.3	23	
16	5:35:17.30	-5:14:30.0	0.11	79	···	···	8.9	20	
17	5:35:06.60	-5:15:09.0	0.26	470	···	···	1.2	17	
18	5:35:17.30	-5:15:50.0	0.16	90	···	···	8.8	26	2187
19	5:35:09.20	-5:17:49.0	0.14	92	···	···	6.9	25	
20	5:35:03.80	-5:19:09.0	0.11	27	···	···	~ 2		
21	5:35:17.20	-5:19:10.0	0.11	530	8.74	54.86	58.4	30	2069
22	5:35:01.10	-5:19:49.0	0.12	49	···	···	3.2	47	
23	5:35:41.30	-5:19:52.0	0.12	45	···	···	3	17	
24	5:35:54.70	-5:19:53.0	0.1	19	···	···	1.1	47	2047
25	5:35:25.20	-5:20:30.0	0.09	22	···	2.84	2.1	47	
26	5:35:17.20	-5:21:10.0	0.11	360	8.96	55	36.3	41	1971
27	5:35:46.60	-5:21:12.0	0.08	19	···	···	~ 2	166	
28	5:34:58.40	-5:21:48.0	0.14	260	···	···	6.6	21	
29	5:35:14.50	-5:22:30.0	0.15	1800	···	244.04	> 250	166	1913
30	5:35:01.10	-5:23:49.0	0.17	180	···	···	4.7	34	1800
31	5:35:14.50	-5:23:50.0	0.1	320	···	57.24	36.2	66	1807
32	5:35:30.60	-5:23:51.0	0.08	11	···	8.45	···		
33	5:35:03.70	-5:24:29.0	0.08	51	6.41	24.24	9.2	26	1800
34	5:35:25.10	-5:24:30.0	0.06	38	···	···	4.8	116	
35	5:35:06.40	-5:25:49.0	0.12	61	···	···	~ 4	116	
36	5:35:17.10	-5:25:50.0	0.07	77	···	9.72	14.5	59	1718

[1]Tatematsu et al. (1993)
[2]Tatematsu et al. (2010)
[3]Wilson et al. (1999)
[1]Tatematsu et al. (1993)
[2]Tatematsu et al. (2010)
[3]Wilson et al. (1999)

Table 2.5: Coordinate, Radius, Mass, Column Density from CS, CCS, HC_3N, and NH_3 Line Parameter

			CS[1]		CCS[2]	HC_3N[2]	NH_3[3]		Megeath
TUKH[1]	R.A. (J2000) h m s	Decl. (J2000) ° ′ ″	R (pc)	$M_{\rm LTE}$ ($M_\odot$)	N(CCS) (10^{12} cm^{-2})	N(HC_3N) (10^{12} cm^{-2})	N(NH_3) (10^{13} cm^{-2})	$T_{\rm kin}$ (K)	
37	5:35:14.40	-5:26:30.0	0.1	600	16.11	31.75	19.7	41	
38	5:35:01.00	-5:27:49.0	0.13	44	···	···	···		
39	5:35:11.70	-5:27:49.0	0.11	120	15.74	43.23	~ 18	34	
40	5:35:11.70	-5:29:09.0	0.1	110	14.9	10.31	~ 8		
41	5:35:06.30	-5:29:49.0	0.1	27	···	···	< 4		
42	5:35:17.00	-5:30:30.0	0.09	37	···	···	< 3		
43	5:35:03.60	-5:31:49.0	0.16	75	···	···	3.6	34	
44	5:35:03.60	-5:34:29.0	0.13	110	···	···	8.3	34	
45	5:35:16.90	-5:35:10.0	0.13	41	···	···	···		
46	5:34:58.10	-5:35:48.0	0.23	350	···	···	< 6	25	
47	5:35:06.20	-5:36:29.0	0.29	390	3.07	5.5	18.4	17	1400
48	5:35:08.80	-5:37:49.0	0.18	220	···	···	~ 9		
49	5:34:50.10	-5:39:08.0	0.14	75	8.28	···	11.8	17	1350
50	5:34:36.60	-5:41:47.0	0.14	41	···	···	~ 6		
51	5:34:55.30	-5:43:08.0	0.27	240	···	···	11.4	25	
52	5:34:52.60	-5:45:48.0	0.22	150	···	···	13.6	25	
53	5:35:00.60	-5:48:29.0	0.21	69	···	···	8.4	23	1191
54	5:35:08.50	-5:53:09.0	0.15	19	···	···	10.2	17	
55	5:34:57.80	-5:53:48.0	0.19	100	···	···	6.7	17	1121, 1127
56	5:35:11.10	-5:55:49.0	0.15	55	17.52	2.79	7.9	34	
57	5:35:03.10	-5:57:49.0	0.27	250	8.7	···	11.6	17	
58	5:35:11.10	-5:59:49.0	0.24	160	···	···	8.2	34	
59	5:35:40.40	-6:07:52.0	0.33	380	12.31	···	12.1	34	
60	5:35:40.40	-6:09:12.0	0.24	150	···	···	13.3	34	
61	5:36:07.10	-6:10:34.0	0.2	150	···	···	7.1	34	
62	5:36:04.40	-6:12:33.0	0.3	310	···	···	5	25	
63	5:36:36.70	-6:13:16.0	0.27	360	···	···	3.3	25	
64	5:36:28.50	-6:15:15.0	0.21	170	···	···	10	21	
65	5:36:36.70	-6:15:16.0	0.2	34	···	1.9	11.2	18	
66	5:36:41.90	-6:17:16.0	0.3	280	···	···	4.6	17	
67	5:36:20.40	-6:21:54.0	0.22	330	···	13.59	20	47	944
68	5:35:56.20	-6:22:33.0	0.13	33	···	···	3.5	23	
69	5:36:25.80	-6:23:15.0	0.15	190	11.32	10.61	17.4	34	933
70	5:36:44.50	-6:24:36.0	0.17	64	···	···	~ 5	18	
71	5:35:29.30	-6:26:31.0	0.15	120	···	···	5.5	17	882
72	5:35:53.50	-6:26:33.0	0.27	310	···	···	5.5	17	
73	5:36:33.70	-6:26:35.0	0.17	120	···	···	17.3	34	
74	5:36:41.80	-6:26:36.0	0.19	140	···	···	25.1	17	
75	5:36:41.80	-6:27:56.0	0.14	41	···	···	5.6	11	
76	5:36:01.50	-6:28:33.0	0.12	30	···	···	4.2	84	
77	5:36:47.10	-6:28:36.0	0.18	140	···	···	~ 6	25	
78	5:36:49.80	-6:29:17.0	0.12	34	···	···	~ 5	25	
79	5:36:04.20	-6:29:53.0	0.14	28	···	···	~ 5	63	
80	5:35:26.60	-6:30:31.0	0.11	37	···	···	~ 2	34	
81	5:36:25.50	-6:30:35.0	0.15	56	···	···	~ 2	25	
82	5:36:17.50	-6:31:14.0	0.14	84	···	···	~ 4	34	
83	5:36:47.00	-6:31:56.0	0.2	59	6.75	8.37	2.4	63	
84	5:35:58.70	-6:32:33.0	0.12	55	···	···	6.2	63	
85	5:36:20.20	-6:33:14.0	0.28	39	···	···	2		
86	5:36:57.80	-6:33:57.0	0.18	34	···	···	···		

Table 2.6: Coordinate, Radius, Mass, Column Density from CS, CCS, HC_3N, and NH_3 Line Parameter

			CS[1]		CCS[2]	HC_3N[2]	NH_3[3]		Megeath
TUKH[1]	R.A. (J2000) h m s	Decl. (J2000) ° ′ ″	R (pc)	$M_{\rm LTE}$ ($M_\odot$)	N(CCS) (10^{12} cm^{-2})	N(HC_3N) (10^{12} cm^{-2})	N(NH_3) (10^{13} cm^{-2})	$T_{\rm kin}$ (K)	
87	5:36:44.40	-6:34:36.0	0.18	54	···	···	3	25	
88	5:37:00.40	-6:35:57.0	0.19	170	6.86	5.68	4	25	
89	5:36:33.50	-6:38:35.0	0.16	62	···	···	12.4	11	821
90	5:36:17.30	-6:39:54.0	0.17	61	···	···	3		
91	5:36:25.40	-6:45:15.0	0.2	310	···	4.59	5.2	14	783
92	5:36:25.20	-6:45:55.0	0.15	120	···	4.28	15.8	21	772
93	5:36:14.60	-6:48:34.0	0.23	310	···	5.04	~ 8	16	
94	5:36:27.70	-6:51:15.0	0.14	30	···	···	2.2	25	
95	5:38:46.90	-7:00:45.0	0.16	85	···	4.79	~ 7	11	697
96	5:38:04.50	-7:06:02.0	0.1	19	···	···	~ 10	34	
97	5:37:59.00	-7:07:22.0	0.19	150	7.92	5.65	~ 33	11	638
98	5:38:07.10	-7:08:42.0	0.15	60	···	···	~ 4.8	11	636
99	5:38:28.60	-7:10:04.0	0.2	89	···	···	~ 4	25	
100	5:38:12.50	-7:10:43.0	0.1	23	···	···	~ 5	17	
101	5:39:03.50	-7:11:26.0	0.15	27	···	···	5.3	17	
102	5:38:33.20	-7:12:04.0	0.1	8.2	···	···	~ 3	47	
103	5:38:51.90	-7:12:05.0	0.2	100	···	···	~ 15	11	
104	5:39:06.20	-7:12:07.0	0.19	28	3.88	6.2	10.6	11	
105	5:38:07.00	-7:13:22.0	0.18	57	5.81	1.85	···		
106	5:38:20.50	-7:13:23.0	0.15	29	···	···	···		
107	5:38:09.70	-7:15:22.0	0.18	71	···	···	···		
108	5:38:15.00	-7:16:43.0	0.15	37	···	···	···		
109	5:38:28.50	-7:16:44.0	0.19	52	···	···	···		
110	5:39:22.20	-7:18:48.0	0.14	12	···	···	···		
111	5:39:00.80	-7:20:06.0	0.15	39	···	···	5.1	25	595
112	5:38:35.80	-7:20:44.0	0.19	100	···	···	~ 6		
113	5:39:29.20	-7:24:08.0	0.12	16	···	···	7		
114	5:38:49.10	-7:24:45.0	0.26	160	···	···	~ 4		
115	5:38:54.40	-7:26:06.0	0.1	14	···	···	~ 44	11	
116	5:38:35.60	-7:26:44.0	0.22	160	···	···	···		
117	5:39:18.40	-7:26:47.0	0.27	320	3.54	2.67	~ 22	10	545
118	5:40:28.10	-7:27:32.0	0.12	25	···	···	···		536
119	5:40:28.10	-7:28:52.0	0.14	30	···	···	···		
120	5:38:25.70	-7:29:24.0	0.15	34	···	···	···		
121	5:38:31.00	-7:30:04.0	0.13	17	···	···	···		
122	5:39:42.50	-7:30:09.0	0.18	49	7.3	12.95	~ 23	16	
123	5:39:58.60	-7:30:50.0	0.23	78	···	3.75	~ 46		514
124	5:40:28.10	-7:30:52.0	0.14	22	···	···	~ 6		
125	5:40:14.60	-7:32:52.0	0.18	35	···	4.78	~ 5		

Chapter 3

Chemical evolutions of dense cores in the Vela C giant molecular cloud complex

A part of this chapter has been published as Ohashi, Satoshi; Tatematsu, Ken'ichi; Fujii, Kosuke; Sanhueza, Patricio; Nguyen Luong, Quang; Choi, Minho; Hirota, Tomoya; & Mizuno, Norikazu, PASJ, 68, 3 (Ohashi et al., 2016b)

Abstract

We have observed the HC_3N ($J = 10 - 9$) and N_2H^+ ($J = 1 - 0$) lines toward the Vela C molecular clouds with the Mopra 22 m telescope to study chemical characteristics of dense cores. The intensity distributions of these molecules are similar to each other at an angular resolution of 53", corresponding to 0.19 pc suggesting that these molecules trace the same dense cores. We identified 25 local peaks in the velocity-integrated intensity maps of the HC_3N and/or N_2H^+ emission. Assuming LTE conditions, we calculated the column densities of these molecules and found a tendency that N_2H^+/HC_3N abundance ratio seems to be low in starless regions while it seems to be high in star-forming regions, similar to the tendencies in the NH_3/CCS, NH_3/HC_3N, and N_2H^+/CCS abundance ratios found in previous studies of dark clouds and the Orion A GMC. We suggest that carbon chain molecules, including HC_3N, may trace chemically young molecular gas and N-bearing molecules, such as N_2H^+, may trace later stages of chemical evolution in the Vela C molecular clouds. It may be possible that the N_2H^+/HC_3N abundance ratio of ~ 1.4 divides the star-forming and starless peaks in the Vela C, although it is not as clear as those in NH_3/CCS, NH_3/HC_3N, and N_2H^+/CCS for the Orion A GMC. This less clear separation may be caused by our lower spatial resolution or the misclassification of star-forming and starless peaks due to the larger distance of the Vela C. It might be also possible that the HC_3N ($J = 10 - 9$) transition is not a good chemical evolution tracer compared with CCS ($J = 4 - 3$ and $7 - 6$) transitions.

3.1 Introduction of this chapter

In previous section, we found that $N(N_2H^+)/N(CCS)$, $N(c\text{-}C_3H_2)/N(CCS)$, $N(NH_3)/N(CCS)$ and $N(NH_3)/N(HC_3N)$ are high in star-forming regions and low in starless regions in the Orion A cloud. These results are consistent with those found in cold dark clouds ($T_k \sim 10$ K), but both ratios decrease with increasing temperature. We also investigated the core dynamical characteristics through virial analysis, and found that the starless cores are in a stable equilibrium and tend to have high ratio of $R/R_{\rm cr}$, while the star-forming cores tend to have low ratio of $R/R_{\rm cr}$. This is consistent with the scenario by Nakano (1998), suggesting that the dissipation of turbulence is the important factor of star formation. Comparing the chemical evolution with dynamical states, we found that the $N(NH_3)/N(CCS)$ ratio seems to be correlated with $R/R_{\rm cr}$. This may mean the chemical evolution can be an indicator of the dynamical evolution of the core.

In order to understand the chemical compositions and evolutions in GMC cores in general, it is important to examine the chemical properties of different phases and environments of GMCs and a lot of star-forming dense cores. Taking into account the fact that ALMA is expected to be used to investigate the molecular cloud evolution in extragalaxies, it will be highly needed to search for specific molecules that can be used by ALMA.

In Vela C molecular cloud complex, Yamaguchi et al. (1999) mapped ^{12}CO, ^{13}CO, and C^{18}O ($J = 1 - 0$) lines and detected molecular outflows. By *Herschel* PACS and SPIRE observations at 70, 160, 250, 350, and 500 μm dust continuum emission, Hill et al. (2011) identified high column density filaments over the whole region, and showed differences in their column density and temperature probability distribution function (PDF) among regions. They revealed that the column density PDF of the 'Centre-Ridge region', which contains a high-mass star, is flatter than other regions, and shows a high column density tail.

In this study, we investigate the chemical characteristics of molecular cloud cores in the Vela C giant molecular cloud complex through mapping observations of HC_3N ($J = 10 - 9$) and N_2H^+ ($J = 1 - 0$), which can be used for ALMA band 3. The purpose of this chapter is to investigate whether HC_3N (a carbon-chain molecule) and N_2H^+ (a N-bearing molecule) are indicators of chemical evolution in the Vela C molecular cloud complex.

3.2 Observations toward the Vela C molecular cloud complex

Observations were carried out by the Mopra 22 m telescope located in Australia from 2014 May 10 to 25. We used the 3 mm MMIC receiver that can simultaneously record dual polarization data. We simultaneously observed HC_3N ($J = 10 - 9$) at 90.978989 GHz and N_2H^+ ($J = 1 - 0$) at 93.1737767 GHz. The employed spectrometer was the Mopra Spectrometer (MOPS) digital filter bank in the zoom-band mode. The spectral resolution was 33.57 kHz ($\sim$ 0.11 km s^{-1}). At 90 GHz, the half-power beam width (HPBW) and "extended beam efficiency" of the telescope are 42" and 50%, respectively (Ladd et al., 2005). We observed source 81 of the Vela-D molecular cloud identified by Morales Ortiz et al. (2012) once a day to check the stability of the intensity calibration. The absolute intensity accuracy was estimated to be less than 10%. We mapped $5' \times 5'$ box areas in the on-the-fly (OTF) mode. We observed a total of 7 regions, which were selected from bright $C^{18}O$ emission peaks. The $C^{18}O$ ($J = 1 - 0$) observations were previously carried out by Yamaguchi et al. (1999) with $2'$ resolution. Figure 3.1 shows the locations of the observed areas superimposed on a $Herschel\ SPIRE$ 500 μm map. The black boxes indicate OTF mapping area and white contours represent the N_2H^+ $J = 1 - 0$ velocity-integrated intensity map. The obtained data were smoothed to a HPBW of 53" with a 2D Gaussian function in order to improve the signal-to-noise ratio. The angular resolution is equivalent to 0.2 pc at a distance of 700 pc. It is worth noting that this resolution will identify objects that will form groups of stars. The typical rms noise level is about 0.08 K per channel. The telescope pointing was checked every 1.0 hour by observing the SiO maser source L2 Pup (RA,DEC (J2000) = $7^h13^m32.31$, -44°38′24".1). The pointing accuracy was better than 10". The upper energy levels (E_u/k) for HC_3N ($J = 10-9$) and N_2H^+ ($J = 1 - 0$) transitions are 24.01 and 4.47 K, respectively. The critical densities for these transitions are 3×10^5 and 5×10^5 cm^{-3} at 20 K, respectively (Sanhueza et al., 2012). However, Shirley (2015) suggested that N_2H^+ is excited at lower densities than the critical density, and the effective excitation densities may be lower than 5×10^5 cm^{-3}.

The observed data were reduced using "Livedata" and "Gridzilla", which are the most typical data reduction packages for the Mopra telescope[1]. "Livedata" fits and subtracts a linear baseline. The output of "Livedata" is recorded in single-dish fits format (sdfits). "Gridzilla" uses this output to regrid data onto a data cube using a Gaussian smoothing. The final data cubes were smoothed

[1] http://www.atnf.csiro.au/computing/software/livedata/index.html

to 15" grid size.

3.3 Results of the Vela C molecular cloud complex

3.3.1 Integrated intensity maps

Figures 3.2 through 3.8 show the integrated intensity maps in $T_{\rm A}^*$ scale. The HC_3N $J = 10 - 9$ contour maps superimposed on the N_2H^+ $J = 1 - 0$ gray-scale images. We plot the location of protostars identified by thermal emission at 5 wavebands from 70 to 500 μm using $PACS$ and $SPIRE$ cameras on board the $Herschel\ Space\ Observatory$ (Giannini et al. (2012); T. Giannini, private communication for the protostar coordinates). We also plot protostar candidates identified by the near-infrared (J, H, K_S) survey carried out by Baba et al. (2006) and AKARI-FIS Point Source Catalogue, which are Class 0 protostellar candidates (Sunada et al., 2009). We identified 25 local peaks in the velocity-integrated intensity maps of the HC_3N $J = 10 - 9$ and/or N_2H^+ $J = 1 - 0$ emission in these 7 regions. The criteria for identification are more than five sigma above the noise level for N_2H^+ and/or three sigma above the noise level for HC_3N. If the HC_3N peak is within the HPBW of the N_2H^+ peak, we use the HC_3N peak position. The identification of N_2H^+ emission peaks is more strict so that we can perform hyperfine fitting to satellite components. In Table 3.1, we list the positions of the detected HC_3N $J = 10 - 9$ and/or N_2H^+ $J = 1-0$ local peaks in the velocity-integrated intensity map and the line parameters of the HC_3N spectra measured toward these positions. The peak intensities and linewidths are obtained through Gaussian fitting. If local intensity peaks coincide with the protostars within 53", we define the peaks as star-forming cores. If local intensity peaks do not coincide with the protostars, we define the peaks as starless cores. A total of 12 peak positions were identified as star-forming. We assume that both lines trace sufficiently dense gas, and the starless cores identified in these lines will eventually form protostars. We found that the distributions of the HC_3N and N_2H^+ velocity-integrated intensities are similar to each other, suggesting that these molecular lines trace the same dense cores. Taking into account the fact that the scale of different distributions between HC_3N and N_2H^+ occurs at 0.1 pc scales in OMC-3 region (Tatematsu et al. (2008)), less prominent differences of intensity distributions would be due to our larger spatial resolution of 0.19 pc.

Table 3.1: HC_3N and N_2H^+ intensity peaks, coordinates, and HC_3N parameters.

Peak Position name	l °	b °	T_A^* (K)	$v_{\rm LSR}$(HC_3N) (km s^{-1})	dv(HC_3N) (km s^{-1})	Protostar
1	264.161	1.986				
2	264.140	1.960	0.41±0.06	6.6±0.1	1.00±0.18	P1
3	264.113	1.969	0.20±0.07	6.8±0.1	0.75±0.31	P2
4	264.086	1.944	0.22±0.05	6.5±0.3	1.10±0.59	
5	264.148	1.926	0.26±0.06	6.9±0.1	0.66±0.15	P3
6	264.31	1.733	0.30±0.07	7.1±0.1	0.83±0.21	
7	264.292	2.006	0.16±0.07	7.2±0.2	0.70±0.35	P4
8	264.304	1.725	0.23±0.06	6.6±0.1	0.99±0.31	P5
9	264.299	1.746				P6
10	264.279	1.733	0.24±0.09	6.8±0.1	0.37±0.21	
11	264.265	1.67	0.21±0.07	6.9±0.1	0.77±0.30	
12	264.975	1.633				P8
13	265.015	1.618	0.07±0.06	7.0±0.4	1.02±1.00	
14	264.965	1.587	0.29±0.06	6.4±0.1	0.99±0.24	P11
15	264.957	1.601	0.26±0.06	6.4±0.1	1.00±0.27	
16	265.138	1.439	0.35±0.05	8.3±0.1	1.37±0.71	
	265.138	1.439	0.24±0.03	6.6±0.2	2.29±0.34	
17	265.152	1.437	0.32±0.04	7.1±0.1	2.05±0.32	P12
18	265.167	1.433	0.29±0.04	7.2±0.2	2.14±0.34	P13
19	265.336	1.392	0.33±0.06	6.5±0.1	1.18±0.23	P14
20	265.292	1.432	0.13±0.09	6.8±0.1	0.85±0.24	P15
21	266.212	0.888	0.36±0.08	4.9±0.1	0.60±0.14	
22	266.245	0.871	0.23±0.08	5.1±0.1	0.67±0.26	
23	266.285	0.918				
24	266.279	0.928	0.29±0.06	4.5±0.1	1.24±0.27	
25	266.278	0.941	0.22±0.05	4.8±0.2	1.40±0.37	

3.3.2 Hyperfine fitting of N_2H^+ and column density

We fitted a hyperfine component model to the N_2H^+ spectra, and derived the optical depth, LSR velocity, linewidth, and excitation temperature assuming a uniform excitation temperature in the N_2H^+ hyperfine components. We also assume that the N_2H^+ emission fills the whole beam, that is, the beam filling factor is equal to unity. Figure 3.9 plots the linewidths of HC_3N against those of N_2H^+. The dashed line delineates the case that they are equal. We found a good correlation between them, suggesting that the molecular emission likely comes from the same volume. This is supported by the fact that the centroid velocities of the N_2H^+ and HC_3N lines are consistent with each other (see also Table 1 and 2). The intrinsic line strengths of the hyperfine components are adopted from Tiné et al. (2000). The optical depth $\tau_{\rm tot}$ is the sum of the optical depths of all the hyperfine components. At peak 16, we identified two velocity components and we fit a two-velocity-component hyperfine model. Figure 3.10 shows examples of hyperfine-fitting results at the peak positions of the cores. The column density is calculated by assuming local thermodynamic equilibrium (LTE). The formulation can be found, for example, in Equation (96) and (97) of Mangum & Shirley (2015). The range of the optical depths and the excitation temperatures are: $\tau_{\rm tot} = 0.9 - 9.6$ and $T_{\rm ex} = 3.3 - 10.4$ K (see also Table 3.2). Even in the most prominent hyperfine line ($F_1 = 2 - 1$, $F = 3 - 2$), the optical thickness is 0.259 $\tau_{\rm tot}$ (N_2H^+) (Tiné et al., 2000). Therefore, each N_2H^+ hyperfine emission line is optically thin in general because the median value of $\tau_{\rm tot}(N_2H^+)$ was estimated to be $\sim$2.4. The 1 σ error of the N_2H^+ column density was estimated by $\Delta\tau_{\rm tot}$ of the hyperfine fitting results. However, if we use the lower limit of the $\tau_{\rm tot} - \Delta\tau_{\rm tot}$, the $T_{\rm ex}(N_2H^+)$ can be too high to accept, that is, $T_{\rm ex}(N_2H^+)$ is higher than $T_{\rm ex}$(CO) $\sim 10 - 20$ K from Yamaguchi et al. (1999). In these cases, we use the symmetric error bars in the log scale by adopting the upper limit $\tau_{\rm tot} + \Delta\tau_{\rm tot}$.

For HC_3N, the optical depth has been derived by using multitransitional observations ($J = 4 - 3$, $J = 10 - 9$, $J = 12 - 11$, and $J = 16 - 15$) toward several GMCs including Orion A GMC by Bergin et al. (1996), and the opacity was found to be <1 at all positions. The HC_3N column density is calculated by assuming LTE and optically thin emission. The formulation can be found in Equation (13) of Sanhueza et al. (2012), for example. The excitation temperature $T_{\rm ex}(HC_3N)$ is assumed to be equal to that for N_2H^+. This assumption has some uncertainties, but the same excitation will be a best guess because both lines are thought to be optically thin and

would be only subthermally excited. We confirmed that the excitation temperature of N_2H^+ does not change between the star-forming and starless peaks suggesting that the excitation condition of the dense cores would not be changed. When hyperfine fitting is not successful due to low signal to noise ratios, we adopt $T_{ex}(HC_3N)$ = 5 K, which is the average value of $T_{ex}(N_2H^+)$. In the case of non-detection of these lines, we estimate the upper limit of the column densities from 3 sigma noise level. Table 3.2 summarizes the derived column densities.

Table 3.2: N_2H^+ hyperfine fitting results and column densities.

Peak Position name	$\tau_{tot}(N_2H^+)$	v_{LSR} (N_2H^+) (km s^{-1})	$dv(N_2H^+)$ (km s^{-1})	T_{ex} (K)	$N(N_2H^+)$ (cm^{-2})	$N(HC_3N)$ (cm^{-2})
1	1.2±1.1	7.40±0.06	1.70±0.21	4.7±1.5	$(5.7^{+5.3}_{-2.7})$E+12	<7.50E+12
2	6.2±2.2	6.68±0.04	1.00±0.11	3.8±0.2	$(1.3^{+4.8}_{-3.5})$E+13	(1.2±0.3)E+13
3	3.5±2.9	6.78±0.03	0.60±0.07	4.2±0.8	$(5.0^{+4.2}_{-2.3})$E+12	(3.4±1.8)E+12
4	5.2±4.2	7.04±0.06	0.82±0.16	3.9±0.5	$(9.1^{+7.3}_{-4.1})$E+12	(6.6±3.8)E+12
5	5.6±2.6	6.96±0.03	0.65±0.06	3.6±0.2	$(7.0^{+3.3}_{-2.2})$E+12	(7.3±1.9)E+12
6	3.9±3.6	7.22±0.04	0.63±0.09	3.9±0.7	$(5.2^{+5.0}_{-2.6})$E+12	(6.7±2.3)E+12
7				5	< 2.2E+12	(1.9±1.3)E+12
8	3.6±2.4	6.88±0.06	1.20±0.19	3.7±0.4	$(8.6^{+5.7}_{-3.4})$E+12	(7.4±3.1)E+12
9	6.0±2.6	7.54±0.03	0.70±0.07	3.8±0.2	$(8.6^{+3.5}_{-2.5})$E+12	<5.0E+12
10	3.0±2.6	6.84±0.05	0.84±0.12	4.1±0.8	$(5.8^{+5.2}_{-2.7})$E+12	(2.1±1.4)E+12
11				5	<2.4E+12	(2.7±1.4)E+12
12	1.7±1.6	7.44±0.03	0.80±0.09	5.4±1.7	$(4.8^{+4.7}_{-2.4})$E+12	<2.9E+12
13				5	< 3.1E+12	(1.2±1.2)E+12
14	3.8±1.7	6.41±0.03	0.99±0.10	4.5±0.5	$(1.0^{+4.4}_{-3.1})$E+13	(5.6±1.8)E+12
15	9.6±7.5	6.63±0.05	0.56±0.11	3.4±0.2	$(9.7^{+7.6}_{-4.3})$E+12	(1.1±0.4)E+13
16	1.0±0.8	8.28±0.05	1.23±0.12	9.2±4.5	$(1.0^{+0.8}_{-0.5})$E+13	(5.9±3.2)E+12
	1.9±1.7	6.61±0.10	1.14±0.20	4.8±1.5	$(6.2^{+5.8}_{-3.0})$E+12	(9.8±1.9)E+12
17	0.9±0.4	7.12±0.02	1.81±0.07	10.4±3.1	$(1.7^{+8.2}_{-5.5})$E+13	(8.1±1.7)E+12
18	2.1±0.6	7.23±0.03	1.58±0.08	5.9±0.7	$(1.3^{+0.4}_{-0.3})$E+13	(8.9±1.9)E+12
19	1.7±0.9	6.46±0.03	1.27±0.09	7.0±1.8	$(1.1^{+0.6}_{-0.4})$E+13	(5.1±1.4)E+12
20	3.0±2.0	6.85±0.03	0.69±0.06	4.9±1.0	$(6.3^{+4.2}_{-2.5})$E+12	(1.9±1.4)E+12
21	9.1±6.4	4.88±0.04	0.49±0.08	3.3±0.2	$(7.7^{+5.4}_{-3.2})$E+12	(1.1±0.4)E+13
22	1.4±1.4	4.98±0.04	0.99±0.12	5.3±1.4	$(4.7^{+4.6}_{-2.3})$E+12	(5.6±1.2)E+12
23	3.7±2.5	4.60±0.04	0.87±0.12	5.2±1.1	$(1.0^{+0.7}_{-0.4})$E+13	<3.4E+12
24	2.8±2.3	4.59±0.04	0.82±0.10	4.6±1.1	$(6.2^{+5.2}_{-2.8})$E+12	(6.9±1.9)E+12
25				5	< 4.3E+12	(5.2±1.8)E+12

3.3.3 Integrated intensity ratio and abundance ratio

We show the ratio of the velocity-integrated intensity of the N_2H^+ main hyperfine group $J = 1-0$, $F_1 = 2-1$ to that of the HC_3N $J = 10-9$ emission against the N_2H^+ column density in Figure 3.11. The integrated intensity ratios of N_2H^+/HC_3N are always greater than unity. It is also found

that the star-forming peaks have high ratios compared with those of starless peaks, suggesting that the N_2H^+/HC_3N integrated intensity ratio increases with time as star formation evolves. However, the substantial overlap between the star-forming and starless peaks can be seen. This unclear boundary will be discussed in the following section.

In molecular dense cores located in the Orion A GMC, it has been shown that the column density ratios of N_2H^+/CCS, NH_3/CCS, and NH_3/HC_3N are high in star-forming regions, while these are low in starless region (Ohashi et al. (2014b); Tatematsu et al. (2014a)). These results suggest that the carbon-chain molecules (HC_3N and CCS) trace chemically young gas, while N-bearing molecules (N_2H^+ and NH_3) trace later stages of chemical evolution. We investigate whether N_2H^+/HC_3N abundance ratio can be an indicator of the chemical evolution in the Vela C. Figure 3.12 shows the column density of N_2H^+ against that of HC_3N. We found a positive correlation between these column densities. We also found a systematic difference in the column densities between the star-forming and starless peaks. Figure 3.13 shows the column density ratio of N_2H^+/HC_3N against the linewidth of HC_3N. We find, on average, that the column density ratio of N_2H^+/HC_3N seems to be low toward starless peaks while it seems to be high toward star-forming peaks. The average value of the N_2H^+/HC_3N abundance ratio, excluding the data with upper limits, is $1.6^{+0.5}_{-0.4}$ for star-forming (median value is 1.5) and $1.2^{+0.4}_{-0.3}$ for starless peaks (median value is 0.9). This is similar to the tendency found in the Orion A GMC and nearby cold dark clouds. Ohashi et al. (2014b) suggested that column density ratio of NH_3/HC_3N decreases with increasing linewidth of HC_3N in the Orion A cloud. However, we found no correlation between column density ratio of N_2H^+/HC_3N and linewidths. The criterion between star-forming and starless in the Vela C is found around N_2H^+/$HC_3N \sim 1.4$. That is, N_2H^+/HC_3N may be $\lesssim 1.4$ in starless peaks, and $\gtrsim 1.4$ in star-forming peaks. Differences in the filling factors of these two molecules may affect the column density ratio. If the filling factor is equal to 0.5, the column density is $1.3 - 1.4$ times higher than that in the case of unity. Without having precise measurements of the filling factor, we assume the same filling factor, that is, unity for both of them. Even if the filling factor of HC_3N is systematically larger or smaller than that of N_2H^+, we will obtain the same tendency in comparison between starless and star-forming peaks, although the absolute value of the ratio may change. It should be noting that the uncertainties of the ratios are still large and we have to confirm these trends with high sensitivity observations in future.

Tatematsu et al. (2014a) observed CCS $J = 7 - 6$ and N_2H^+ $J = 1 - 0$ emission toward dense cores in the Orion A cloud, and showed a clearer boundary between star-forming and starless at $\sim 2 - 3$ (see their figure 20). However, in the present study, the boundary between star-forming and starless is less evident. Our large beam observations may have failed to resolve the core. If so, the column density of HC_3N may be underestimated with our observations, and the column density ratio of N_2H^+/HC_3N will become smaller than our estimate in such cold dense regions. Furthermore, identifications of protostars may not be complete in the Vela C. Giannini et al. (2012) identified protostars if 70 μm flux obtained by the *Herschel Space Observatory* is more than 3 σ from the best modified black body fit. Embedded protostars may not be identified by these criteria and we may have misidentified star-forming cores as starless cores. Finally, it may be also possible that the HC_3N $J = 10 - 9$ transition is not a appropriate chemical evolution tracer as the CCS $J = 7 - 6$ transition. This is because the upper state energy for the HC_3N $J = 10 - 9$ transition is ~ 24 K, which is higher than that for the CCS $J = 7 - 6$ transition of ~ 15 K. The HC_3N $J = 10 - 9$ transition may be emitted in warm gas in star-forming regions rather than in young cold gas. It is also known that HC_3N emissions show the wing emission toward Orion KL (Ungerechts et al., 1997) and strong emission in the circumnuclear disk of NGC 1068 (Takano et al., 2014). The HC_3N molecule will not trace always chemically young gas.

Finally, figure 3.14 plots the column density ratio of N_2H^+/HC_3N against Galactic longitude. The lower longitude corresponds to the northern part of the Vela C and the higher longitude corresponds to the southern part. The boundary between star-forming and starless cores may remain unchanged along the different locations of the cores. We find no evidence for global chemical variation in Vela C, in contrast as has been observed in Orion A GMC by Tatematsu et al. (2010).

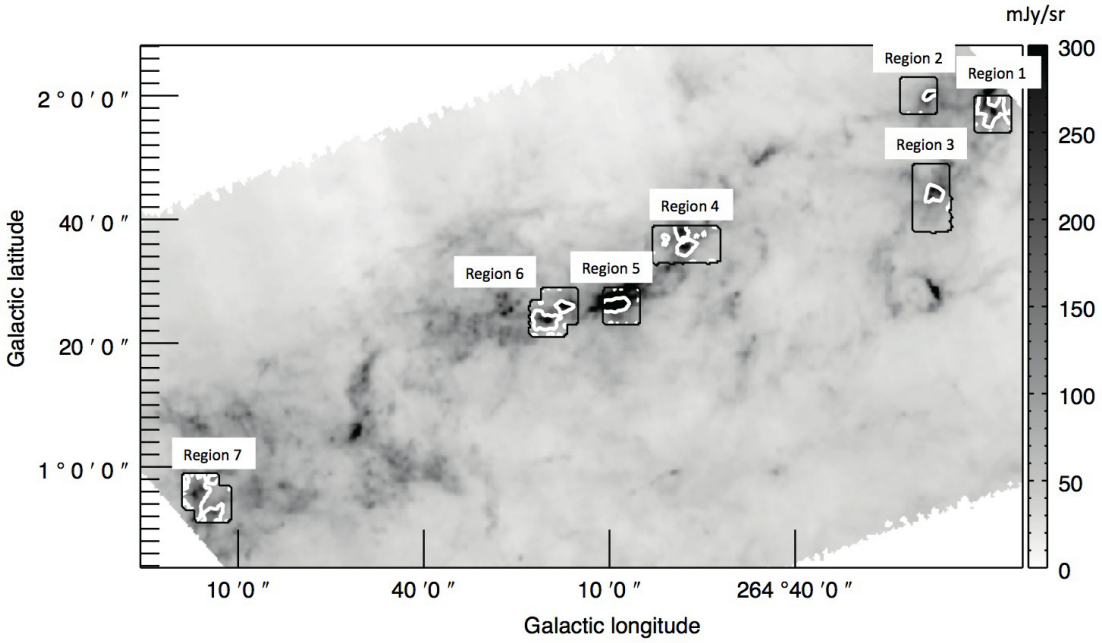

Figure 3.1: The N_2H^+ $J = 1 - 0$ velocity-integrated intensity maps in contours are imposed on the gray scale map of the $Herschel\ SPIRE$ 500 μm dust emission. The velocity range of integration for the N_2H^+ line emission is from 3.5 to 9.0 km s^{-1}. The contours represent 0.4 K km s^{-1}.

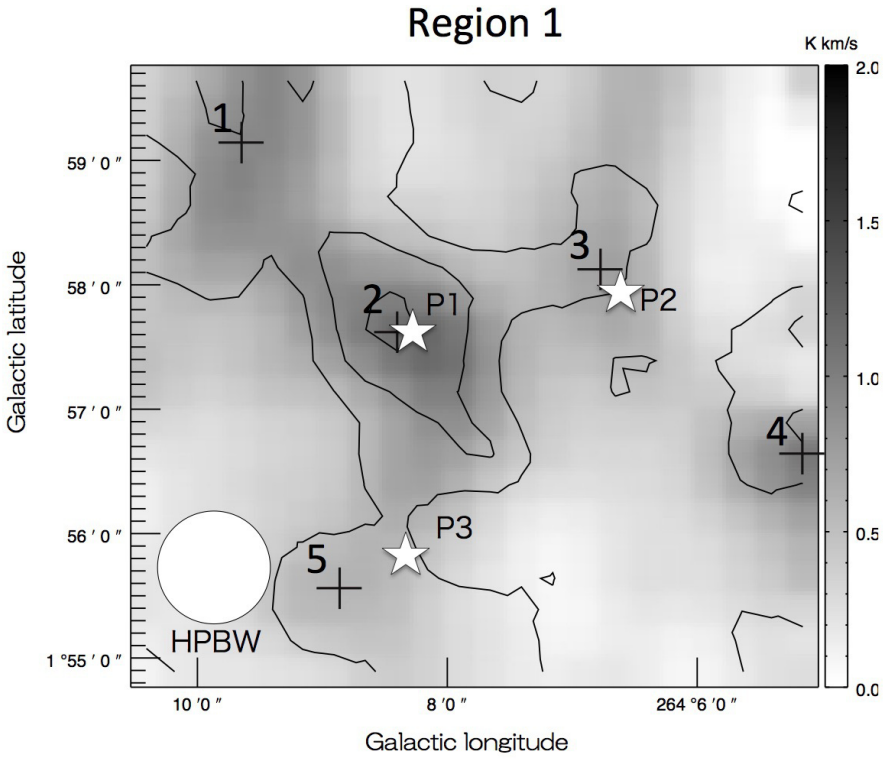

Figure 3.2: The HC_3N $J = 10 - 9$ velocity-integrated intensity map is superimposed on the gray scale map of the integrated intensity of the main hyperfine component group N_2H^+ $J = 1 - 0$, $F_1 = 2 - 1$. The integrated velocity range for both molecular lines is from 5.0 to 9.0 km s^{-1}. The lowest contour and the contour step are 3 σ. The 1 σ noise level for the contour is 0.05 K km s^{-1}. The white star signs represent the locations of the protostars in Giannini et al. (2012). The plus signs represent the locations of the N_2H^+ and HC_3N intensity peaks.

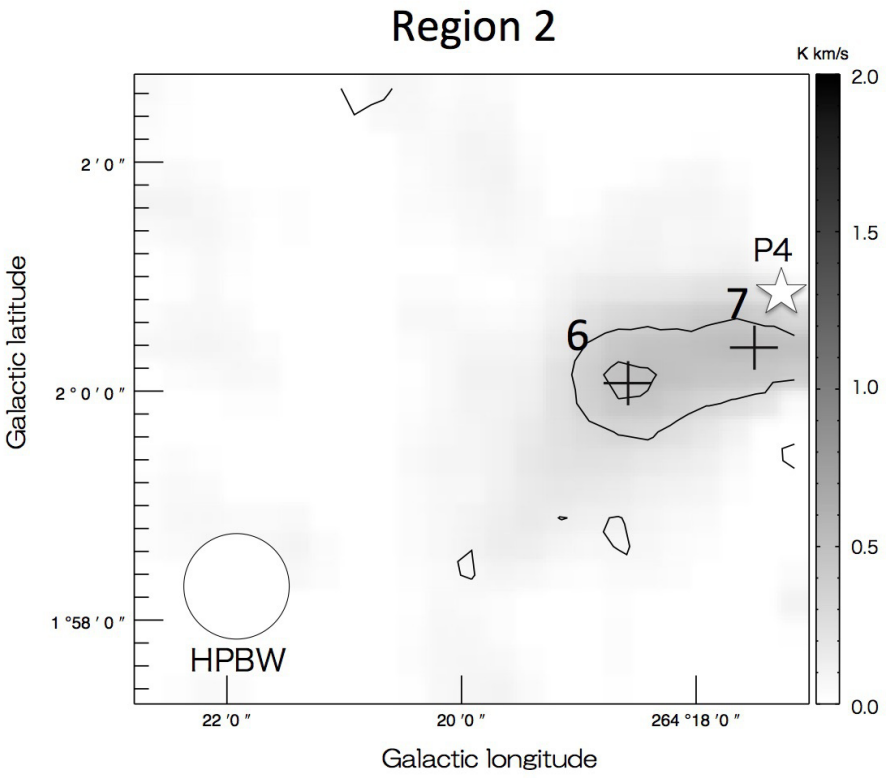

Figure 3.3: The same as figure 3.2 but for region 2. The integrated velocity range for the molecular line emission is from 6.0 to 8.0 km s^{-1}. The lowest contour and the contour step are 3 σ. The 1 σ noise level is 0.04 K km s^{-1}.

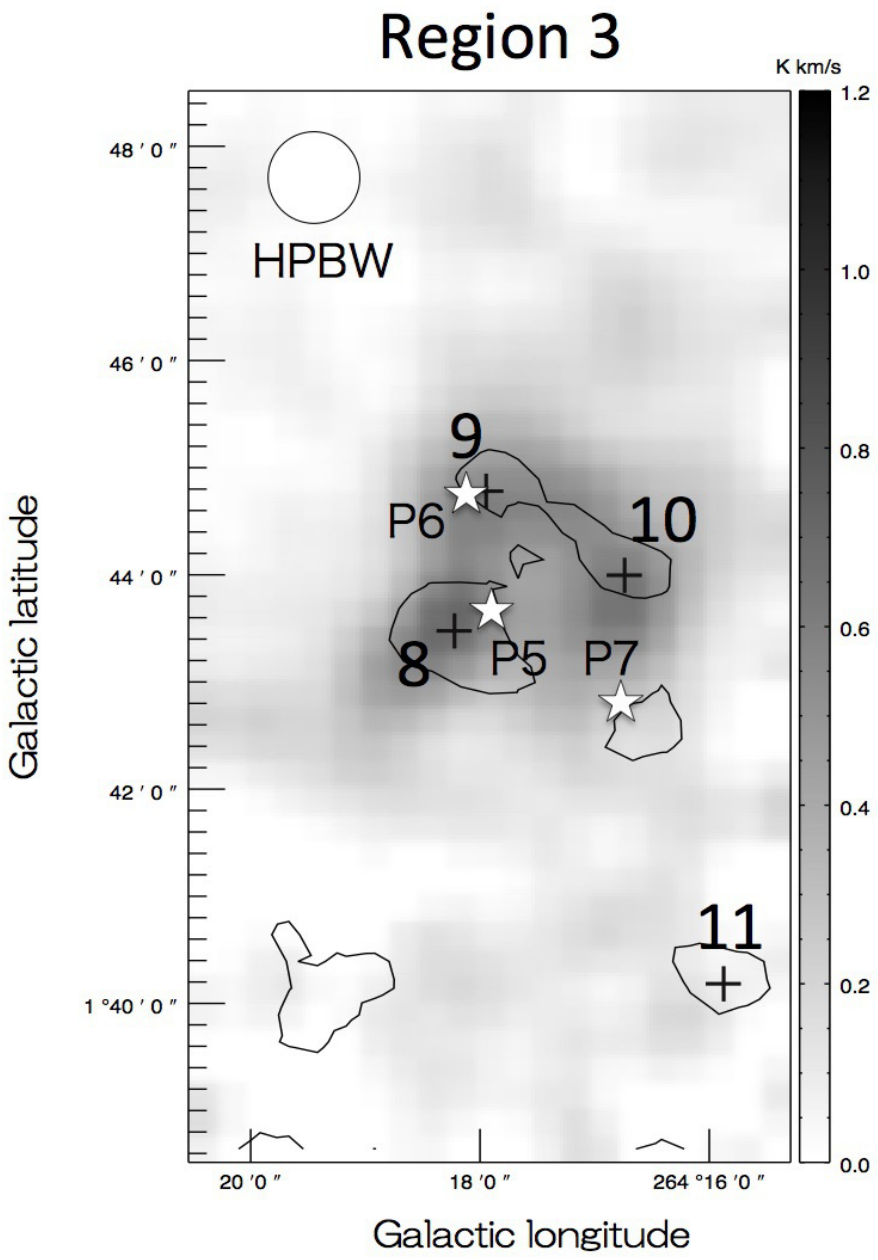

Figure 3.4: The same as figure 3.2 but for region 3. The integrated velocity range for the molecular line emission is from 6.0 to 8.0 km s^{-1}. The lowest contour and the contour step are 3 σ. The 1 σ noise level is 0.04 K km s^{-1}.

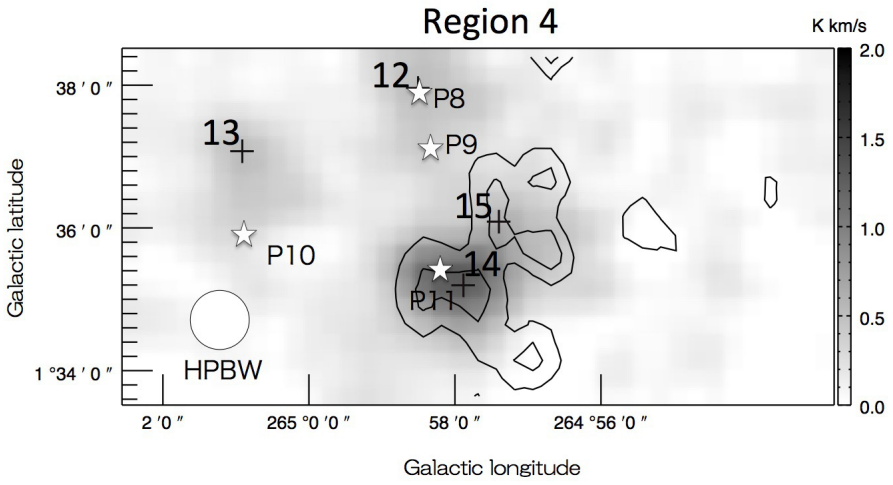

Figure 3.5: The same as figure 3.2 but for region 4. The integrated velocity range for the molecular line emission is from 5.0 to 7.5 km s^{-1} . The lowest contour is 3 σ, and the contour step is 2 σ. The 1 σ noise level is 0.05 K km s^{-1}.

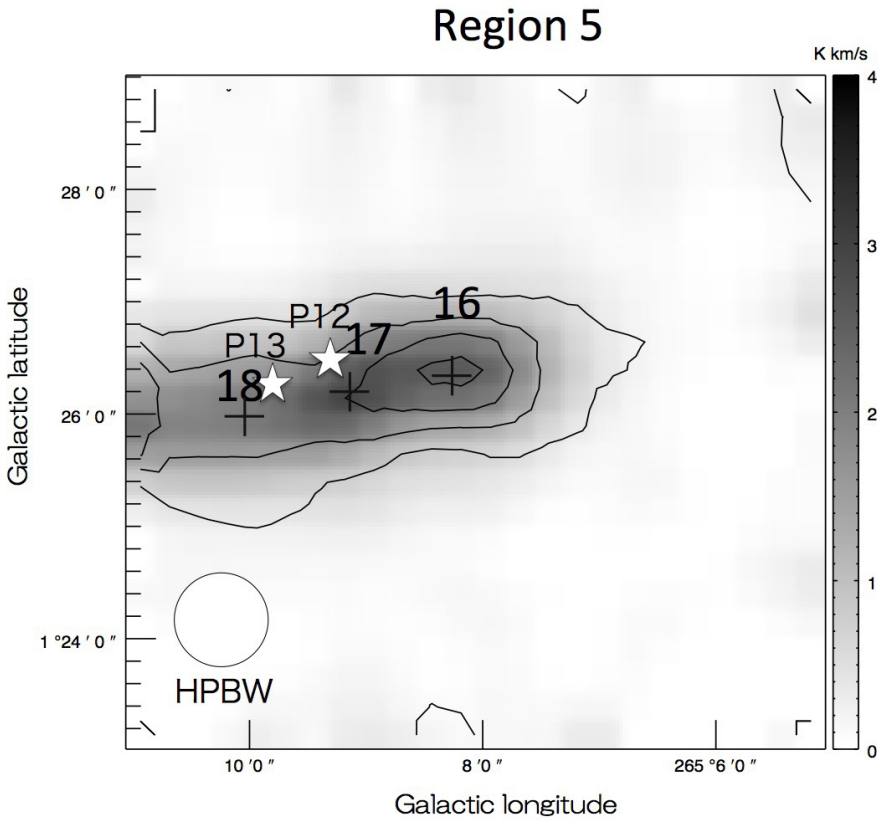

Figure 3.6: The same as figure 3.2 but for region 5. The integrated velocity range for the molecular line emission is from 6.0 to 9.0 km s^{-1}. The lowest contour and the contour step are 3 σ. The 1 σ noise level is 0.06 K km s^{-1}.

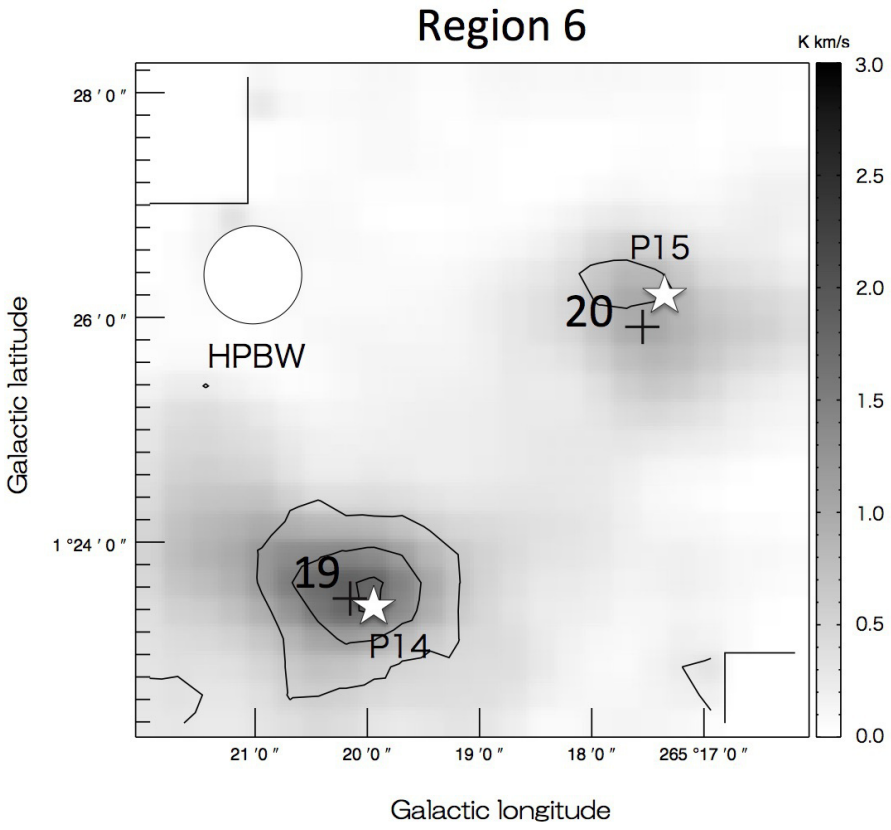

Figure 3.7: The same as figure 3.2 but for region 6. The integrated velocity range for the molecular line emission is from 6.0 to 9.0 km s^{-1}. The lowest contour and the contour step are 3 σ. The 1 σ noise level is 0.05 K km s^{-1}.

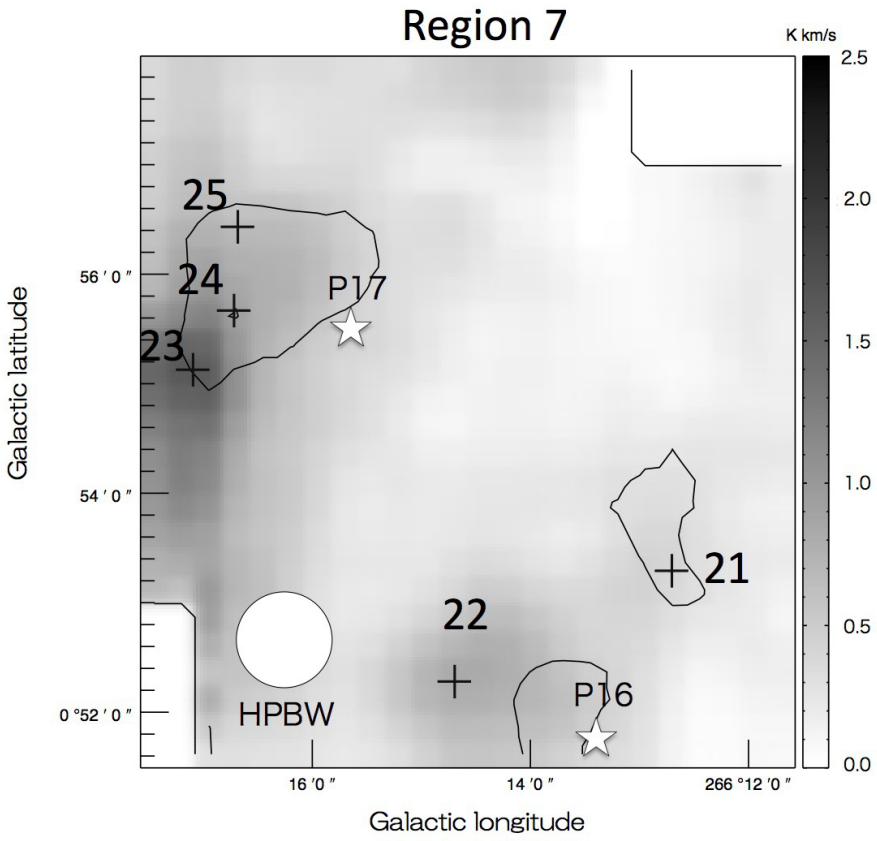

Figure 3.8: The same as figure 3.2 but for region 7. The integrated velocity range for the molecular line emission is from 3.5 to 6.0 km s^{-1}. The lowest contour and the contour step are 3 σ. The 1 σ noise level is 0.07 K km s^{-1}.

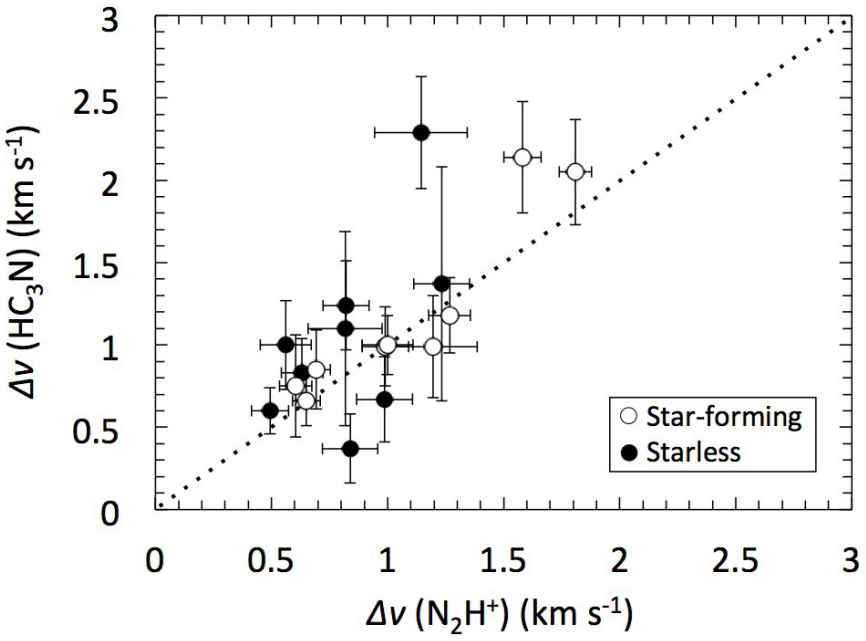

Figure 3.9: The HC_3N linewidth against that the N_2H^+ linewidth. The dotted line represents unity.

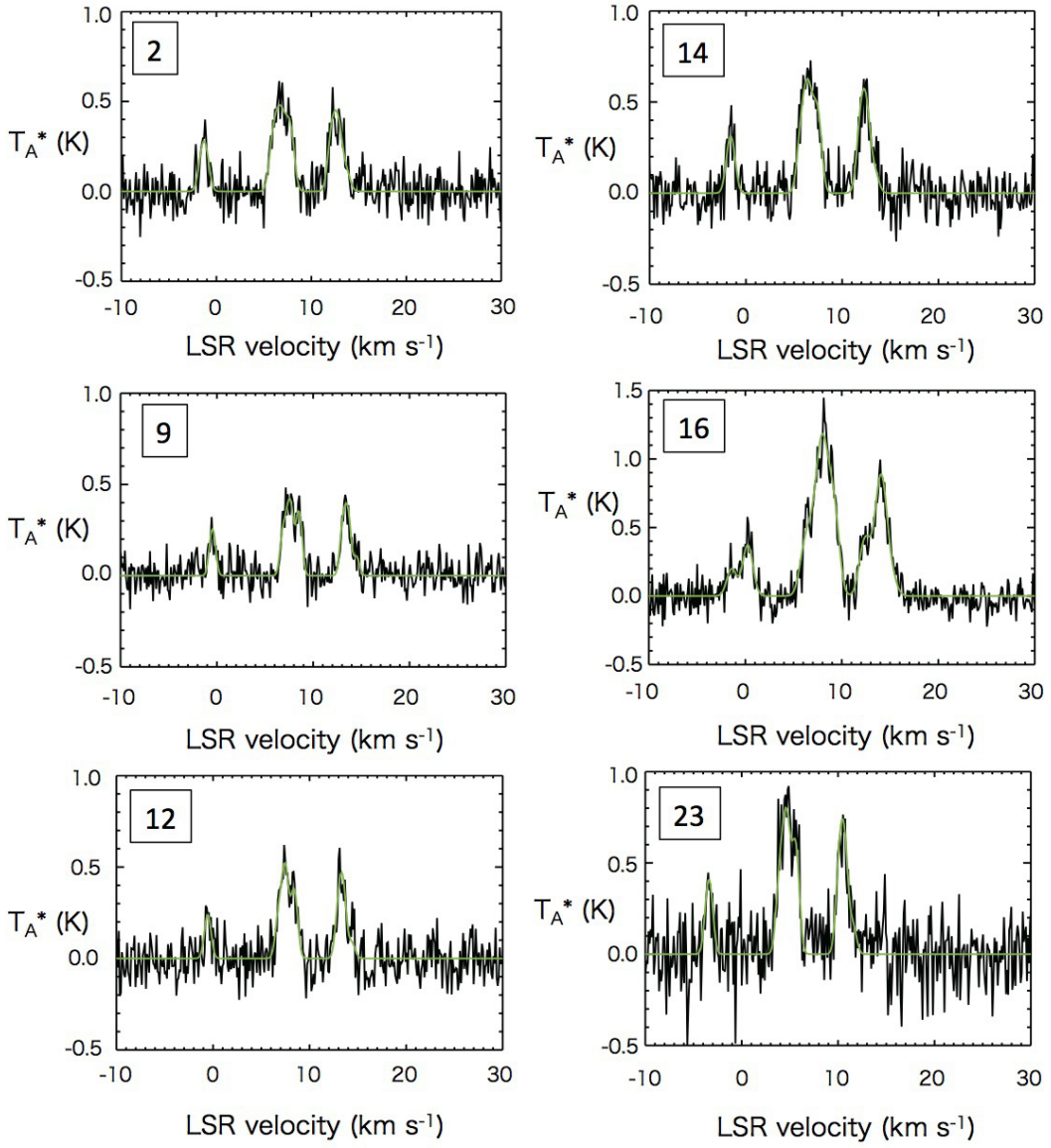

Figure 3.10: Hyperfine-fitting results for the N_2H^+ ($J = 1 - 0$) spectra for the six intensity peaks.

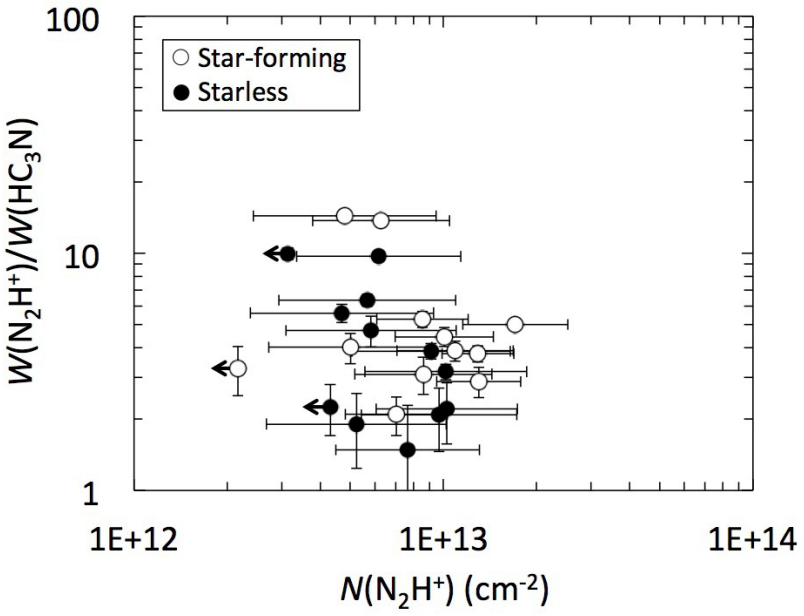

Figure 3.11: The integrated intensity ratio of N_2H^+ to HC_3N against the N_2H^+ column density. The vertical error bar represents the 1 σ noise level of integrated intensity ratio of N_2H^+ to HC_3N. The horizontal error bar represents the 1 σ error corresponding to the N_2H^+ $J = 1 - 0$ hyperfine line fitting.

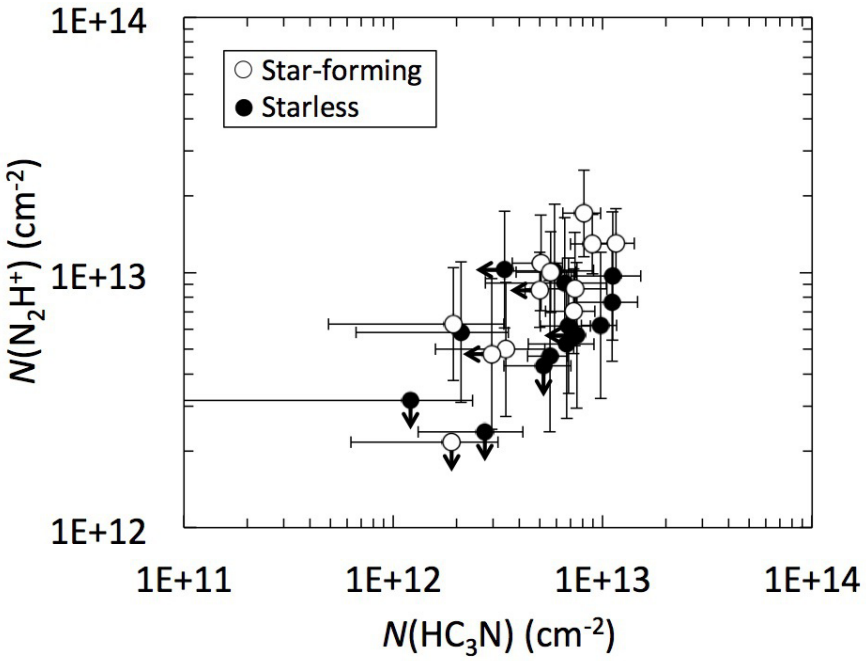

Figure 3.12: The N_2H^+ versus HC_3N column density. The vertical error bar represents the 1 σ error corresponding to the N_2H^+ $J = 1 - 0$ hyperfine line fitting. The horizontal error bar represents the 1 σ error in the HC_3N assuming that the excitation temperature $T_{\rm ex}(HC_3N)$ is equal to that for N_2H^+.

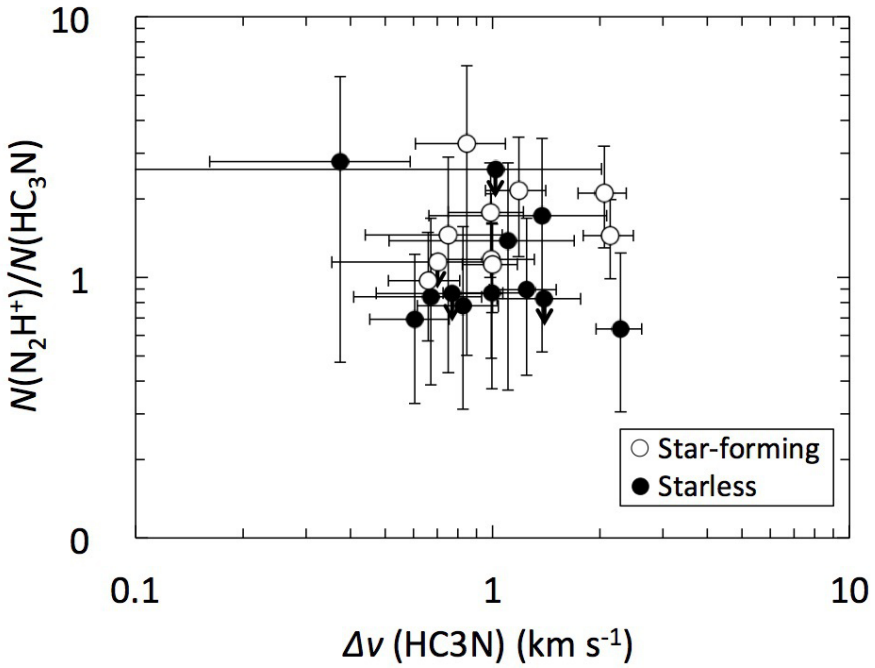

Figure 3.13: The column density ratio of N_2H^+/HC_3N against the linewidth of the HC_3N emission.

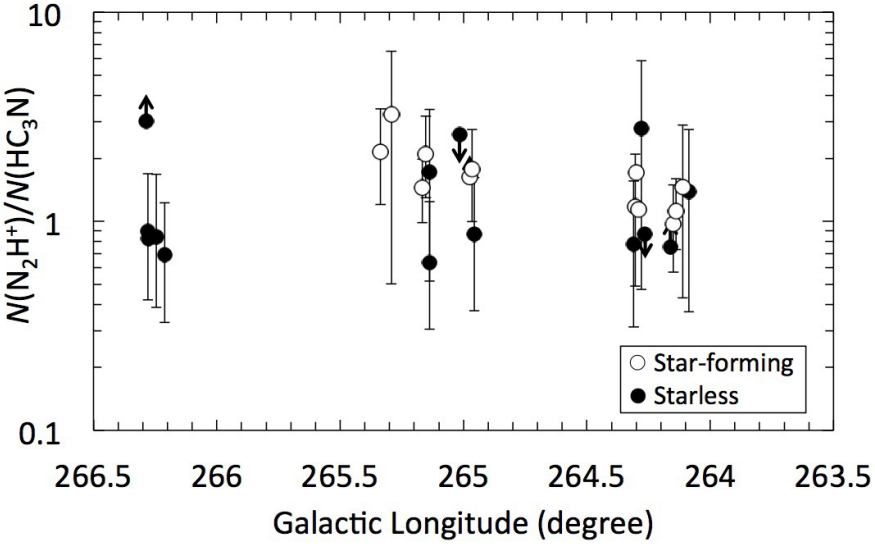

Figure 3.14: The column density ratio of N_2H^+/HC_3N against the Galactic longitude.

Chapter 4

Discovery of evidence for turbulence dissipation in a chemically-selected evolved starless core

A part of this chapter has been published as Ohashi, Satoshi; Tatematsu, Ken'ichi; Sanhueza, Patricio; Hirota, Tomoya; Choi, Minho; & Mizuno, Norikazu, MNRAS, 459, 4130 (Ohashi et al., 2016c)

Abstract

We report the detection of a wing component in NH_3 emission toward the starless core TUKH122 with subthermal turbulence in the Orion A cloud. This NH_3 core is suggested to be on the verge of star formation because the turbulence inside the NH_3 core is almost completely dissipated, and also because it is surrounded by CCS, which resembles the prestellar core L1544 in Taurus showing infall motions. Observations were carried out with the Nobeyama 45 m telescope at 0.05 km s^{-1} velocity resolution. We find that the NH_3 line profile consists of two components. The quiescent main component has a small linewidth of 0.3 km s^{-1} dominated by thermal motions, and the red-shifted wing component has a large linewidth of 1.36 km s^{-1} representing turbulent motions. These components show kinetic temperatures of 11 K and < 30 K, respectively. Furthermore, there is a clear velocity offset between the NH_3 quiescent gas ($V_{\rm LSR} = 3.7$ km s^{-1}) and the turbulent gas ($V_{\rm LSR} = 4.4$ km s^{-1}). The centroid velocity of the turbulent gas corresponds to that of the surrounding gas traced by the ^{13}CO ($J = 1 - 0$) and CS ($J = 2 - 1$) lines. LVG model calculations for CS and CO show that the turbulent gas has a temperature of $8 - 13$ K and an H_2 density of $\sim 10^4$ cm^{-3}, suggesting that the temperature of the turbulent component is also ~ 10 K. The detections of both NH_3 quiescent and wing components may indicate a sharp transition from the turbulent parent cloud to the quiescent dense core.

4.1 Introduction of this chapter

In previous chapters 2 and 3, we found that the chemical evolutions can be used even in GMC cores (the Orion A cloud and Vela C molecular cloud complex) wtih the $N(N_2H^+)/N(CCS)$, the $N(NH_3H)/N(HC_3N)$ and so on. As a next step, we are very much interested in searching for dense cores on the verge of star formation (onset on initial conditions of star formation).

We have found such a thermal starless core in the Orion A cloud through the $N(N_2H^+)/N(CCS)$ chemical evolution and VLA NH_3 observations. TUKH122 is a starless but takes the highest ratio of the $N(N_2H^+)/N(CCS) \sim 2-3$ within starless.

Tatematsu et al. (2014b) observed the NH_3 $(J,K)=(1,1)$ and CCS ($J_N=4_3-3_2$) emission lines toward the TUKH122 core with the Very Large Array (VLA). Surprisingly, they revealed narrow NH_3 line profiles ($\Delta v \sim 0.2$ km s^{-1}), in contrast to the broader previous observed CS ($J=1-0$) line profiles ($\Delta v \sim 0.8$ km s^{-1}). They also found that an NH_3 oval structure (core) is surrounded by CCS emission. This configuration is quite similar to that of the starless cores L1544 and L1498 in Taurus (Aikawa et al., 2001; Lai & Crutcher, 2000). The prestellar core L1544 displays infall motions (Tafalla et al., 1998), which means that NH_3 cores surrounded by CCS emission might indicate that these cores are chemically evolved and on the verge of the star formation.

Tatematsu et al. (1993) showed the core mass function (CMF) using CS ($J=1-0$) line in the Orion A cloud. The parent CS ($J=1-0$) core mass of TUKH122 is derived to be $\sim 48\ M_\odot$. Their CMF indicates that the CS mass of $\sim$48 $M_\odot$ is typical in the Orion A cloud. Therefore, we consider this core is one of typical dense cores in the Orion A cloud and is on the verge of the star formation. Because most stars are formed as clusters and their majority of birth places are giant molecular clouds (GMCs), it is of great interest to know how dense cores are formed in GMCs.

Here, we report new single-pointing observations of the NH_3 $(J,K)=(1,1)$ and $(2,2)$ emission lines toward the TUKH122 core at 0.05 km s^{-1} velocity resolution using the Nobeyama 45 m telescope in order to investigate the kinematics and the physical conditions of the core. Measurements of the NH_3 inversion lines are ideal for temperature of dense gas (Ho & Townes, 1983). Therefore, we will provide kinetic temperature and turbulence information from a good example of a dense core on the verge of star formation.

4.2 Observations toward the TUKH122 core

Single-pointing observation was carried out with the Nobeyama 45 m telescope on 2015 March 4. At 23 GHz, the half-power beam width (HPBW) and main beam efficiency (η) of the telescope were 73" and 0.825, respectively. The observations were perfomred in the position switch mode. For the receiver front end, we employed the 20 GHz HEMT receiver (H22). For the back end, we used the SAM45 digital spectrometer with a spectral resolution of 3.81 kHz (0.05 km s^{-1} at 23 GHz) and a bandwidth of 16 MHz. The NH_3 $(J, K) = (1, 1)$ and $(2, 2)$ lines were simultaneously observed. We used rest frequencies of 23.69449 and 23.72263 GHz for NH_3 $(J, K) = (1, 1)$ and $(2, 2)$, respectively (Kukolich, 1967). The system noise temperatures ranged from 90 to 96 K. The standard chopper wheel method was used, and the intensity is reported in terms of the main-beam temperature $T_{\rm mb}$, which is obtained by dividing the antenna temperature $T_{\rm A}^{\star}$ by the main beam efficiency. The on-source integration time was $\sim$ 52 min, resulting in an rms noise level of 37 mK in $T_{\rm mb}$ for the NH_3 $(J, K) = (1, 1)$ observations in the dual polarization mode, and 51 mK in $T_{\rm mb}$ for the NH_3 $(J, K) = (2, 2)$ observations in the single polarization mode. The telescope pointing was checked at the beginning of the observation by observing the SiO maser source Orion KL and was better than 10".

4.3 Results and Discussion

Figure 4.1 shows the location of TUKH122 on top of 70 μm, thermal dust continuum map, and NH_3 emission map. The bright 70 μm source corresponds to TUKH123, which contains six protostars identified by *Spitzer* (Megeath et al., 2012). On the other hand, no 70 μm emission was detected toward the TUKH122 core, which is consistent with the fact that the TUKH122 core has no protostars. We can see a filamentary structure elongated from northwest to southeast toward the TUKH122 core (Figure 4.1). The width of the filament is about 0.1 pc and its length is 0.5 pc. On the NH_3 map, an oval structure with embedded condensations is seen toward TUKH 122.

4.3.1 Hyperfine fitting and derivation of physical parameters

Figure 4.2 shows the line profile and hyperfine fitting of the NH_3 $(J, K) = (1, 1)$ and $(2, 2)$ lines obtained with the Nobeyama 45 m telescope. We identified a total of nine hyperfine components

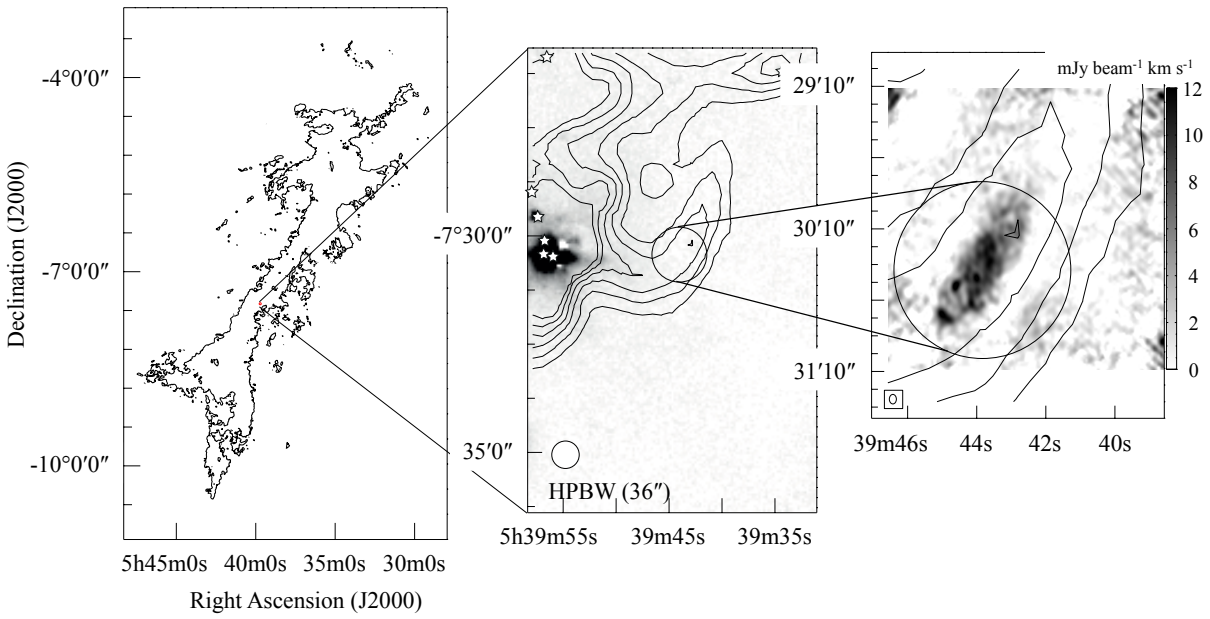

Figure 4.1: (Left): The Orion A large map taken by $Herschel\ SPIRE$ 500 μm dust emission is shown in a contour. The contour level is 13 mJy. (Middle): The $Herschel\ SPIRE$ 500 μm dust emission map in contour is imposed on the grey scale map of the $Herschel\ PACS$ 70 μm emission. The lowest contour level is 92 mJy (10% of the peak flux in the map) and the contour interval is 18.4 mJy (2% of the peak flux in the map). The center circle represents the beam size of the Nobeyama 45 m telescope at 23 GHz. The bottom-left circle is the $Herschel$ beam size (36") at 500 μm. (Right): The NH_3 velocity-integrated intensity map in grey scale of the main NH_3 $(J, K) = (1, 1)$ component toward TUKH122 obtained with VLA. The velocity integration range is from $V_{\rm LSR} = 3.2$ to 4.4 km s^{-1}. The contours represent 500 μm dust continuum emission (same contour levels used in the left panel). The bottom-left circle is the VLA synthesized beam (4".1 $\times$ 3".1).

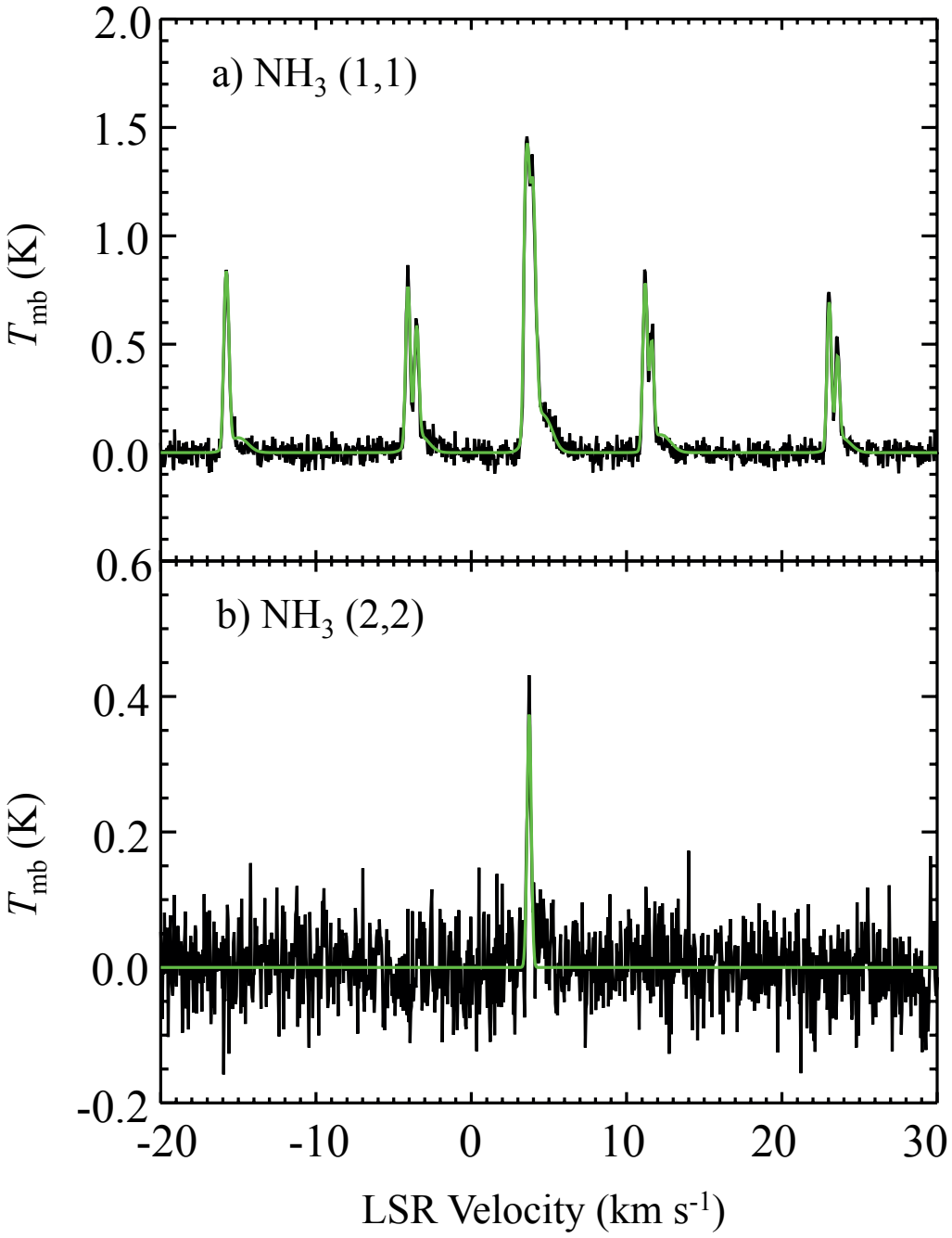

Figure 4.2: (a) The NH_3 $(J, K) = (1, 1)$ spectrum and hyperfine-fitting result. The green line represents the best fit model of the hyperfine fitting. (b) The NH_3 $(J, K) = (2, 2)$ spectrum and Gaussian-fitting result. The green line represents the best fit model of the Gaussian-fitting.

with $T_{\rm mb} \sim 0.8 - 1.5$ K in the NH_3 $(J, K) = (1, 1)$ line. The hyperfine fitting was performed to the NH_3 $(J, K = 1, 1)$ spectra by using equations:

$$T_{\rm A}^{\star}(v) = \eta[J_{\nu}(T_{\rm ex}) - J_{\nu}(T_{\rm bg})][1 - \exp(-\tau(v))], \tag{4.1}$$

where

$$\tau(v) = \tau_{\rm tot} \sum_{i} \frac{s_i}{4.284} \exp\left\{-4 \ln 2 \left(\frac{v - v_i - v_{\rm LSR}}{\Delta v}\right)^2\right\}. \tag{4.2}$$

The optical depth $\tau_{\rm tot}$ is the sum of the centroid optical depths of all the hyperfine components. The background temperature $T_{\rm bg}$ is 2.7 K. J_{ν} is the Planck function in temperature units. The free parameters are the optical depth ($\tau_{\rm tot}$), LSR velocity ($V_{\rm LSR}$), linewidth (Δv), and excitation temperature ($T_{\rm ex}$). We assume a uniform excitation temperature in all NH_3 hyperfine components. The intrinsic line strengths (s_i) and velocity offsets (v_i) of the hyperfine components are adopted from Levshakov et al. (2010). We fit the hyperfine structure with a least-squares Gaussian hyperfine structure fitting routine written in IDL. Fitting is optimized by the use of the Levenberg-Marquardt algorithm (for non-linear fitting). Iterations are performed until the solutions converge.

Because we identified another component (wing component) in the NH_3 $(J, K) = (1, 1)$ spectrum, we fit a two-velocity-component hyperfine model. The fitting results of the wing emission will be discussed in the following subsection. The fitting results of the quiescent component are: $\tau_{\rm tot} = 8.4 \pm 0.1$, $V_{\rm LSR} = 3.74 \pm 0.01$ km s^{-1}, $\Delta v = 0.30 \pm 0.001$ km s^{-1}, and $T_{\rm ex} = 4.14 \pm 0.05$ K. The NH_3 hyperfine components are moderately optically thick. It is found that the core is thermally dominated because the observed linewidth is close to the thermal linewidth $\Delta v({\rm th}) = (8 \ln 2\, kT_{\rm k}/m)^{1/2}$, which is 0.16 km s^{-1} for NH_3 at $T_{\rm k} = 10$ K. Here, k is the Boltzmann constant, and m is the mass of the molecule.

We performed a single Gaussian fitting to the NH_3 $(J, K) = (2, 2)$ spectrum because there is only one detected velocity component and hyperfine lines are not detected. The fitting results are: peak intensity of $T_{\rm mb} = 0.37 \pm 0.03$ K, centroid velocity of $V_{\rm LSR} = 3.728 \pm 0.014$ km s^{-1}, and linewidth of $\Delta v = 0.31 \pm 0.03$ km s^{-1}. The optical depth of $\tau(2, 2)$ can be derived from equation (1) assuming that NH_3 $(J, K) = (1, 1)$ and $(2, 2)$ transition have the same excitation temperature and a filling factor of unity for both transitions. The rotational temperature of NH_3 was derived from the $(J, K) = (1, 1)$ and $(2, 2)$ transitions by following Bachiller et al. (1987) and equation

(4.3)

$$T_{\rm rot} = \frac{41.5}{\ln\left(2.35\frac{\tau_m(1,1)}{\tau_m(2,2)}\frac{\Delta v_{1,1}}{\Delta v_{2,2}}\right)}, \tag{4.3}$$

where $\tau_m(1,1)$ is the optical depth of the main hyperfine component group ($\tau_m(1,1) = 0.5 \times \tau_{\rm tot}$). Following Mangum et al. (1992) and Mangum & Shirley (2015), the column density was derived as

$$N(J,K) = 3.96 \times 10^{12} \frac{J(J+1)}{K^2} \times \left\{\frac{1+\exp(-h\nu/kT_{\rm ex})}{1-\exp(-h\nu/kT_{\rm ex})}\right\}\tau(J,K)\Delta v \ \ {\rm cm}^{-2}. \tag{4.4}$$

The total column density was obtained by using

$$N({\rm NH_3}) = 0.0138 \times N(1,1) \exp\left(\frac{23.1}{T_{\rm rot}}\right) T_{\rm rot}^{3/2}. \tag{4.5}$$

From these equations, we derived a rotation temperature of $T_{\rm rot} = 10.6 \pm 1.5$ K and $N({\rm NH_3}) = (5.8 \pm 0.5) \times 10^{14}$ cm^{-2}. In order to estimate the kinetic temperature $T_{\rm kin}$, we used the relations derived by Tafalla et al. (2004)

$$T_{\rm kin} = \frac{T_{\rm rot}}{1 - \frac{T_{\rm rot}}{42}\ln\left[1 + 1.1\exp(-16/T_{\rm rot})\right]} \tag{4.6}$$

The kinetic temperature is derived to be $T_{\rm kin} = 11 \pm 2$ K. The value of $T_{\rm kin} = 11$ K is consistent with the fact that there is no heating source in this core. We also investigate how the filling factor affects equation (1). If the filling factor is 0.5, the kinetic temperature and the column density are derived to be $T_{\rm kin} = 11$ K and $N({\rm NH_3}) = 7.8 \times 10^{14}$ cm^{-2}, respectively. The kinetic temperature is not significantly affected by the filling factor because it is derived from the intensity ratio of NH$_3$ $(J,K) = (1,1)$ and $(2,2)$ emission. Again, we assume that both transitions have the same filling factor.

4.3.2 Wing emission

In addition to the narrow linewidth component of $\Delta v = 0.3$ km s^{-1}, we identified a red-shifted wing component in the NH$_3$ $(J,K) = (1,1)$ spectrum for the first time for this source (see Figures

Table 4.1: Fitting results of various molecular lines toward TUKH122

molecular lines	τ	$V_{\rm LSR}$ (km s^{-1})	Δv (km s^{-1})	$T_{\rm ex}$ (K)
NH_3 $(J, K = 1, 1)$ main	8.4±0.1	3.74±0.01	0.30	4.14±0.05
NH_3 $(J, K = 1, 1)$ wing	3.23±0.03	4.40±0.02	1.36	2.9±0.1
CS $(J = 2 - 1)$		4.37±0.33	1.7	
^{13}CO $(J = 1 - 0)$		4.51±0.09	2.6	

4.2 a and 4.3).

To analyze the wing emission, we performed the hyperfine fitting including the quiescent main component and the wing component, simultaneously. The fitting results of the wing component are: $\tau_{\rm tot} = 3.23\pm0.03$, $V_{\rm LSR} = 4.40\pm0.02$ km s^{-1}, $\Delta v = 1.36\pm0.01$ km s^{-1}, and $T_{\rm ex} = 2.9\pm0.1$ K, suggesting that the wing emission is turbulent. Because we were unable to detect a counterpart in the NH_3 $(J, K) = (2, 2)$ emission, we estimated the upper limit to the kinetic temperature to be 30 K assuming the 3 σ upper limit of the NH_3 $(J, K) = (2, 2)$ emission. The centroid velocity of NH_3 quiescent gas is 3.7 km s^{-1}, while that of the wing/high velocity gas is 4.4 km s^{-1}. The velocity offset is about 0.7 km s^{-1}, more than twice the linewidth of the quiescent component. In Figure 4.3, we show the CS $(J = 2 - 1)$, ^{13}CO $(J = 1 - 0)$, and NH_3 $(J, K = 1, 1)$ line profiles toward TUKH122. The ^{13}CO $(J = 1 - 0)$ and CS $(J = 2 - 1)$ lines are convolved with a Gaussian kernel to match the beam size of the NH_3 observations (73"). These lines were observed by Tatematsu et al. (1993, 1998, 2014a). We find that the ^{13}CO $(J = 1 - 0)$ and CS $(J = 2 - 1)$ emission lines are dominated by turbulent motions and their velocity centroids are consistent with that of the NH_3 turbulent gas rather than that of the NH_3 quiescent gas within the uncertainties (see also table 1). A rest frequency of 110.201353 GHz was used for ^{13}CO $(J = 1 - 0)$ (Ulich & Haas, 1976).

In addition to the upper limit to the kinetic temperature of the turbulent gas explained above, we tried to obtain the temperature by another method. We make LVG calculations (e.g., Scoville & Solomon, 1974; Goldreich & Kwan, 1974) for the multitransition CS $(J = 1 - 0)$, CS$(J = 2 - 1)$ and C^{34}S $(J = 2 - 1)$ data to derive the kinetic temperature of the turbulent gas. LVG analysis was made by using the RADEX software (van der Tak et al., 2007). The collision rates for CS are taken from Lique et al. (2006). We assume that the CS lines are emitted from similar volumes and they are from a uniform density sphere.

In LVG calculations, we investigate the parameter range of $n(H_2) = 10^3 - 10^5$ cm^{-3} and

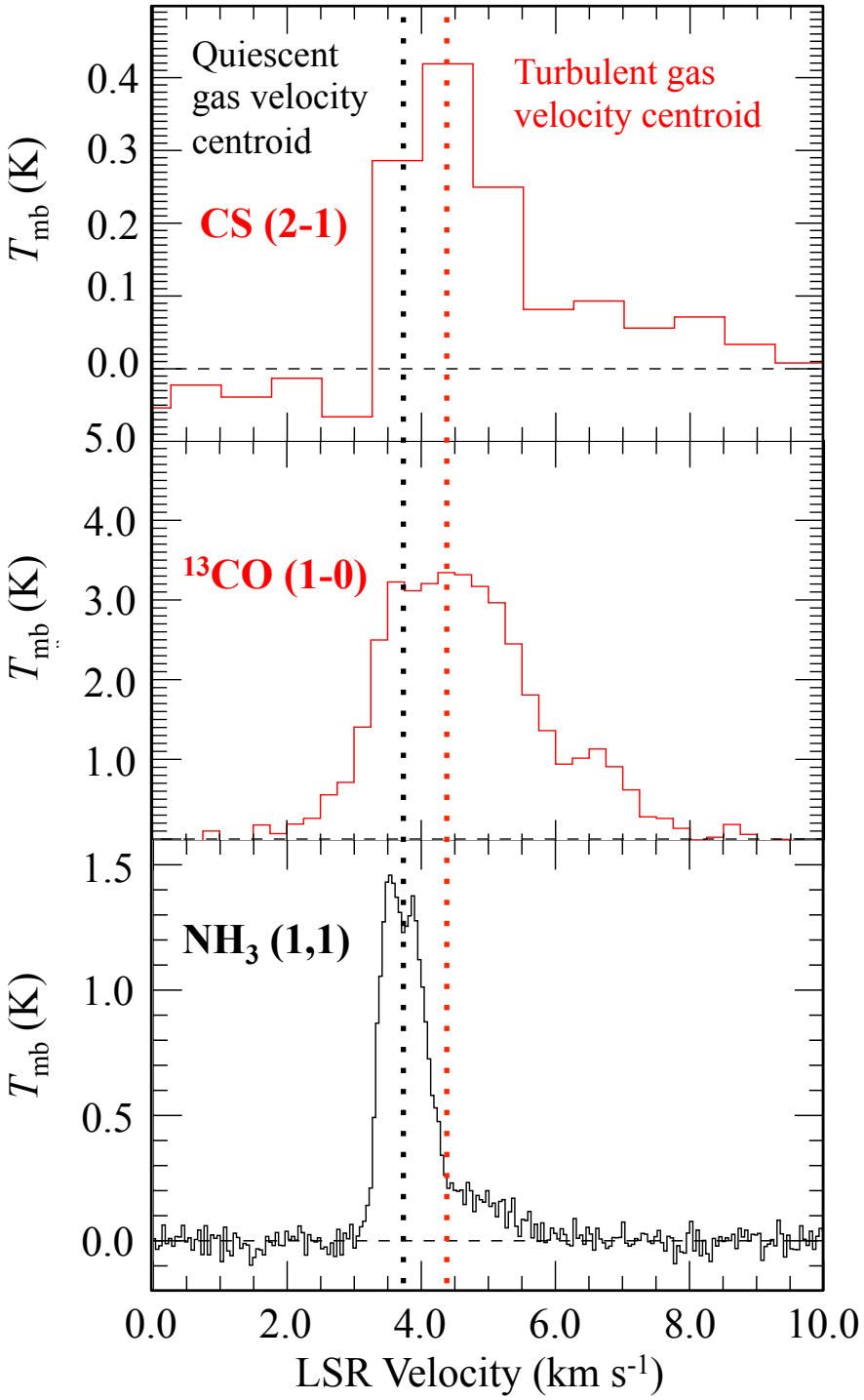

Figure 4.3: CS ($J = 2 - 1$), ^{13}CO($J = 1 - 0$), and NH_3 $(J, K = 1, 1)$ line profiles. The black dotted line indicates the centroid velocity of the quiescent NH_3 gas at 3.7 km s^{-1} and the red dotted line indicates the turbulent NH_3 gas at 4.4 km s^{-1}.

Table 4.2: LVG models for CS toward TUKH122

model	n (cm^{-3})	T_k (K)	N(CS) (cm^{-2})
fitting range	$10^3 - 10^5$	$5 - 30$	7.8×10^{14}
results	8.7×10^3	8	7.8×10^{14}

$T_\mathrm{kin} = 5 - 30$ K. We use a column density of N(CS) $\sim 7.8 \times 10^{14}$ cm^{-2}, obtained from CS $(J = 2 - 1)$ by assuming LTE condition, and a linewidth of 0.56 km s^{-1}. The formulation can be found, for example, in Lee et al. (2013). We assume the abundance ratio of $^{32}\mathrm{S}/^{34}\mathrm{S}$ to be 15 (Blake et al., 1987). We use a CS ($J = 1-0$) intensity of 4.3, a C^{34}S ($J = 2-1$)/CS($J = 1-0$) intensity ratio of 0.17, and a CS ($J = 2 - 1$) intensity of 0.7 toward the peak position of TUKH122. Figure 4.4 shows the results and the derived values are listed in Table 2. Temperature is significantly low ($\sim$ 10 K) even taking into account the uncertainties of the intensities. The observed CS $(J = 2 - 1)$ intensity is generally weaker than the value determined by the model. This has been already pointed out by Tatematsu et al. (1998). They suggested that foreground absorption due to less dense gas is significant for $J = 2 - 1$. Nishimura et al. (2015) also performed LVG analysis using CO $(J = 2 - 1)$, ^{13}CO $(J = 1 - 0)$, and ^{13}CO $(J = 2 - 1)$ lines and derived a kinematic temperature of $\sim$ 13 K toward TUKH122. Therefore, we conclude that the turbulent gas is also cold ($\sim$ 10 K).

It is worth noting that our previous results of NH_3 observations with the VLA (Tatematsu et al., 2014b) have shown no wing emission toward the core. The VLA observations were carried out using NH_3 $(J, K) = (1, 1)$ emission with 0.2 km s^{-1} velocity resolution (Figure 7 in Tatematsu et al. 2014b). From the observed intensity of the wing emission in the present study ($T_\mathrm{mb} = 0.22$ K), the flux density is estimated to be 1.31 mJy beam^{-1} at the VLA configuration of 4".2 $\times$ 3".1 resolution. The wing component were not detected with the VLA because the rms noise level of the VLA observations was as high as $\sim$ 2.6 mJy beam^{-1}. Therefore, the non-detection of the wing component with the VLA will be due to lower sensitivity. Another possibility is that the turbulent gas is widely extended and resolved out in the interferometric observations.

4.3.3 Linewidth-size relations

The linewidth-size relation has been investigated in many studies (e.g., Larson, 1981; Caselli & Myers, 1995; Goodman et al., 1998). It is suggested that the coefficient or intercept (in the log-

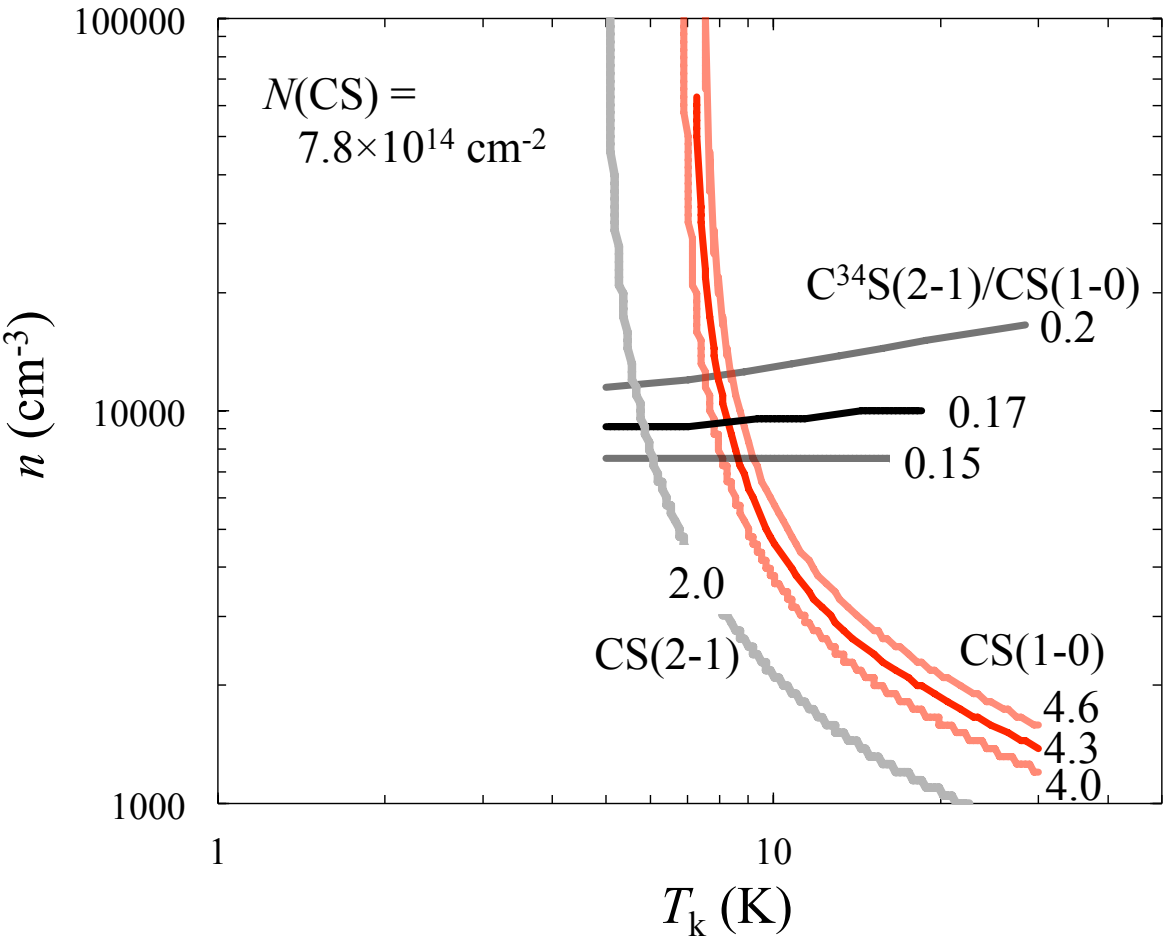

Figure 4.4: LVG results for N(CS)=7.8×10^{14} cm^{-2} and Δv =0.56 km s^{-1} are shown in the density-temperature diagram. Black, red, and grey lines show the C^{34}S ($J = 2-1$)/CS($J = 1-0$) intensity ratio, CS ($J = 1 - 0$) intensity, and CS($J = 2 - 1$) intensity, respectively.

log form) of the linewidth-size relation in GMC turbulent cores is larger than in low-mass star-forming regions, which means GMC cores have a higher level of turbulence (Tatematsu et al., 1993; Caselli & Myers, 1995; Heyer et al., 2009). Lu et al. (2014) investigated the linewidth-size relation in high-mass star-forming regions in NH_3 emission using the VLA. Their results suggest that high-mass star-forming cores still have high level of turbulence within 0.1 pc.

We estimate the nonthermal linewidth $\Delta v_{\rm NT}$, which is defined as $\Delta v_{\rm NT}^2 = \Delta v_{\rm obs}^2 - \Delta v_{\rm T}^2$, where $\Delta v_{\rm T} = (8 \ln 2\, kT_{\rm k}/m_{\rm obs})^{1/2}$ and $m_{\rm obs}$ is the mass of the observed molecules (Fuller & Myers, 1992). We assume $T_k = 11$ K, which was obtained from the NH_3 inversion transition observations, for all molecular lines. The thermal linewidth for NH_3 and mean molecular weight (2.33 u) are 0.17 km s^{-1} and 0.47 km s^{-1}, respectively.

Figure 4.5 shows the nonthermal linewidth against the core radius in TUKH122 observed in several molecular lines; ^{13}CO ($J = 1 - 0$), CS ($J = 2 - 1$), NH_3 $(J, K) = (1, 1)$, and N_2H^+ ($J = 1 - 0$). The (equivalent) core radius is calculated from the area inside the 25%, 50%, and 75% levels with respect to the maximum intensities of these molecular lines. That is the core radius can be represented

$$r(25, 50, 75\%) = \sqrt{S(25, 50, 75\%)/\pi} \tag{4.7}$$

We derived the observed linewidth, $\Delta v_{\rm obs}$, from the average spectrum from positions within the contours. We omit the plot of r(75%) for CS and N_2H^+ because S(75%) for CS and N_2H^+ is similar to the telescope beam area and the contour is not fully resolved. Our NH_3 single dish observations cannot constrain the radius. Therefore, we use the horizontal bar to illustrate the probable radius range of the NH_3 quiescent core. The NH_3 quiescent core was observed with VLA, but it was found that diffuse emission was resolved out. It is possible that the NH_3 quiescent core is as large as the N_2H^+ quiescent, if N_2H^+ and NH_3 coexist. We also use the horizontal bar for the NH_3 turbulent core radius. The NH_3 turbulent gas distribution can be as small as the NH_3 quiescent core observed with VLA, while it can be widespread as observed in CS and ^{13}CO with the Nobeyama 45 m telescope. The dashed line represents a power law index of 0.21 derived by Caselli & Myers (1995) in Orion cores. We find that the nonthermal component in TUKH122 follows the trend in the Orion cores if the core radius is larger than $\sim$ 0.2 pc. We also find that turbulence is dissipated within $\sim$ 0.2 pc, and the nonthermal linewidth becomes smaller than

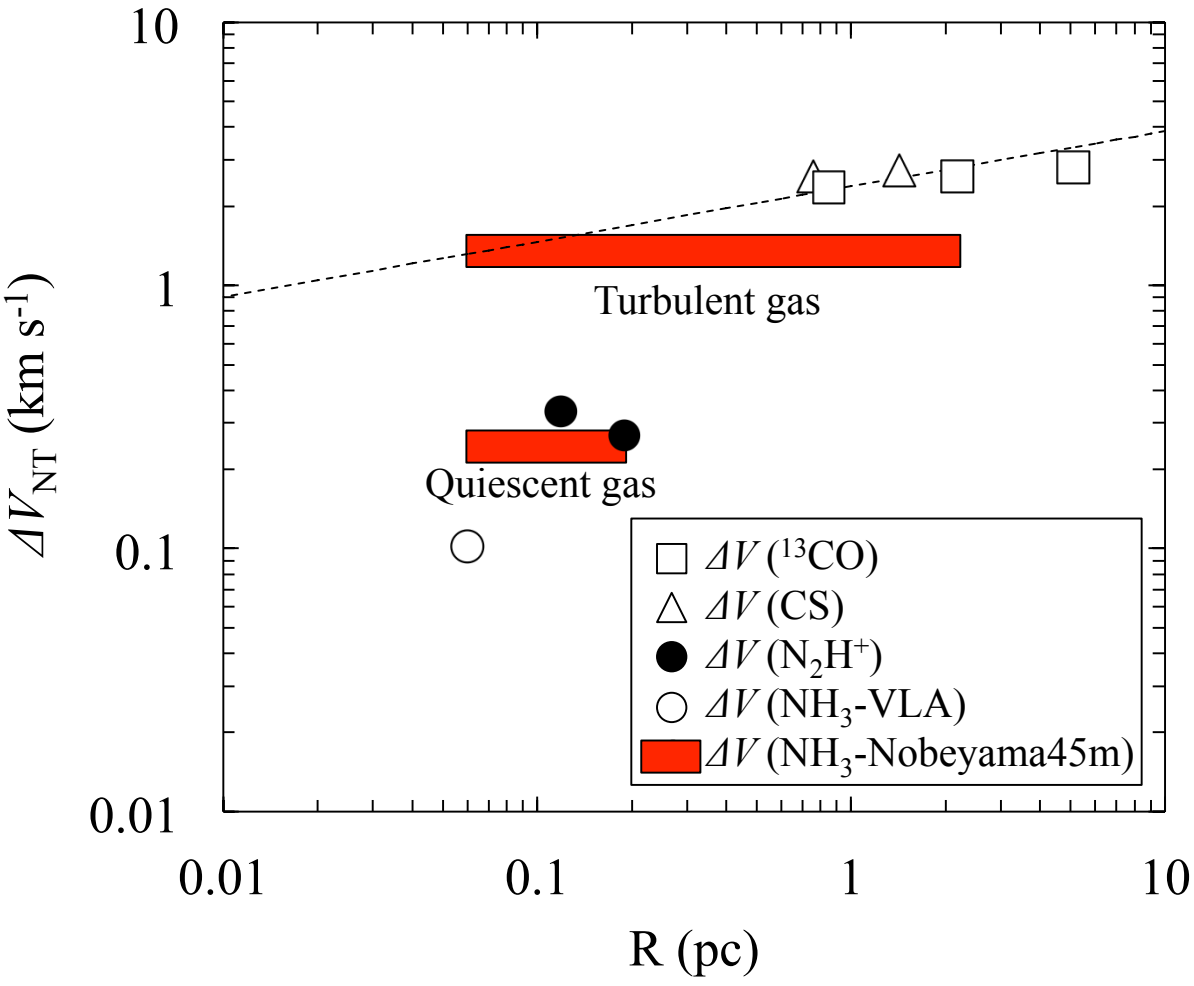

Figure 4.5: The nonthermal linewidth traced by different molecules against the core radius of the TUKH122 core. Values were derived by using the ^{13}CO ($J = 1 - 0$), CS ($J = 2 - 1$), N_2H^+ ($J = 1 - 0$), and NH_3 ($J, K = 1, 1$) observations. The dashed line represents a power law index of 0.21 derived by Caselli & Myers (1995).

the thermal linewidth (0.47 km s^{-1}) for the mean molecular weight. Our new results with high velocity resolution confirm that the nonthermal motion is almost completely dissipated. This may be the first evidence of a coherent region in a GMC core.

The nonthermal linewidth $\Delta v_{\rm NT}$ of the NH_3 wing component is derived to be 1.36 km s^{-1}, which is consistent with the trend of the linewidth-size relation derived for CS and ^{13}CO turbulent gas. Furthermore, the centroid velocity of the NH_3 wing component of 4.7 km s^{-1} corresponds to that of CS and ^{13}CO lines. Therefore, the NH_3 wing component should also trace the turbulent surrounding gas. We have observed dense turbulent gas and quiescent dense gas in a single tracer. Our detection of both NH_3 quiescent and wing components may indicate a sharp transition from the turbulent parent cloud to the quiescent high dense core.

Similar objects that have a sharp transition between turbulent surrounding gas and a coherent core have been reported by Pineda et al. (2010, 2011). However, it is still not clear how these coherent cores are formed in such turbulent environments. Some models suggest that shocks may dissipate the turbulence (Pon et al., 2012). Recently, hydrodynamic turbulent cloud simulations show the filament formation made up of a network smaller and coherent sub-filaments (Smith et al., 2016). They found that sub-filaments are formed at the stagnation points of the turbulent velocity fields where shocks dissipate the turbulence. Our results of the velocity offsets between the quiescent dense core and its parent cloud may be consistent with such simulations and TUKH122 core might be formed at the stagnation point.

Chapter 5

Discussion and summary

5.1 Discussion

In Chapter 2 and 3, we suggested that the chemical evolution will be a good indicator to determine the evolutional stages of starless cores in GMCs. We found that the column density ratios of $N(N_2H^+)/N(HC_3N)$, $N(N_2H^+)/N(CCS)$, $N(N_2H^+)/N(c\text{-}C_3H_2)$, $N(NH_3H)/N(HC_3N)$, and $N(NH_3)/N(CCS)$ are high in star forming region, while it is low in starless region. Interestingly, the ratios of $N(N_2H^+)/N(HC_3N) \sim 1-2$, $N(N_2H^+)/N(CCS) \sim 2$, $N(NH_3)/N(HC_3N) \sim 40-50$, and $N(NH_3)/N(CCS) \sim 30-40$ may divide the star-forming and starless criteria.

We investigate whether these tendencies can be found in other star-forming region and compare these threshold ratios. Sakai et al. (2008b) observed N_2H^+ and HC_3N toward the 55 massive clumps associated with IRDCs by using the Nobeyama 45 m telescope. Hirota et al. (2011) investigated NH_3/CCS ratio toward dark cloud cores and searched carbon-chain-producing regions recognized as chemically young dark cloud cores. By reanalyzing N_2H^+ and HC_3N data obtained by Sakai et al. (2008b), we plotted the column density ratio of $N(N_2H^+)/N(HC_3N)$ against rotation temperature derived by NH_3 lines (Figure 5.1). In Figure 5.1, the open circles represent star-forming cores associated with 8 and 24 μm point sources, the grey open circles represent star forming cores associated with 24 μm point sources, and filled circles represent starless cores without 8 and 24 μm sources. Figure 5.1 shows that the star forming cores associated with 8 and 24 μm point sources are high ratio, while starless cores without 8 and 24 μm sources are low ratio. Furthermore, the column density ratio increases with increasing rotation temperature. Assuming that star formation evolves from starless cores without infrared sources to star forming cores with

8 μm emission, and then into star forming cores with both 8 and 24 μm emission, we suggest that the column density ratio of $N(N_2H^+)/N(HC_3N)$ may indicate chemical evolution even in IRDCs. Furthermore, the threshold ratio of $N(N_2H^+)/N(HC_3N) \sim 1-2$ may divide the star-forming and starless cores, which is the same value with the Vela C.

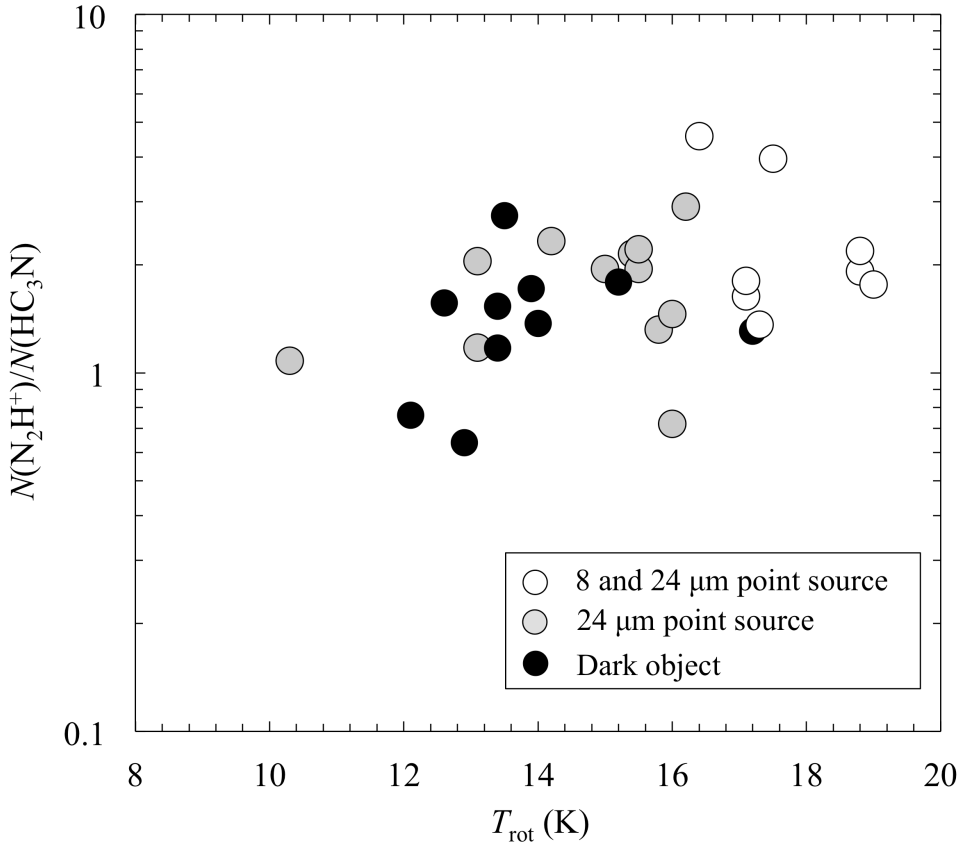

Figure 5.1: The column density ratio of N_2H^+ to HC_3N is plotted against the rotation temperature. The open circles represent star-forming cores associated with 8 and 24 μm point sources, the grey open circles represent star forming cores associated with 24 μm point sources, and filled circles represent starless cores without 8 and 24 μm sources.

Hirota et al. (2011) also investigated the NH_3/CCS ratio against star forming activities in dark cloud cores (see also figure 4 in their paper). Their results show that the star forming cores are recognized when the ratio of $N(NH_3)/N(CCS)$ is more than $\sim 30-40$. The threshold of $N(NH_3)/N(CCS) \sim 30-40$ is the same value with the orion A cloud in a velocity linewidth of $\Delta v(CCS) < 1.5$ km s^{-1}. Therefore, we suggest that the chemical evolution and its threshold between star forming and starless cores are universal and useful in wide range of star forming activities from dark clouds to IRDCs.

chemical simulations

To estimate timescale of the chemical evolution process in dense cores, we calculate the formation rate of N_2H^+, NH_3, HC_3N, and CCS molecules on gas phase using the UMIST 2012 network made by McElroy et al. (2013). The model is adapted for $n = 10^4$ cm^{-3}, $T = 10$ K, and $A_v = 10$ mag. By calculating the chemical network, Figure 5.2 shows the fractional abundances of N_2H^+, NH_3, HC_3N, and CCS against time. Taking into account the fact that typical fractional abundances are derived to be $\sim 10^{-10}$ for N_2H^+, $\sim 10^{-8}$ for NH_3, $\sim 10^{-8}$ for HC_3N, and $\sim 10^{-9}$ for CCS respectively, in dense cores (e.g., Tafalla et al., 2002; Gwenlan et al., 2000; Shinnaga et al., 2004), this chemical simulation is acceptable expect for CCS. The fact that CCS abundance fall significantly below its observed value was already reported and McElroy et al. (2013) suggested the effect of the large rate coefficient for its destruction by atomic oxygen. The rate coefficient of CCS and Oxygen reaction may decrease in cold region. Therefore, we ignore the CCS abundance in this discussion.

To estimate timescale of the dense cores, we plotted the abundance ratios of N_2H^+/HC_3N, NH_3/HC_3N, and NH_3/CCS against time in Figure 5.3. Based on published data and our studies, we showed that the abundance ratios of $N(N_2H^+)/N(HC_3N) \sim 1-2$, $N(N_2H^+)/N(CCS) \sim 2$, $N(NH_3)/N(HC_3N) \sim 40-50$, and $N(NH_3)/N(CCS) \sim 30-40$ may divide the star-forming and starless. To have such abundance ratios, it takes $4 \times 10^5 - 10^6$ year according to the Figure 5.3. This timescale is longer than or equal to the timescale derived by Onishi et al. (2002) for starless cores. Note that we ignore the $N(NH_3)/N(CCS)$ ratio due to CCS highly underabundant.

The timescale is several times larger than free-fall timescale of gas with 10^5 cm^3, $\sim 10^5$ yr. Therefore, some other mechanisms are needed to support self-gravitating cores against gravity. Nakano (1998) suggested that dense cores embedded in clouds are shown to be magnetically supercritical and that the turbulence dissipates in several times the free-fall time, leading to a dynamical collapse of the cores. The timescale of dissipation of turbulence is almost consistent with dynamical time,

$$t_{\rm dyn} = 5.0 \times 10^5 \times \frac{R}{0.1\ \ {\rm pc}} \times \frac{0.2\ \ {\rm km\ s^{-1}}}{C_s}\ \ {\rm yr}. \tag{5.1}$$

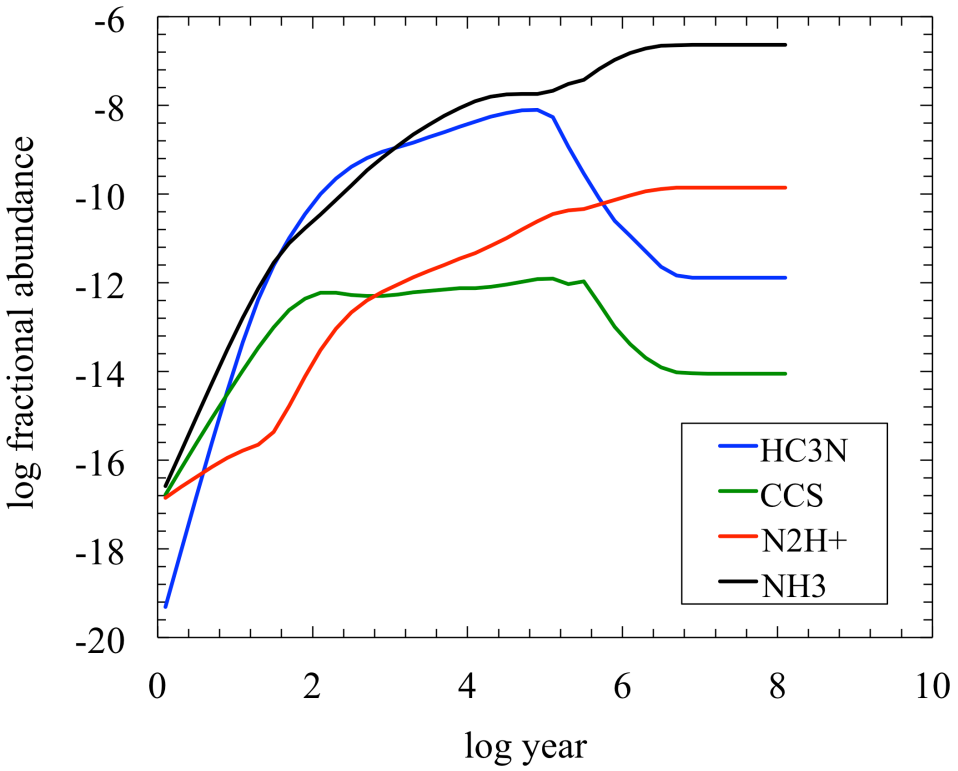

Figure 5.2: The fractional abundances of N_2H^+, NH_3, HC_3N, and CCS against the time assuming a dense core model for $n = 10^4$ cm^{-3}, $T = 10$ K, and $A_v = 10$ mag.

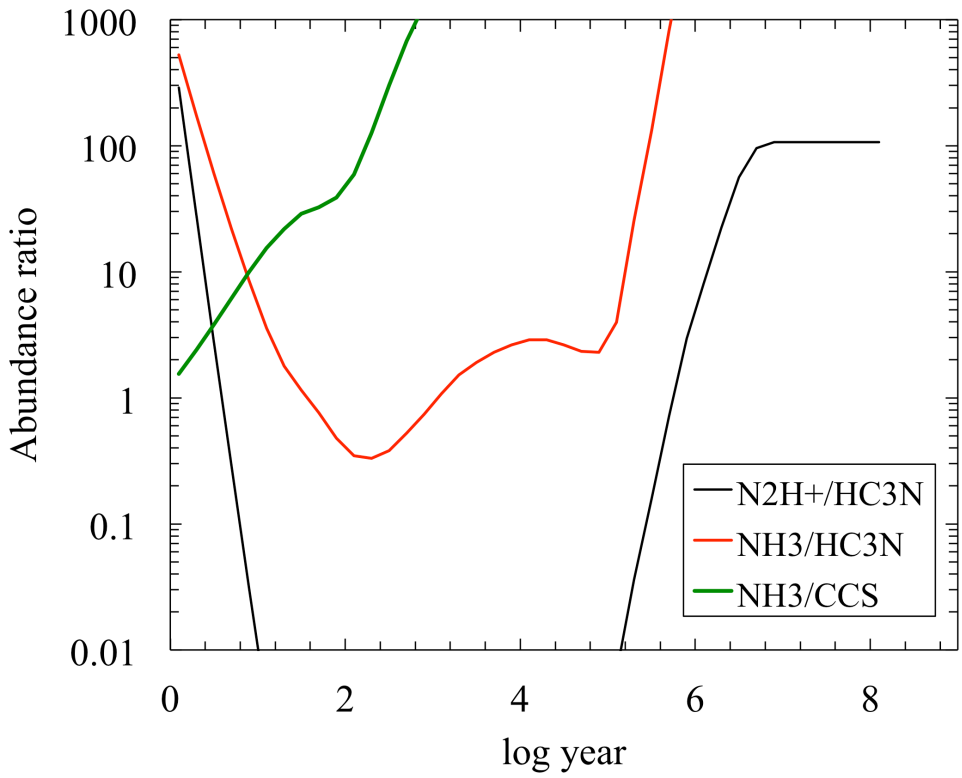

Figure 5.3: The fractional abundance ratios of N_2H^+/HC_3N, NH_3/HC_3N, and NH_3/CCS against time.

Therefore, the dissipation of the turbulence is an important factor to initiate star formation. Furthermore, we already found the correlation between the chemical evolution ($N(\mathrm{NH_3})/N(\mathrm{CCS})$) and dissipation of turbulence (R/R_{cr}), suggesting that the chemical evolution can be an indicator of the dynamical evolution of the core and the timescale is determined by the dissipation of turbulence.

5.2 Summary

Chemical composition was measured in selected six warm and dense cores in the Orion A giant molecular cloud for N_2H^+, CCS, c-C_3H_2, HCO^+, $H^{13}CO^+$, and HCN. Both N_2H^+ and c-C_3H_2 show similar trend, they are suppressed against CCS in starless cores are enhanced in star-forming cores. Correlation is tighter for c-C_3H_2 than N_2H^+, possibly due to destruction of N_2H^+ by CO in warm region. NH_3 was also found to be suppressed against CCS and HC3N in starless cores and to be enhanced in star-forming cores, confirming the trend found in cold dark clouds but with lower ratios for larger values of temperature and linewidth.

To test the reliability of the abundance ratios as chemical clocks of core evolution in more broader range of physical conditions, a total of 7 regions selected from bright $C^{18}O$ peaks in the Vela C molecular cloud complex were observed in N_2H^+ and HC_3N emission. The N_2H^+/HC_3N abundance ratio was smaller in starless cores and higher in star-forming cores. This trend is similar to the one established in the Orion A GMC, though the distinction between the ratios for starless and star-forming cores is not as clear as that in N_2H^+/CCS ratio in the Orion A GMC.

It is suggested that the chemical compositions are robust and useful clocks for the evolutionary stage of dense cores even in warm GMCs. Species like CCS, NH_3, and c-C_3H_2 are more reliable than HC_3N and N_2H^+ as chemical clocks of dense core evolution in GMCs warmer than 25 K.

By using the published data of $N(\mathrm{NH_3})/N(\mathrm{CCS})$ and $N(\mathrm{N_2H^+})/N(\mathrm{HC_3N})$ in dark clouds and infrared dark cloud clumps, we found the criteria between star forming and starless cores are $N(\mathrm{NH_3})/N(\mathrm{CCS}) \sim 30 - 40$ and $N(\mathrm{N_2H^+})/N(\mathrm{HC_3N}) \sim 1 - 2$. Using the chemical reaction network of UMIST Database for Astrochemistry (UDfA) assuming a density of 10^4 cm^{-3} and a temperature of 10 K, we estimated a timescale of $4 \times 10^5 - 1 \times 10^6$ yr for taking these criteria of the column density ratios. This lifetime is several times longer than free-fall timescale and comparable to dissipation timescale of turbulence. The NH_3/CCS abundance ratio appears to be

correlated with the core radius normalized with the critical radius ($R/R_{\rm cr}$). Starless cores tend to have higher ratio of $R/R_{\rm cr}$ exceeding unity, indicating hydrostatic equilibrium of these cores. For star-forming cores, this ratio tends to be lower. Dissipation of turbulence may play an important role because $R/R_{\rm cr}$ decreases with decreasing linewidth.

One of the chemically-selected starless cores at advanced evolutionary stages (TUKH122) in Orion A GMC was observed in NH_3 lines. Two velocity components were identified: a quiet main component with a small linewidth ($\sim$ 0.3 km s^{-1}) and a redshifted wing component with a large linewidth ($\sim$ 1.4 km s^{-1}). There is clear velocity offset between these two components, and the centroid velocity of the turbulent component agrees with that of the surrounding gas traced by ^{13}CO $J = 1 - 0$ and CS $J = 2 - 1$ emission lines. Given that turbulence dissipates in a $\sim$ 0.2 pc region, this core may have a coherent region. This is the first detection of such an object in the GMC. The detection of NH_3 emission for both quiescent and wing components indicates a sharp transition from the turbulent parent cloud to the quiescent dense core.

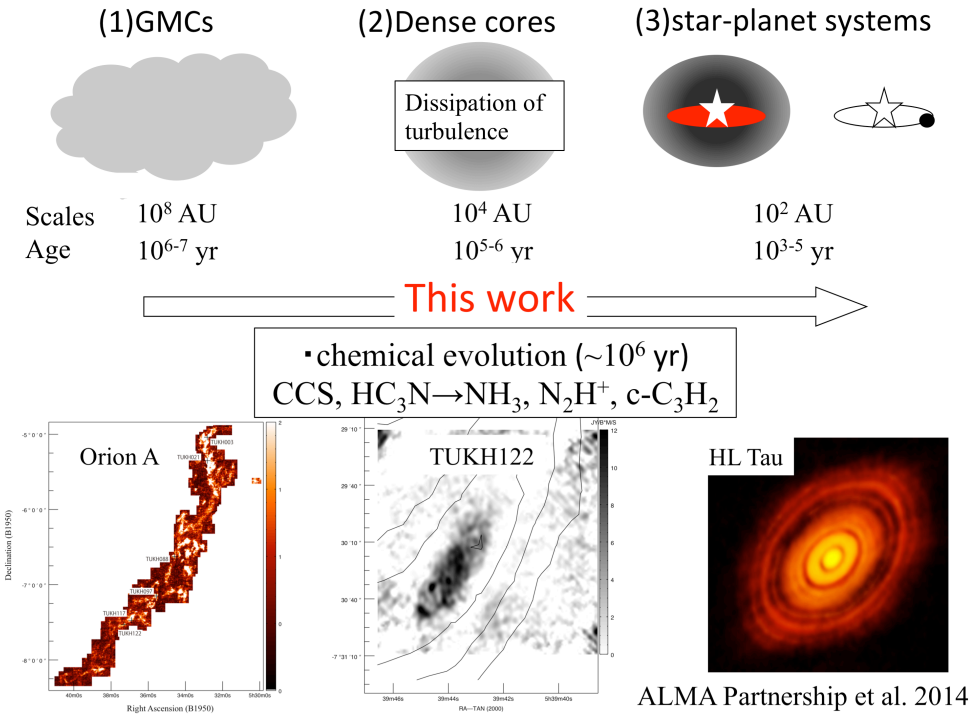

Figure 5.4: The schematic view of this thesis.

Appendix A

Hyperfine fitting of N_2H^+ and NH_3

N_2H^+ ($J = 1 - 0$) and NH_3 ($J, K = 1, 1$) lines have hyperfine structures. We identify a total of 7 lines in N_2H^+ and 10 lines in NH_3 if linewidth is small (e.g., Caselli & Myers, 1995; Tiné et al., 2000).

Therefore, line intensity can be expressed by following

$$T_{\rm mb}(v) = [J_\nu(T_{\rm ex}) - J_\nu(T_{\rm bg})][1 - \exp(-\tau(v))] \tag{A.1}$$

$$\tau(v) = \tau_{\rm tot} \sum_i s_i \exp\left\{-4\log 2 \left(\frac{v - v_i - v_{\rm LSR}}{\Delta v}\right)^2\right\} \tag{A.2}$$

$T_{\rm bg}$ is the back ground temperature of 2.7 K, ν is observing frequency, s_i is the line intensity, and v_i is the velocity referred to the $F_1 = 2 - 1, F = 3 - 2$ for N_2H^+ amd $\Delta F = 0$ for NH_3 line, respectively (see also A.1 and A.2).

Table A.1: The line intensity and velocity offset of each component in N_2H^+ (Tiné et al., 2000)

(J)	transition	v_i (km s^{-1})	s_i
J=1-0	$F_1 = 1 - 1, F = 0 - 1$	6.9	0.037
	$F_1 = 1 - 1, F = 2 - 2$	5.97	0.185
	$F_1 = 1 - 1, F = 1 - 1$	5.53	0.111
	$F_1 = 2 - 1, F = 2 - 1$	0.93	0.185
	$F_1 = 2 - 1, F = 3 - 2$	0	0.259
	$F_1 = 2 - 1, F = 1 - 0$	-0.66	0.111
	$F_1 = 0 - 0, F = 1 - 2$	-8.03	0.111

Therefore, free parameters of our hyperfine fitting is $\tau_{\rm tot}$, $v_{\rm LSR}$, Δv, and $T_{\rm ex}$. We fit equations of A.1 and A.2 with a least-squares Gaussian hyperfine structure fitting routine written in IDL

Table A.2: The line intensity and velocity offset of each component in NH_3 (Armstrong & Barrett, 1985)

(J, K)	transition	v_i (km s^{-1})	s_i
(1,1)	$\Delta F = 0$	0	0.500
	F', F = 1,2	$\pm$7.8	0.139
	F', F = 1,0	$\pm$19.4	0.111

(LMFIT). The fit is optimized by the use of the Levenberg-Marquardt algorithm (for non-linear fitting). Iterations are performed until the solutions are converged.

Acknowledgments

The author would like to thank all persons who have been assisting, and encouraging me, to complete this thesis.

Firs of all, the author would like to give my special thanks to Prof. Ken'ichi Tatematsu for his much of continuous encouragement and invaluable comments, not only for scientific studies but also my astronomer life. He has spent a great amount of time working with me and has helped me to improve the contents of this thesis. The author also gives my special thanks to Prof. Seiichi Sakamoto and Prof. Norikazu Mizuno, who are my supervisors. They gave me many good opportunities to study radio astronomy. The author tanks to Dr. Patricio Sanhueza for helpful comments and suggestions on this work. He also gave ma a chance to collaborate with Dr. Qizhou Zhang and his group at Harvard Smithonian Center for Astrophysics.

The author is deeply indebted to the Chile observatory members of NAOJ. The author has been encouraged through discussions by many astronomers, particularly, Prof. Satoru Iguchi, Prof. Daisuke Iono, Prof. Takeshi Okuda, Prof. Hiroshi Nagai, Dr. Kazuya Saigo, Dr. Hatsukade Bunyo, Dr. Yuichi Matsuda and Dr. Eiji Akiyama. The author also thanks to the NRO 45 m team for supporting me the common use observations.

The author deeply thanks to Dr. Toshiki Saito, Dr. Kyoko Onishi, Dr. Yusuke Aso, Dr. Kazuhiro Kiyokane, Dr. Ayumu Matsuzawa, Dr. Kosuke Fujii, Mr. Yuzo Otomo, Mr. Shin Koyamatsu and Ms. Chihomi Hara for discussion and continuous encouragement as friends. The author also thanks to Mr. Yuta Kato, Ms. Minju Lee, Mr. Tomonari Michiyama, Mr. Sho Kuwahara, Mr. Takuya Kurahashi, Mr. Ippei Kurose, and Ms. Misaki Ando for enjoying astronomer life.

The author is supported by the Grant-in -Aid for Japan Society for the Promotion of Science (JSPS) for young scientist.

Finally, the author would like to thank my family for their support.

Reference

Adams, F. C., Lada, C. J., & Shu, F. H. 1987, ApJ, 312, 788

Aikawa, Y., Ohashi, N., Inutsuka, S.-i., Herbst, E., & Takakuwa, S. 2001, ApJ, 552, 639

Alves, J. F., Lada, C. J., & Lada, E. A. 2001, Natur, 409, 159

Andre, P., & Montmerle, T. 1994, ApJ, 420, 837

Andre, P., Ward-Thompson, D., & Barsony, M. 1993, ApJ, 406, 122

Armstrong, J. T., & Barrett, A. H. 1985, ApJS, 57, 535

Asayama, S., & Nakajima, T. 2013, PASP, 125, 213

Aso, Y., Tatematsu, K., Sekimoto, Y., Nakano, T., Umemoto, T., Koyama, K., & Yamamoto, S. 2000, ApJS, 131, 465

Aso, Y., et al. 2015, ApJ, 812, 27

Baba, D., et al. 2006, AJ, 132, 1692

Bachiller, R., Guilloteau, S., & Kahane, C. 1987, A&A, 173, 324

Bate, M. R., & Bonnell, I. A. 2005, MNRAS, 356, 1201

Battersby, C., Bally, J., Jackson, J. M., Ginsburg, A., Shirley, Y. L., Schlingman, W., & Glenn, J. 2010, ApJ, 721, 222

Beichman, C. A., Myers, P. C., Emerson, J. P., Harris, S., Mathieu, R., Benson, P. J., & Jennings, R. E. 1986, ApJ, 307, 337

Benson, P. J., Caselli, P., & Myers, P. C. 1998, ApJ, 506, 743

Benson, P. J., & Myers, P. C. 1980, ApJL, 242, L87

—. 1989, ApJS, 71, 89

Bergin, E. A., Snell, R. L., & Goldsmith, P. F. 1996, ApJ, 460, 343

Blake, G. A., Sutton, E. C., Masson, C. R., & Phillips, T. G. 1987, ApJ, 315, 621

Bonnell, I. A., Vine, S. G., & Bate, M. R. 2004, MNRAS, 349, 735

Bonnor, W. B. 1956, MNRAS, 116, 351

Caselli, P., & Myers, P. C. 1995, ApJ, 446, 665

Caselli, P., Walmsley, C. M., Zucconi, A., Tafalla, M., Dore, L., & Myers, P. C. 2002, ApJ, 565, 331

Cesaroni, R., & Wilson, T. L. 1994, A&A, 281, 209

Chabrier, G. 2003, PASP, 115, 763

Chambers, E. T., Jackson, J. M., Rathborne, J. M., & Simon, R. 2009, ApJS, 181, 360

Chini, R., Reipurth, B., Ward-Thompson, D., Bally, J., Nyman, L.-Å., Sievers, A., & Billawala, Y. 1997, ApJL, 474, L135

Contreras, Y., Garay, G., Rathborne, J. M., & Sanhueza, P. 2016, MNRAS, 456, 2041

Danby, G., Flower, D. R., Valiron, P., Schilke, P., & Walmsley, C. M. 1988, MNRAS, 235, 229

Dickman, R. L. 1978, ApJS, 37, 407

Dirienzo, W. J., Brogan, C., Indebetouw, R., Chandler, C. J., Friesen, R. K., & Devine, K. E. 2015, AJ, 150, 159

Ebert, R. 1955, Zs. Ap., 37, 217

Egan, M. P., Shipman, R. F., Price, S. D., Carey, S. J., Clark, F. O., & Cohen, M. 1998, ApJL, 494, L199

Evans, II, N. J., Di Francesco, J., Lee, J.-E., Jørgensen, J. K., Choi, M., Myers, P. C., & Mardones, D. 2015, ApJ, 814, 22

Evans, II, N. J., Levreault, R. M., & Harvey, P. M. 1986, ApJ, 301, 894

Evans, II, N. J., et al. 2003, PASP, 115, 965

—. 2009, ApJS, 181, 321

Feng, S., Beuther, H., Zhang, Q., Liu, H. B., Zhang, Z., Wang, K., & Qiu, K. 2016, ApJ, 828, 100

Fukui, Y., et al. 2008, ApJS, 178, 56

Fuller, G. A., & Myers, P. C. 1992, ApJ, 384, 523

Furuya, R. S., Kitamura, Y., & Shinnaga, H. 2006, ApJ, 653, 1369

Galloway, E. T., & Herbst, E. 1989, A&A, 211, 413

Geballe, T. R., & Oka, T. 1996, Natur, 384, 334

Genzel, R., & Stutzki, J. 1989, ARA&A, 27, 41

Giannini, T., et al. 2012, A&A, 539, A156

Goldreich, P., & Kwan, J. 1974, ApJ, 189, 441

Goodman, A. A., Barranco, J. A., Wilner, D. J., & Heyer, M. H. 1998, ApJ, 504, 223

Gwenlan, C., Ruffle, D. P., Viti, S., Hartquist, T. W., & Williams, D. A. 2000, A&A, 354, 1127

Henshaw, J. D., et al. 2016, MNRAS, 463, 146

Herbst, E., Defrees, D. J., & McLean, A. D. 1987, ApJ, 321, 898

Heyer, M., Krawczyk, C., Duval, J., & Jackson, J. M. 2009, ApJ, 699, 1092

Hildebrand, R. H. 1983, QJRAS, 24, 267

Hill, T., et al. 2011, A&A, 533, A94

Hirahara, Y., et al. 1992, ApJ, 394, 539

Hirota, T., Ito, T., & Yamamoto, S. 2002, ApJ, 565, 359

Hirota, T., Ohishi, M., & Yamamoto, S. 2009, ApJ, 699, 585

Hirota, T., Sakai, N., & Yamamoto, S. 2010, ApJ, 720, 1370

Hirota, T., Sakai, T., Sakai, N., & Yamamoto, S. 2011, ApJ, 736, 4

Ho, P. T. P., & Townes, C. H. 1983, ARA&A, 21, 239

Hoare, M. G., Kurtz, S. E., Lizano, S., Keto, E., & Hofner, P. 2007, Protostars and Planets V, 181

Hogerheijde, M. R., & Sandell, G. 2000, ApJ, 534, 880

Hunter, C. 1977, ApJ, 218, 834

Ikeda, N., Sunada, K., & Kitamura, Y. 2007, ApJ, 665, 1194

Izumi, T., et al. 2013, PASJ, 65, 100

Kandori, R., et al. 2005, AJ, 130, 2166

Kauffmann, J., Pillai, T., & Goldsmith, P. F. 2013, ApJ, 779, 185

Kawamura, A., et al. 2009, ApJS, 184, 1

Kim, K.-T., et al. 2011, Journal of Korean Astronomical Society, 44, 81

Kim, M. K., et al. 2008, PASJ, 60, 991

Kohno, K., Matsushita, S., Vila-Vilaró, B., Okumura, S. K., Shibatsuka, T., Okiura, M., Ishizuki, S., & Kawabe, R. 2001, in Astronomical Society of the Pacific Conference Series, Vol. 249, The Central Kiloparsec of Starbursts and AGN: The La Palma Connection, ed. J. H. Knapen, J. E. Beckman, I. Shlosman, & T. J. Mahoney, 672

Kroupa, P. 2001, MNRAS, 322, 231

Kukolich, S. G. 1967, Physical Review, 156, 83

Kurono, Y., Saito, M., Kamazaki, T., Morita, K.-I., & Kawabe, R. 2013, ApJ, 765, 85

Lada, C. J., & Lada, E. A. 2003, ARA&A, 41, 57

Lada, C. J., & Wilking, B. A. 1984, ApJ, 287, 610

Ladd, N., Purcell, C., Wong, T., & Robertson, S. 2005, PASA, 22, 62

Lai, S.-P., & Crutcher, R. M. 2000, ApJS, 128, 271

Larson, R. B. 1969, MNRAS, 145, 271

—. 1981, MNRAS, 194, 809

Launhardt, R., et al. 2013, A&A, 551, A98

Lee, J.-E., Bergin, E. A., & Evans, II, N. J. 2004, ApJ, 617, 360

Lee, K., Looney, L. W., Schnee, S., & Li, Z.-Y. 2013, ApJ, 772, 100

Lee, S.-S., et al. 2011, PASP, 123, 1398

Levreault, R. M. 1988, ApJS, 67, 283

Levshakov, S. A., Molaro, P., Lapinov, A. V., Reimers, D., Henkel, C., & Sakai, T. 2010, A&A, 512, A44

Li, D., Kauffmann, J., Zhang, Q., & Chen, W. 2013, ApJL, 768, L5

Lique, F., Spielfiedel, A., & Cernicharo, J. 2006, A&A, 451, 1125

Liseau, R., Lorenzetti, D., Nisini, B., Spinoglio, L., & Moneti, A. 1992, A&A, 265, 577

Loughnane, R. M., Redman, M. P., Thompson, M. A., Lo, N., O'Dwyer, B., & Cunningham, M. R. 2012, MNRAS, 420, 1367

Lu, X., Zhang, Q., Liu, H. B., Wang, J., & Gu, Q. 2014, ApJ, 790, 84

Machida, M. N., & Hosokawa, T. 2013, MNRAS, 431, 1719

MacLaren, I., Richardson, K. M., & Wolfendale, A. W. 1988, ApJ, 333, 821

Maezawa, H., et al. 1999, ApJL, 524, L129

Mangum, J. G., & Shirley, Y. L. 2015, PASP, 127, 266

Mangum, J. G., Wootten, A., & Mundy, L. G. 1992, ApJ, 388, 467

Massi, F., Lorenzetti, D., & Giannini, T. 2003, A&A, 399, 147

McElroy, D., Walsh, C., Markwick, A. J., Cordiner, M. A., Smith, K., & Millar, T. J. 2013, A&A, 550, A36

McKee, C. F., & Tan, J. C. 2003, ApJ, 585, 850

Megeath, S. T., et al. 2012, AJ, 144, 192

Milam, S. N., Savage, C., Brewster, M. A., Ziurys, L. M., & Wyckoff, S. 2005, ApJ, 634, 1126

Morales Ortiz, J. L., et al. 2012, A&A, 543, A65

Motte, F., Bontemps, S., Schilke, P., Schneider, N., Menten, K. M., & Broguière, D. 2007, A&A, 476, 1243

Murphy, D. C., & May, J. 1991, A&A, 247, 202

Myers, P. C., & Benson, P. J. 1983a, RMxAA, 7, 238

—. 1983b, ApJ, 266, 309

Myers, P. C., Linke, R. A., & Benson, P. J. 1983, ApJ, 264, 517

Nagahama, T., Mizuno, A., Ogawa, H., & Fukui, Y. 1998, AJ, 116, 336

Nakajima, T., et al. 2013, PASP, 125, 252

Nakano, T. 1998, ApJ, 494, 587

Nishimura, A., et al. 2015, ApJS, 216, 18

Ohashi, N., et al. 2014a, ApJ, 796, 131

Ohashi, S., Sanhueza, P., Chen, H.-R. V., Zhang, Q., Busquet, G., Nakamura, F., Palau, A., & Tatematsu, K. 2016a, ArXiv e-prints

Ohashi, S., Tatematsu, K., Fujii, K., Sanhueza, P., Nguyen Luong, Q., Choi, M., Hirota, T., & Mizuno, N. 2016b, PASJ, 68, 3

Ohashi, S., Tatematsu, K., Sanhueza, P., Hirota, T., Choi, M., & Mizuno, N. 2016c, MNRAS, 459, 4130

Ohashi, S., et al. 2014b, PASJ, 66, 119

Onishi, T., Mizuno, A., Kawamura, A., Tachihara, K., & Fukui, Y. 2002, ApJ, 575, 950

Oya, Y., Sakai, N., López-Sepulcre, A., Watanabe, Y., Ceccarelli, C., Lefloch, B., Favre, C., & Yamamoto, S. 2016, ApJ, 824, 88

Penston, M. V. 1969, MNRAS, 144, 425

Perault, M., et al. 1996, A&A, 315, L165

Peretto, N., & Fuller, G. A. 2009, A&A, 505, 405

Pillai, T., Kauffmann, J., Wyrowski, F., Hatchell, J., Gibb, A. G., & Thompson, M. A. 2011, A&A, 530, A118

Pillai, T., Wyrowski, F., Carey, S. J., & Menten, K. M. 2006, A&A, 450, 569

Pineda, J. E., Goodman, A. A., Arce, H. G., Caselli, P., Foster, J. B., Myers, P. C., & Rosolowsky, E. W. 2010, ApJL, 712, L116

Pineda, J. E., Goodman, A. A., Arce, H. G., Caselli, P., Longmore, S., & Corder, S. 2011, ApJL, 739, L2

Pon, A., Johnstone, D., & Kaufman, M. J. 2012, ApJ, 748, 25

Ragan, S. E., Bergin, E. A., & Wilner, D. 2011, ApJ, 736, 163

Ragan, S. E., Heitsch, F., Bergin, E. A., & Wilner, D. 2012, ApJ, 746, 174

Rathborne, J. M., Jackson, J. M., & Simon, R. 2006, ApJ, 641, 389

Rathborne, J. M., Jackson, J. M., Zhang, Q., & Simon, R. 2008, ApJ, 689, 1141

Reiter, M., Shirley, Y. L., Wu, J., Brogan, C., Wootten, A., & Tatematsu, K. 2011, ApJS, 195, 1

Rydbeck, O. E. H., Hjalmarson, A., Rydbeck, G., Ellder, J., Olofsson, H., & Sume, A. 1981, ApJL, 243, L41

Sakai, N., Sakai, T., Hirota, T., & Yamamoto, S. 2008a, ApJ, 672, 371

Sakai, N., et al. 2014, Natur, 507, 78

Sakai, T., Sakai, N., Kamegai, K., Hirota, T., Yamaguchi, N., Shiba, S., & Yamamoto, S. 2008b, ApJ, 678, 1049

Salpeter, E. E. 1955, ApJ, 121, 161

Sanhueza, P., Garay, G., Bronfman, L., Mardones, D., May, J., & Saito, M. 2010, ApJ, 715, 18

Sanhueza, P., Jackson, J. M., Foster, J. B., Garay, G., Silva, A., & Finn, S. C. 2012, ApJ, 756, 60

Scalo, J. M. 1986, FcPh, 11, 1

Scoville, N. Z., & Solomon, P. M. 1974, ApJL, 187, L67

Shinnaga, H., Ohashi, N., Lee, S.-W., & Moriarty-Schieven, G. H. 2004, ApJ, 601, 962

Shirley, Y. L. 2015, PASP, 127, 299

Shirley, Y. L., et al. 2013, ApJS, 209, 2

Shu, F. H., Adams, F. C., & Lizano, S. 1987, ARA&A, 25, 23

Simon, R., Jackson, J. M., Rathborne, J. M., & Chambers, E. T. 2006, ApJ, 639, 227

Smith, R. J., Glover, S. C. O., Klessen, R. S., & Fuller, G. A. 2016, MNRAS, 455, 3640

Snell, R. L., Loren, R. B., & Plambeck, R. L. 1980, ApJL, 239, L17

Strom, K. M., Strom, S. E., & Merrill, K. M. 1993, ApJ, 412, 233

Sunada, K., Ikeda, N., Kitamura, Y., Nakazato, T., & Yang, J. 2009, in Astronomical Society of the Pacific Conference Series, Vol. 418, AKARI, a Light to Illuminate the Misty Universe, ed. T. Onaka, G. J. White, T. Nakagawa, & I. Yamamura, 73

Suzuki, H. 1983, ApJ, 272, 579

Suzuki, H., Yamamoto, S., Ohishi, M., Kaifu, N., Ishikawa, S.-I., Hirahara, Y., & Takano, S. 1992, ApJ, 392, 551

Tafalla, M., Mardones, D., Myers, P. C., Caselli, P., Bachiller, R., & Benson, P. J. 1998, ApJ, 504, 900

Tafalla, M., Myers, P. C., Caselli, P., & Walmsley, C. M. 2004, A&A, 416, 191

Tafalla, M., Myers, P. C., Caselli, P., Walmsley, C. M., & Comito, C. 2002, ApJ, 569, 815

Takahashi, S., Ho, P. T. P., Teixeira, P. S., Zapata, L. A., & Su, Y.-N. 2013, ApJ, 763, 57

Takano, S., et al. 2014, PASJ, 66, 75

Tan, J. C., Kong, S., Butler, M. J., Caselli, P., & Fontani, F. 2013, ApJ, 779, 96

Tan, J. C., Kong, S., Zhang, Y., Fontani, F., Caselli, P., & Butler, M. J. 2016, ApJL, 821, L3

Tatematsu, K., Hirota, T., Kandori, R., & Umemoto, T. 2010, PASJ, 62, 1473

Tatematsu, K., Kandori, R., Umemoto, T., & Sekimoto, Y. 2008, PASJ, 60, 407

Tatematsu, K., Umemoto, T., Heyer, M. H., Hirano, N., Kameya, O., & Jaffe, D. T. 1998, ApJS, 118, 517

Tatematsu, K., et al. 1993, ApJ, 404, 643

—. 2014a, PASJ, 66, 16

—. 2014b, ApJ, 789, 83

Tiné, S., Roueff, E., Falgarone, E., Gerin, M., & Pineau des Forêts, G. 2000, A&A, 356, 1039

Ulich, B. L., & Haas, R. W. 1976, ApJS, 30, 247

Ungerechts, H., Bergin, E. A., Goldsmith, P. F., Irvine, W. M., Schloerb, F. P., & Snell, R. L. 1997, ApJ, 482, 245

van der Tak, F. F. S., Black, J. H., Schöier, F. L., Jansen, D. J., & van Dishoeck, E. F. 2007, A&A, 468, 627

Walmsley, C. M., Churchwell, E., Nash, A., & Fitzpatrick, E. 1982, ApJL, 258, L75

Wang, K., Zhang, Q., Wu, Y., & Zhang, H. 2011, ApJ, 735, 64

Wang, Y., Zhang, Q., Rathborne, J. M., Jackson, J., & Wu, Y. 2006, ApJL, 651, L125

Whittet, D. C. B., et al. 1996, A&A, 315, L357

Whitworth, A., & Summers, D. 1985, MNRAS, 214, 1

Wilson, T. L., Mauersberger, R., Gensheimer, P. D., Muders, D., & Bieging, J. H. 1999, ApJ, 525, 343

Wiseman, J. J., & Ho, P. T. P. 1998, ApJ, 502, 676

Yamaguchi, N., Mizuno, N., Saito, H., Matsunaga, K., Mizuno, A., Ogawa, H., & Fukui, Y. 1999, PASJ, 51, 775

Yamaguchi, T., et al. 2012, PASJ, 64, 105

Zhang, Q., Wang, K., Lu, X., & Jiménez-Serra, I. 2015, ApJ, 804, 141

Zhang, Q., Wang, Y., Pillai, T., & Rathborne, J. 2009, ApJ, 696, 268